Unravelling the interactions of nucleoid-associated proteins with DNA using single-molecule biophysical techniques

Samuel Brian Yoshua

PhD

University of York

Physics

January 2020

ABSTRACT

Nucleoid-associated proteins are a large family of proteins that are involved in both structuring and regulating the bacterial genome. Individually they only make small changes to DNA but work in tandem to organise the nucleoid into a compact and organised structure. In this thesis I look at three of these proteins: the DNA-binding proteins, H-NS and StpA, and the integration host factor (IHF). H-NS and StpA were investigated using tethered-particle motion and optical tweezers. They form filaments along DNA, and can also bridge DNA. I show that these filaments are permanently altered by biologically-relevant (piconewton) forces. Mutants of StpA, with different dimerisation behaviour, demonstrate the importance of oligomerisation in the force-dependent behaviour of these filaments beyond DNA binding. Atomic force microscopy (AFM) was used to study IHF, to determine the angles by which it bends DNA. IHF appears to have two non-specific partial bending modes as well as the canonical bending mode that requires a consensus sequence. Additionally, large clusters of DNA were seen, formed by IHF bridging DNA, providing evidence for IHF in the stabilisation of extracellular DNA in biofilms and a potential role in nucleoid organisation. Individually these proteins only make small changes to DNA and so axial optical tweezers were developed to be able to perform force spectroscopy on DNA that is hundreds of base pairs long. This will allow for sequence specific behaviour to be investigated, and the isolation of single binding sites as with AFM.

TABLE OF CONTENTS

Page

LIST OF TABLES

LIST OF FIGURES

I would like to thank the many people who made this thesis possible. I am especially grateful to Prof. Mark Leake, who gave me this opportunity, and whose support and advice was invaluable.

I would also like to thank Dr Agnes Noy and George Watson for their insights, and Dr Jamieson Howard for helping to fill in the many gaps in knowledge of molecular biology. I am indebted to the support and discussion from the other members of the Leake group, including the advice from Dr Adam Wollman and Dr Alex Hargreaves, who always made time if I had an issue to discuss - even if sometimes it was politics. My time in the lab would not have been the same without Sébastien Guilbaud, who liked to tinker with optics as much as I came to, and I am thankful for that. I would also like to thank Dr Alice Pyne, who helped me begin my atomic force microscopy experiments.

There are many people, both in and out of York, who have offered me friendship and guidance during this process. I will forever be indebted to them.

Finally, I would like to thank my family. Without their support, both before and throughout this PhD, I would never have completed this thesis.

DECLARATION

I declare that this thesis is a presentation of original work and I am the sole author. This work has not previously been presented for an award at this, or any other, university. All sources are acknowledged as references and contributions from collaborators are noted where appropriate.

LIST OF PUBLICATIONS

List of published journal articles resulting from work in this thesis

- Yoshua, S. B., Watson, G. D., Howard, J. A. L., Velasco-Berrelleza, V., Leake, M. C. & Noy, A. A nucleoid-associated protein bends and bridges DNA in a multiplicity of topological states with varying specificity.
  Preprint at *bioRxiv* 2020.04.17.047076 (2020). doi:10.1101/2020.04.17.047076

- Yehoshua, S., Pollari, R. & Milstein, J. N. Axial Optical Traps: A New Direction for Optical Tweezers. *Biophys. J.* **108**, 2759–2766 (2015).

- Wang, H., Yehoshua, S., Ali, S. S., Navarre, W. W. & Milstein, J. N. A biomechanical mechanism for initiating DNA packaging. *Nucleic Acids Res.* **42**, 11921–11927 (2014).

List of poster presentations resulting from work in this thesis

- Yoshua, S., Watson G. D., Noy, A. & Leake, M.C., *Investigating the different binding modes of IHF with DNA using atomic force microscopy*. Poster presented at Biophysics of Infection & Immunity Symposium, York, UK, November 2019

- Yoshua, S. & Milstein, J. *Development of Axial Optical Tweezers for Passive Force Clamping*. Poster presented at BPSI Winter Symposium 2017, York, UK, December 2017

- Yoshua, S., Wang, H., Singh N., Navarre, W.W. & Milstein J.N. *Biomechanical Aspects of Gene Silencing in Bacteria*. Poster presented at Chemical Biophysics Symposium 2017, Toronto, ON, Canada, May 2014

- Yoshua, S., Wang, H., Singh, N. & Milstein, J. *The Force Dependent Protein-DNA Structure of H-NS*. Biophys. J. 106, 699a (2014). Poster presented at the Biophysical Society Annual Meeting, February 2014.

INTRODUCTION

Nucleoid-associated proteins are a large family of proteins in bacteria that have a multitude of functions within a cell, including packaging DNA and regulating the expression of genes. These proteins have a wide variety of behaviours to perform these functions, and single-molecule biophysics is well suited to investigate them. In this chapter I describe the bacterial nucleoid, three nucleoid-associated proteins: H-NS, StpA and IHF, and the physics and structure of DNA.

1.1   Single-molecule biophysics

The role of physics in understanding biology was suggested by Schrödinger as long ago as the 1940s. In the decades that followed this came to be realised, creating the new field of biophysics, helping to not just understand biology (as with the structure of DNA [1]) but the fundamental physics underpinning life - a system that , unlike most physical systems, is usually not in thermal equilibrium. In particular the 1970s saw the introduction of the "molecular machine" [2], which is a prime example of biology working at the level of a single molecule.

There are numerous techniques to study the behaviour of a single molecule - often a combination of imaging below the diffraction limit (such as super-resolution microscopy [3–5] or atomic force microscopy (AFM) [6]), fluorescence methods (such

as single-molecule fluorescence resonance energy transfer (smFRET) [7, 8]) and force spectroscopy (such as optical tweezers, magnetic tweezers and AFM force spectroscopy [9]) among others. These techniques have even been combined allowing for both spatial and force data to be collected simultaneously [10–12]. The distinguishing feature is the ability to isolate single molecules in space and/or time instead of taking measurements of an ensemble.

1.1.1   Ensemble vs single measurement

Most biological methods result in ensemble measurements, where the average behaviour of a system is measured. Molecular biology techniques result in ensemble measurements as do many biophysical ones such as many fluorescence techniques (FLIM, FRAP, etc.) as well as nuclear magnetic resonance. Additionally, molecular biology techniques in particular lose many kinetic details as only the final states are measured. Although they are widely applicable, and often give results more readily than single-molecule methods they are not able to measure the distributions underlying the behaviour, just the average value of many molecules. This can be problematic as the heterogeneity of the distribution can reveal existing behaviour that would not be observable in an ensemble, especially as many behaviours happen rarely. This is particularly true if there is a time-dependence to behaviour. For example, the walking of myosin along actin filaments can be measured in bulk to work out the average stroke time or the rate of ATP turnover [13], but a single-molecule measurement will allow the steps to be observed, whether the myosin is walking consistently in one direction or not [14]. Other experiments could determine the mechanism of myosin walking being 'hand-over-hand' (each hand alternating in being at the front) and not the 'inchworm' model (where the myosin slides along the DNA with one hand remaining in front) [15]. Other examples include being able to observe the multiple states of a DNA hairpin [16] or an ion channel [17]. In some cases taking an ensemble-average is not a problem as many biological processes are ergodic, that is the time-average being the same as an ensemble-average, because over time a single particle will explore the entire parameter space. However, there are many biological processes which are non-ergodic [18], such as anomalous diffusion of lipids in a cell membrane [19] or ion channels in a neuron [17], which require time-sensitive single-molecule techniques, such as single-particle tracking. It is the change in behaviour of a single molecule in time that is an incredibly important advantage of single-molecule measurements, especially if the physical, chemical

or biological environment of a single molecule can be altered and its change in behaviour measured, although one needs to make sure the system is ergodic if the result is to be related to an ensemble average.

1.1.2 *in vivo* vs *in vitro* experiments

Life is incredibly complex, even on the level of a single cell and so many experiments are conducted isolated from the cell (*in vitro*), as opposed to in the natural environment of the cell (*in vivo*). A perfect experiment would be able to monitor the behaviour of an organism in its natural habitat. However, even a lab environment is altered from nature. Single-molecule experiments are particularly challenging *in vivo* as in addition to the size of the molecules being on the order of nanometres, there are often tens to thousands of the same molecule present within a cell. In addition, the cell itself is incredibly densely packed as expressed in Figure 1.1. However, microscopy methods, in particular super-resolution microscopy, have allowed single-molecule studies to be conducted on individual cells but even in these cases the molecules of interest are often modified with a fluorescent label of some kind (e.g. by attaching a fluorescent dye or protein, or using immunostaining).

The methods used in this thesis are all *in vitro* methods. These have the advantage of being able to isolate the behaviour of a single protein, not only from others of the same kind but also from the rest of the biological system. This can make measurement simpler as it reduces the noise caused by the cellular environment, or "traffic jams" caused by multiple proteins trying to interact with the same region of DNA [20]. In addition, it allows for greater control of the experiment, but in this case the conditions of the cell often have to be replicated (usually, at least the salt concentration and pH), and in some cases proteins cannot be isolated or molecular crowding needs to imitated. Isolation from the cell can cause changes in behaviour or a protein could exhibit behaviour not present *in vivo*, whether this be due to over-expression or lack of competition, inhibition or co-operation with other cellular mechanisms. Because of this it is important not to over-interpret results from *in vitro* methods without a solid understanding of *in vivo* behaviour. In other words, *in vitro* results are best used to explain (or predict) observations from *in vivo* experiments. They are still incredibly important due to the level of detail they can capture - even if it is just knowing that a process can occur solely through a protein of interest.
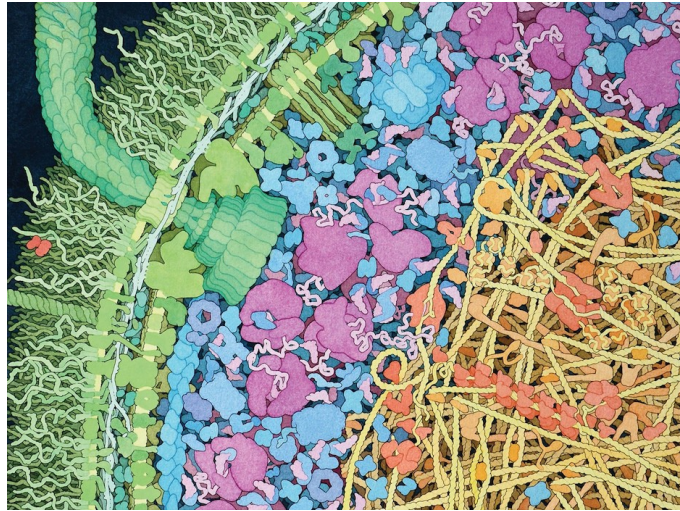
FIGURE 1.1. Artist's impression of the interior of an *E. coli* cell, showing the flagellar motor and membrane (green). The cytoplasm is full of proteins (turquoise), ribosomes and tRNA (magenta) while the nucleoid contains densely packed DNA (yellow) and nucleoid-associated proteins (orange). These proteins are clearly not in solution as with an *in vitro* experiment and small molecules (such as water, salts, glucose and ATP) are also omitted. The image is approximately to scale with a ribosome having a diameter of approximately 20 nm. Image source: [21]

1.2 The physics of DNA

DNA is the information store of life, composed of four bases in sequences that contain genes which encode proteins or non-coding RNA. However, beyond this it also has a physical structure, which has recently come to be considered alongside the underlying sequence. This means the mechanical properties of DNA, in particular its sequence dependence must also be considered. This is particularly true for nucleoid-associated proteins (see below) as their affinity for DNA often depends on the local curvature [22], which is affected by the base pair sequence and when bound change the mechanical properties of DNA.

1.2.1 Polymer physics of DNA

Before looking at sequence-specific effects the bulk properties of DNA must first be understood. Ignoring the differences between base pairs allows us to use models from polymer physics to describe DNA.

(a) Freely-jointed chain schematic

(b) Worm-like chain schematic
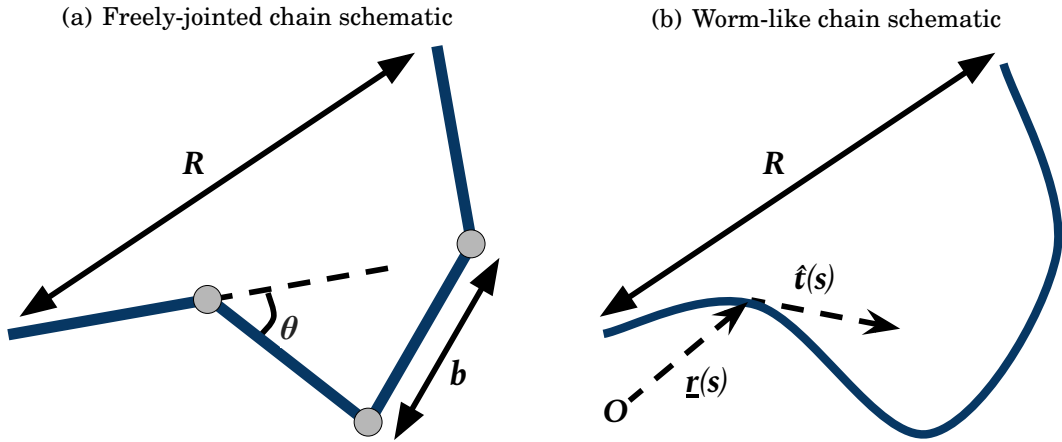
FIGURE 1.2. Diagrams of the two polymer models most often used to describe DNA. The freely-jointed chain is a simple discrete model but only applies at very low forces, while the worm-like chain is a continuous model that is more widely applicable.

The freely-jointed chain The freely-jointed chain (FJC) is the simplest model described here. Although it is not as accurate as the worm-like chain it is simpler mathematically which is useful for for further analysis. It also describes DNA well under low force conditions (for example with tethered-particle motion, described in Sec. 2.2.1).

The model is discrete, consisting of rigid rods of fixed length (b), known as the *Kuhn length*, described by vectors, $\vec{r}$, that have unrestricted rotation at each length (see Fig. 1.2(a)). The Kuhn segments are an abstraction and so much larger than an individual base pair. The exact value depends upon the conditions the polymer is in but is usually around 300 bp or 100 nm.

The contour (i.e. unfolded) length of the chain is therefore, $L_c = Nb$, where N is the number of segments. The end-to-end distance R cannot be calculated directly as it averages to zero as all the segments are independent. This model is also known as the random coil (because it is mathematically the same as a random walk). However we can take the RMS values to get the expected end to end distances.

$$\langle R^2 \rangle = L_c b \tag{1.1}$$

Another common term used is the radius of gyration, R_g. Analytically, this is the RMS displacement of the vectors from their centre of mass, and is used to give

5

an approximate size of the polymer coil. In general, a random walk the radius of gyration is related to the end-to-end distance,

$$\langle R_g^2 \rangle = \langle R^2 \rangle / 6 \tag{1.2}$$

For the freely-jointed chain, we can use Equation 1.1 to get (dropping the ensemble average notation)

$$R_g(\text{FJC}) = \sqrt{\frac{L_c b}{6}}. \tag{1.3}$$

The worm-like chain A more accurate model of DNA is the worm-like chain (see Fig. 1.2(b)). Unlike the freely-jointed chain, this model is continuous and imposes a constraint on the bending by introducing an energy cost. In other words, the interactions between parts of the polymer restrain the direction of different points along its length. This correlation is modelled as an exponential decay, with a characteristic length scale, ℓ_p, known as the *persistence length*, such that going from s to s' along the contour gives

$$\langle \hat{t}(s) \cdot \hat{t}(s') \rangle = \langle \cos \theta(s, s') \rangle = \mathrm{e}^{-|s'-s|/\ell_p}, \tag{1.4}$$

From this we can then extract the mean squared end-to-end distance by taking the integral along the contour, $\vec{R} = \int_0^{L_c} \mathrm{d}s \, \hat{t}(s)$, giving

$$\langle R^2 \rangle = \int_0^{L_c} \mathrm{d}s \int_0^{L_c} \mathrm{d}s' \, \langle \hat{t}(s) \cdot \hat{t}(s') \rangle$$

$$\text{Eqn.\,1.4} \implies \langle R^2 \rangle = \int_0^{L_c} \mathrm{d}s \int_0^{L_c} \mathrm{d}s' \, \mathrm{e}^{-|s'-s|/\ell_p}.$$

This can be solved [23] to get the following relationship,

$$\langle R^2 \rangle = 2 L_c \ell_p \left[1 - \frac{\ell_p}{L_c} \left(1 - \mathrm{e}^{-L_c/\ell_p} \right) \right]. \tag{1.5}$$

In the limit $L_c \gg \ell_p$ this simplifies to $\langle R^2 \rangle = 2 L_c \ell_p$, which comparing to Equation 1.1 shows that the persistence length is half of a Kuhn length. Additionally, for $L_c \ll \ell_p$, we can expand the exponential to the second order, giving $\langle R^2 \rangle = L_c^2$, i.e. the polymer acts as a stiff rod in this limit. Finally, using Equation 1.2 (in the limit $L_c \gg \ell_p$) we get

$$R_g(\text{WLC}) = \sqrt{\frac{L_c \ell_p}{3}}. \tag{1.6}$$

When stretching the worm-like chain the number of states accessible decreases, leading to an entropic force that acts to keep the polymer relaxed. This can be described by,

$$(1.7) \qquad E = E_{\text{elastic}} + E_{\text{external}} = \int_0^{L_c} \mathrm{d}s \left(\frac{A}{2} k_B T \kappa^2 - F \cos\theta \right),$$

where $\kappa = \partial \vec{r} / \partial s$ is the curvature and F is the external force applied. This can be solved to give an approximate formula [24],

$$(1.8) \qquad F(x) = \frac{k_B T}{\ell_p} \left[\frac{1}{4} \left(1 - \frac{x}{L_c} \right)^{-2} - \frac{1}{4} + \frac{x}{L_c} \right].$$

1.2.2 Excluded-volume interactions

The polymer models above treat the polymer as infinitely thin. However, real polymers such as DNA have monomer units which, even if chemical interactions are not considered have a finite volume, leading to steric hindrance for some conformations. This can be characterised by using "self-avoiding" models. These are usually studied using Monté Carlo simulations where the polymer is modelled by a collection of spheres (containing a region of the polymer) which cannot overlap. However, for most experimental cases the original WLC is enough and is used as it has an analytical form. These excluded-volume models are more important in cases where the polymer is more likely to be compacted.

1.2.3 Failings of models

The ideal worm-like chain rarely applies to DNA or other biofilaments [25]. At long length scales the excluded-volume interaction energy becomes larger than the thermal energy, although this applies less for stiffer chains. Even a common DNA sequence of study, the phage-λ genome, which is 48,502 base pairs long does not fully display ideal worm-like chain behaviour [26]. At short distance scales (especially below 7 nm) the exact sequence becomes a lot more important, and interactions between base pairs may have stronger effects such that the WLC fails.

The observed persistence length of DNA is a combination of both the dynamic persistence length, due to sequence-averaged thermal fluctuations, as well as the static persistence length, due to the non-uniform nature of the DNA monomers which can cause local bending [27]. This static persistence length is estimated to

be around ~130 nm, though of course this depends on sequence. As this is longer than the observed persistence length it shows how on a local level DNA can be more flexible than otherwise expected.

Not all differences in measured persistence length are due to sequence. The persistence length of DNA actually decreases with shorter contour lengths. This is because the equation used to analyse the worm-like chain (Eqn 1.8) assumes that $L_c/\ell_p \to \infty$, but in single-molecule experiments the range of L_c/ℓ_p is usually in the range of 6 - 20. The shortening of persistence length (ℓ_p) was modelled to be

$$(1.9) \qquad \ell_p^{\mathrm{WLC}} = \frac{\ell_p^{\infty}}{1 + a\ell_p^{\infty}/L_c},$$

where L_c is the contour length, $\ell_p^{\infty} = 51.51$ nm, and $a = 2.78$ [28]. This result matches an expansion of the WLC known as the finite worm-like chain [28]. This is important to note when comparing results from different lengths of DNA - irrespective of sequence.

Throughout the descriptions thus far the models have treated DNA as an entropic spring, thereby ignoring enthalpic contributions. However, enthalpic contributions do play a role. For example, DNA is negatively charged and so will lead to some electrostatic repulsion. This becomes more important as the DNA is extended to its full contour length. An entropic spring would not be able to stretch further but we know that DNA can be "over-stretched" beyond this point due to changes in the DNA conformation, an enthalpic effect, and so the force-extension behaviour must take this into account at longer extensions [29].

Despite these shortcomings, the worm-like chain remains a useful model to analyse DNA, especially at low forces, and has been shown to apply even on scales as short as 7 nm (or two helical turns) [30], although as shown above it is more flexible at short length scales [31].

1.2.4 Levels of DNA structure

Although the polymer models described in Sec. 1.2.1 are incredibly useful in describing DNA (or analogously to RNA) they do not take into account both the base pair sequence and the shape of the double helix. The complex and diverse sequences and topology are split into four levels of structure as shown in Figure 1.3.
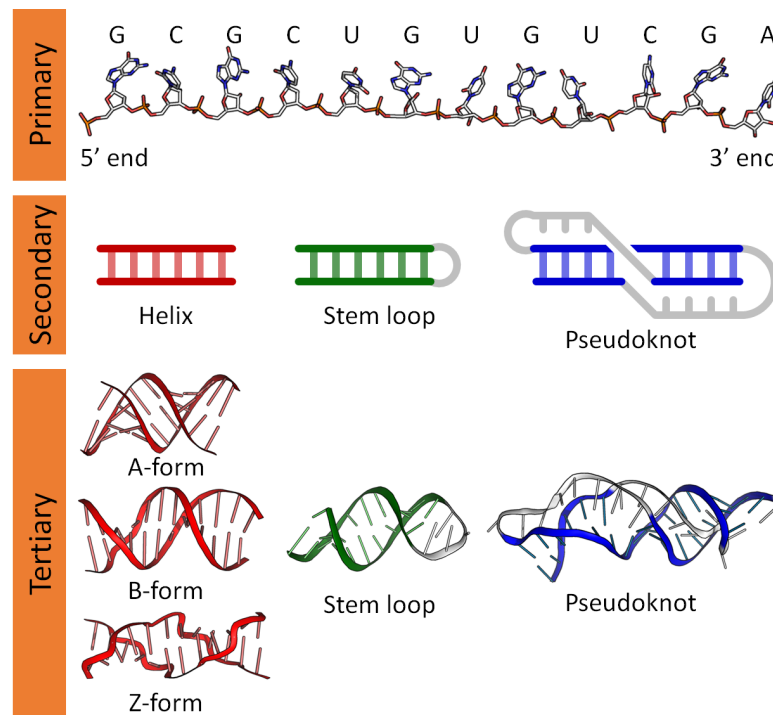
FIGURE 1.3. The first three levels of nucleic acid structure. Red corresponds to DNA and the others are additional forms of RNA. Image source: [32]

The monomer units of DNA are not uniform despite having a similar chemical composition. They consist of four bases: thymine (T)[1], adenine (A), guanine (G) and cytosine (C). These encode the genetic information and form pairs along the DNA-duplex, with adenine forming a base pair with thymine and guanine with cytosine. These base pairs stack along the DNA and, due to their different shapes and bonding (AT-pairs have 2 hydrogen bonds, while GC-pairs have 3 bonds), cause deformations along the DNA - for example AT-pairs and GC-pairs cause different minor grooves in the double helix. Larger sequences of these base pairs, such as extended pairs of AT, known as AT-tracts, change the local structure of the DNA. This allows for recognition or altered interaction with proteins for example. In other words the base pair sequence encodes not just genetic information but also structural information on the DNA itself, which may alter its expression.

Primary structure is the sequence of nucleotides that make up the DNA, described as going from the $5'$ to the $3'$ end of the nucleic acid backbone. It is often

---

[1]RNA has uracil (U) in place of thymine (T), but this still pairs with adenine (A).

listed as the sequence of base pairs and any phosphorylation.

Secondary structure   is the arrangement of the two strands forming double-stranded DNA (dsDNA). For DNA this is just the double helix, though RNA has other structures.

Tertiary structure   is the detailed arrangement of the atoms in space. The handedness, length of helical turn, the number of base pairs within it and the difference between the major and minor grooves of the double helix are described on this level. The canonical form for DNA is B-DNA, though A-DNA and Z-DNA are also found in nature, the structures of which can be seen in Figure 1.3.

Quaternary structure   is the high-level organisation of DNA with other proteins within a cell, i.e. into chromatin. However, prokaryotes do not compartmentalise DNA in the same manner as eukaryotes and the organisation of DNA is less understood, though it involves supercoiling to give rise to some topological domains as well as nucleoid-associated proteins which help to package the DNA so that it fits within a cell.

1.3   The bacterial nucleoid

Bacteria, unlike eukaryotes, do not compartmentalise their DNA within a cell nucleus. Instead the chromosomal DNA is within the cytoplasm of the cell (Figure 1.1). This DNA is also circular, which gives extra constraints, causing some compaction. However, even with this the DNA is too large to fit within the typical dimensions of a bacteria. For example, *E. coli* has a volume of approximately 1 µm^3, but with a genome of approximately 5 Mbp, which would have an $R_g \sim 5$ µm in free solution. Therefore, it is clear that there is further compaction beyond this. Some of this involves excluded-volume effect, and supercoiling as the DNA is circular. However, a large part of it is from nucleoid-associated proteins (NAPs), which together with the DNA form the bacterial nucleoid (see Fig. 1.4).

The nucleoid is not the only source of DNA within the cell. Plasmids are another form of shorter circular DNA that can have multiple copies within a cell. These are passed not only to daughter cells, but also to other cells in a process known as horizontal gene transfer (HGT) (though HGT is not limited to plasmids). This allows

A. Circular *E. coli* genome **B. Random coil of the DNA** **C. Genome organization *in vivo***
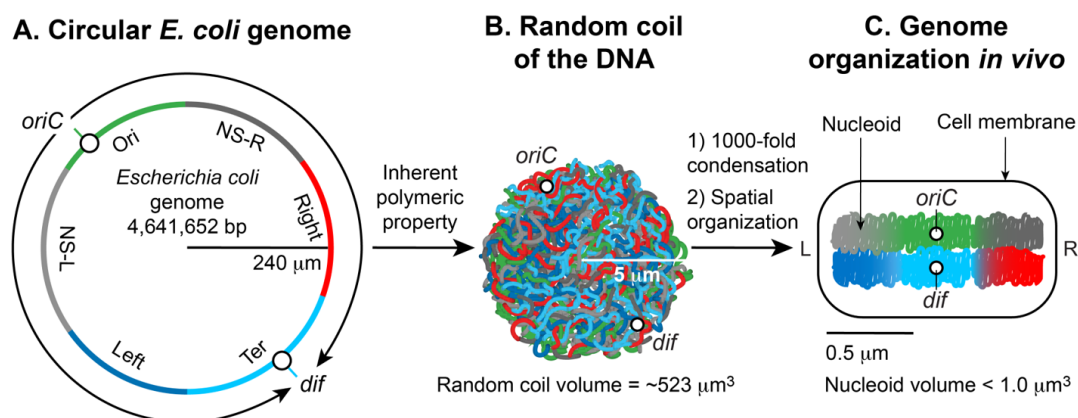
FIGURE 1.4. An example of the importance of NAPs to DNA compaction. A circular *E. coli* genome laid flat would have a radius of 240 μm, but a random coil leads to a radius of a sphere of approximately 11 μm. However, An *E. coli* cell has a *volume* of around 1 μm^3 and the genome is only able to fit due to the compaction by NAPs. Image source:[33].

bacteria to share DNA and genes with each other, leading to horizontal evolution. The same proteins that are involved in the bacterial nucleoid also deal with plasmids and other foreign DNA, especially H-NS (see Sec. 1.4.1).

1.3.1 Forces in the cell

Due to molecular crowding, confinement and DNA-protein interactions the DNA chromosome within a cell is under force at all the time. Electrostatic and hydration forces exist globally while proteins apply forces to the specific parts of the DNA to which they are bound [34]. The DNA backbone is negatively charged, which leads to repulsive forces (which have a Debye length, $\lambda_D \sim 1$ nm [35]), and this is mediated by water and salts in the cell. However, the exact mechanisms underlying this are not well understood, due to the complexity and variety of cellular environments. Proteins further complicate this as they have different charges and alter the shape of DNA. For example, DNA origami experiments suggest nucleosomes (with DNA wrapped in a superhelix around a protein core) have a long range (~ 6 nm) interaction, although this is relatively weak [36].

Proteins can exert far larger forces on DNA than the background interactions. For example, higher forces include those induced by the protein complex that packs

DNA into a bacteriophage capsid, with loading forces in the range of tens of piconewtons [37]. RNAP, with a loading force of around 25 nm [38] is another protein that applies particularly high forces. Proteins that translocate along DNA, unwind it for transcription or replication etc. and typically apply lower forces, such as myosin walking along actin in step-wise movements of approximately 11 nm exerting of 3-4 pN of force [39], typical of molecular motors on DNA [40]. In other words DNA-protein interactions are force-dependent, and so methods than can probe this are useful and may provide information that is otherwise unavailable.

1.3.2   Circular DNA

Most prokaryotes have circular DNA (unlike most eukaryotes, that have linear DNA). This adds further constraints to the DNA as it is now torsionally constrained, which can make the unwinding of the double-helix for transcription difficult compared to a linear strand. However, a circular chromosome has two advantages over a linear chromosome. Firstly, the chromosome is more resilient to incomplete duplication as transcription fails at the ends of linear strands, although this can be somewhat countered by telomeres. Secondly, to counter the strain imposed, the DNA normally forms a higher-order helical structure known as a superhelix. This is known as supercoiling and this alone compacts DNA compared to a relaxed piece of circular DNA. Within bacteria it is thought that this supercoiling might give rise to distinct regions within the bacterial nucleoid. In *E. coli* these are around 10 kbp long and negatively supercoiled. These structures are stabilised by nucleoid-associated proteins (NAPs).

1.4   Nucleoid-associated proteins

Unlike eukaryotes, bacteria do not have compartmentalised cells. One consequence of this is a lack of a cell nucleus and so the DNA is instead located within an irregular region roughly in the centre of the cell, known as the nucleoid. The packaging of DNA is aided by nucleoid-associated proteins (NAPs). These vary in abundance but the most abundant include: H-NS, HU, IHF and FIS. However, unlike the analogous histones of eukaryotes these are not as well preserved across species and are also multi-functional - also being involved in gene regulation and xenogeneic silencing for example. Individually, these proteins are also not vital to cell function [41, 42],
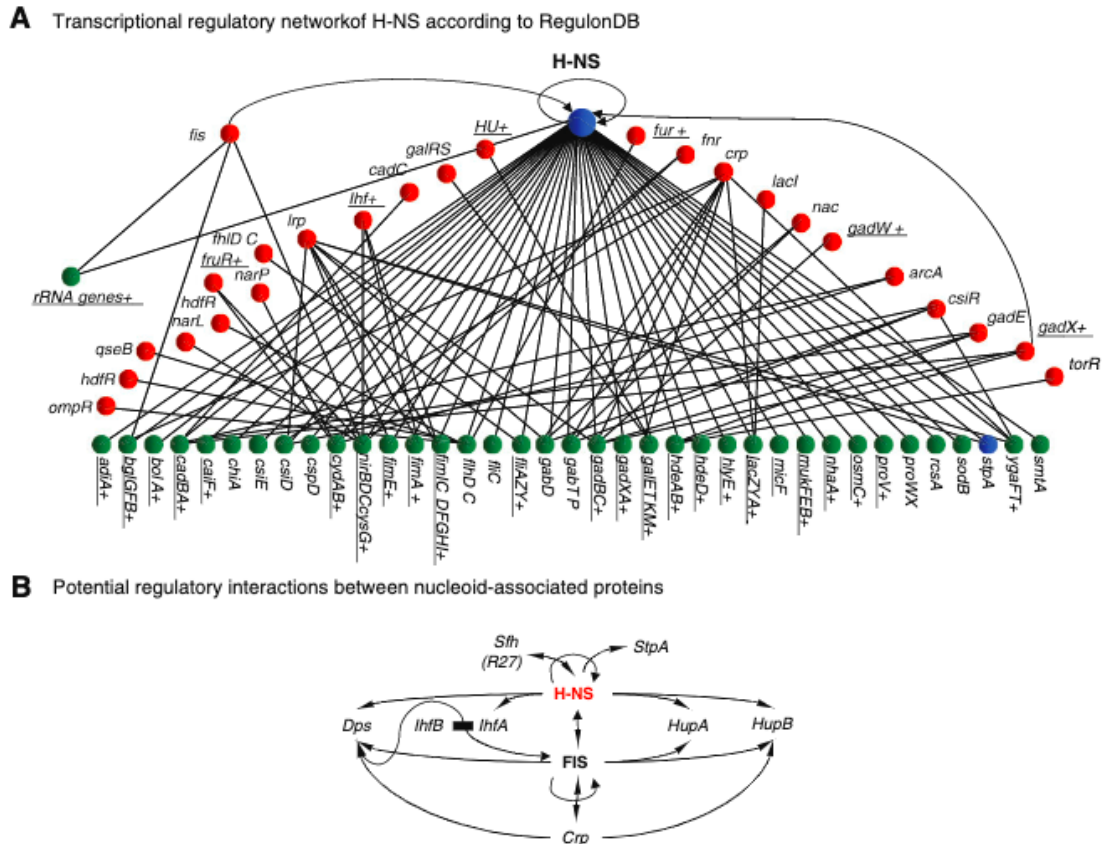
Figure 1.5: (A) The red circles are nucleoid-associated protein (NAP) genes, while the green circles are other genes which H-NS interacts with (those underlined exhibit strong H-NS binding sites). (B) Potential interactions between NAPs. The arrows indicate the direction of the interaction but not whether the protein binding to the promoter sites causes positive or negative regulation. Image source: [51].

perhaps due to the sheer variety of them and the complex network they form (see Fig. 1.5). There are also suggestions that they are not necessary for compaction, but to allow other proteins to access the densely packed nucleoid [43]. Although cells have lower fitness when a NAP is removed they recover due to other proteins being able to compensate and over generations due to mutations in paralogues. Although they are often studied separately it is important to note that they often form complexes together which will likely have effects *in vivo* related to gene expression [44–50].

1.4.1 DNA-binding protein H-NS

DNA-binding protein H-NS is perhaps the prime example of the complexity of nucleoid-associated proteins. It is one of the most abundant proteins in bacteria, with
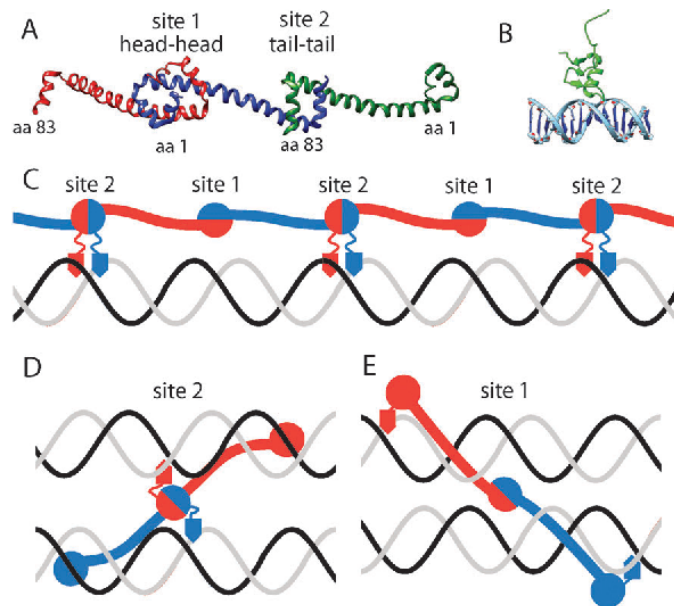
FIGURE 1.6. Structure of H-NS. (A) H-NS has two dimerisation domains, a 'head' domain and a 'tail' domain which can bind to each other as well as (B) a DNA-binding domain that binds to the minor groove. (C) The two dimeraisation domains allow H-NS to form oligomers, creating a filament along the DNA as well as structures which can bridge DNA with a (D) tail-tail or (E) head-head dimer. Image source: [54]

.

approximately 20,000 copies in a typical *E. coli* cell [52] and though it is not essential to survival the fitness of a cell is greatly reduced without it until the bacteria evolves to replace it [42]. It was originally known as Heat-stable nucleoid-structuring protein (compared to HU, the heat-unstable nucleoid-structuring protein) [53], and also Histone-like nucleoid structuring protein, before its multifaceted role was fully elucidated, thus the protein is now preferably known solely by its acronym H-NS.

While H-NS is involved in DNA compaction [52] - forming looped domains within the chromosome [55, 56] - it is also vitally important in a wide range of gene regulatory networks and perhaps more importantly acts as part of the bacterial "immune system", through a mechanism known as "xenogeneic silencing" [57, 58]. H-NS is a global regulator and binds to almost any strand of DNA [53], thereby preventing other proteins from binding, such that transcription cannot occur [59] and "silencing" the gene [60]. The use of H-NS in compaction perhaps also lends support to it being a global regulator, although binding alone is not enough to prevent transcription [61]. Despite it's role in compaction cells can grow without the protein,

albeit more slowly [62].

H-NS binds to most DNA (one dimer per 15-20 bp [63]) but it has a preference for AT-rich DNA or regions [64]. This preference is thought to occur due to an "AT-hook" motif, leading to the DNA-binding region of H-NS fitting better into the minor groove of AT-rich DNA [65] (see Fig. 1.6B). However, this difference is not observable over the genome as a whole (otherwise it would not be able to compact the chromosome) and the overall binding is weak ($K_D = 2.8$ µM [66]). The structure commonly suggested for this compaction is that of Arold et al. [67] who obtained a crystal structure, showing a long filament of H-NS wrapped around DNA forming an super-helical structure, though this is still much larger than a histone. However, this is not the only binding mode of H-NS as it is also possible for it to not oligomerise, but also form bridges between two pieces or distal regions of DNA [56]. It has also been shown that DNA-binding alone is not always enough for gene regulation showing the importance of these higher order structures [61].

Horizontal gene transfer (HGT) is the primary process by which bacteria gain their incredible genetic diversity, allowing for a rapid gene acquisition [62]. The increased binding of H-NS to AT-rich DNA suggests that it forms part of the defence system of bacteria against horizontally-acquired or "foreign" DNA through "gene silencing". Non-genomic DNA, in general, has a higher AT-content compared to that of the bacterial genome [68–70] and this may be why enterobacterial DNA has unusually high AT-content, due to H-NS regulated genes that have been horizontally-acquired [57]. Silencing of genes by H-NS is what distinguishes it from other NAPs, especially as it weakens in response to osmotic or temperature stress [63].

Horizontally-acquired (or xenogeneic) DNA enters the bacterium and is bound by H-NS [58], silencing it. In other words H-NS prevents RNA polymerase (RNAP) from transcribing the DNA [64], although it is not known whether this is through preventing transcription activation or elongation [71]. This is particularly important as AT-rich DNA sequesters RNAP, thereby decreasing global gene expression [72]. The horizontally-acquired DNA may then be activated as over evolutionary timescales random mutations can allow another protein [73] or a strand of RNA [74] to bind to or modify the complex around the horizontally-acquired tract, effectively acting as anti-silencing agents. H-NS can then be removed by RNAP, although it may slow transcription [75]. Temperature can also play a role in modifying the filament by widening it allowing RNAP or another protein to bind [76], allowing for a tempera-

ture stress response. Essentially, a DNA-binding protein can modulate silencing, or a partial paralogue such as Hha [77, 78] or modulating protein YmoA [48, 78, 79] that lack the DNA-binding region, possibly altering the oligomerisation by binding to N-terminal regions [80]. This alteration can occur either through having non-DNA-binding regions or by binding to the H-NS itself [81]. In many cases, silencing cannot occur without a co-regulatory protein such as Hha [80, 82], which can undergo conformational changes in response to increasing temperature, which modulates its interaction with H-NS [46]. In total around 5% of genomic DNA is silenced by H-NS [83].

If a silenced gene is activated and beneficial to the bacterium then it will have increased fitness and become a larger proportion of the population. If it is not, then the bacteria will likely die, or it's daughter cells be out-competed. The prerequisite that mutations occur for this process to happen, facilitated by H-NS, suggests that these regions should have more sequence diversity, which has been shown to be the case [62]. Once incorporated into the genome H-NS then becomes vital for maintaining these genes, as its removal means the gene becomes unregulated [64] and so will be lost (e.g. the Salmonella pathogenicity islands are lost in Δhns mutants of *S. typhimurium* [42]. H-NS is therefore vital for HGT as it is involved in both obtaining and keeping horizontally-acquired DNA [64]. Although the exact reason for the often deleterious nature of these horizontally-acquired genes is unclear, as mentioned above AT-rich genes containing multiple intragenic promoter regions that RNAP can bind to, lowering global non-xenogeneic transcription [75].

Although over large regions of DNA H-NS displays little-to-no sequence specificity there have been extremely short sequences (<400 bp) that show high binding affinity ($K_D = 60$ nM [84]), related to the AT content [57, 42]. However, even for these short regions the binding constant is increased only by a factor of 100 [85], perhaps due to being too short for H-NS to oligomerise [86], as the degree of oligomerisation depends upon the curvature, which requires longer DNA [87]. The lack of the need for oligomerisation for binding has been shown by observing the strong binding of just the C-terminal domain of H-NS (i.e. the DNA-binding region) to certain promoters [86]. This is perhaps unsurprising considering its wide role in gene regulation as well as DNA compaction. It is thought that the difference in binding was primarily due to the local curvature of DNA [88], as AT- and GC- base pairs affect curvature differently (as does the specific sequence) [89, 90]. However, by looking at

genes known the be regulated by H-NS (see Fig. -1.5), Lang et al [51] determined a consensus sequence - tCG(t/a)T(a/t)AATT - and proposed a model where H-NS nucleates at this sites, then oligomerises from these sites, before condensing.

To explain the two binding behaviours of H-NS to DNA the structure must first be understood. Figure 1.6A shows the dimerisation domains of H-NS. The N-terminus of the protein ('aa 1') contains an oligomerisation domain - the 'head', which is thought to be the main dimer-forming region (H-NS is usually a homodimer), there is then a central dimerisation domain (commonly thought to oligomerise), the 'tail', around aa 83) and finally. at the C-terminus, the DNA-binding region [91] (Fig 1.6B). Figure 1.6C shows a cartoon of a filament along a single DNA duplex, where the oligomer forms via alternating head-to-head and tail-to-tail interactions. There are also suggestions that filaments could also join two duplexes in a filament by the each binding site of the dimer joining to a different strand [76]

Figures 1.6D and 1.6E show two examples of bridging, via a tail-tail dimer and a head-head dimer respectively. Both of these functions must have biological significance. Filaments are seen *in vivo* due to the repression of H-NS bound regions of DNA, while bridging is also seen *in vivo* due to the formation of looped domains [22]. *In vitro* single-molecule experiments have shown that the modes can depend upon divalent salt concentration [92, 93]. The divalent salt concentration acts to shield the negative DNA charge, as do some helper proteins. such as Hha in a trimeric complex [94], allowing for functional modification *in vivo* [49, 53]. It has also been shown that the application of force to an H-NS/DNA filament in the presence of Hha or Mg^{2+} can cause compaction of DNA [44].

1.4.2 DNA-binding protein StpA

StpA is a protein that is a paralogue of H-NS. It is 58% homologous to H-NS [96], performs similarly [97] - especially when over-expressed, and is often involved in regulatory pathways with H-NS [98, 99]. This is possibly by interacting with H-NS oligomers [96, 100], especially for *S. typhimurium* [101]. However, StpA is not as predominant in the cell and does not oligomerise in the same way but does form rigid filaments [95].

One example of the interaction of StpA with H-NS is that, in combination with Hha it appears to promote the bridging behaviour of H-NS - helping to further
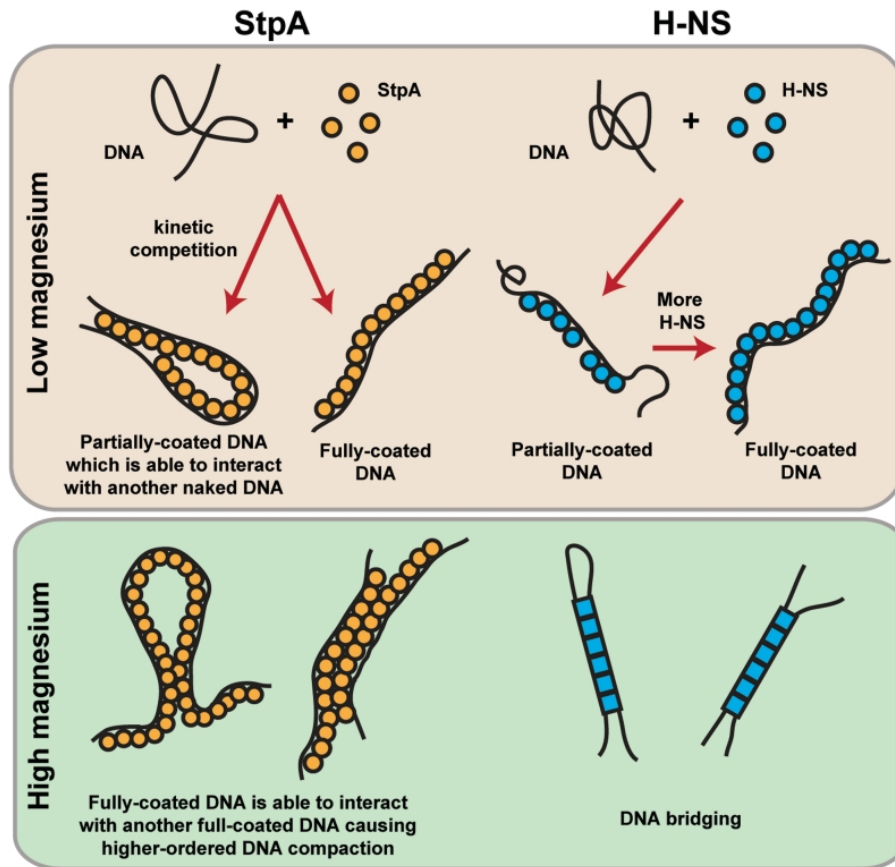
FIGURE 1.7. Comparison of speculative StpA and H-NS binding modes. H-NS can only bridge DNA at higher divalent salt concentration and even then, only along longer filaments, whereas StpA is more likely to bridge, and with more flexible DNA at higher salt concentrations can even form loops. Image source: [95].

compact DNA [102], but more importantly prevent transcription by RNAP. StpA homodimers are more thermally stable than H-NS homodimers but StpA/H-NS hetero-oligomers appear to be more stable than either of these filaments individually [100].

StpA seems to be heavily involved in RNA processes within the cell, as an RNA chaperone [103]. This includes modifying RNA stability [104], promoting RNA assembly [105], altering its splicing and annealing behaviour *in vitro* [105]. It appears to cause strand displacement and this loosening of structure causes RNA to fold [106]. However, despite this, StpA only binds weakly to RNA, mainly through electrostatic interactions and has a preference for disordered RNA [106].
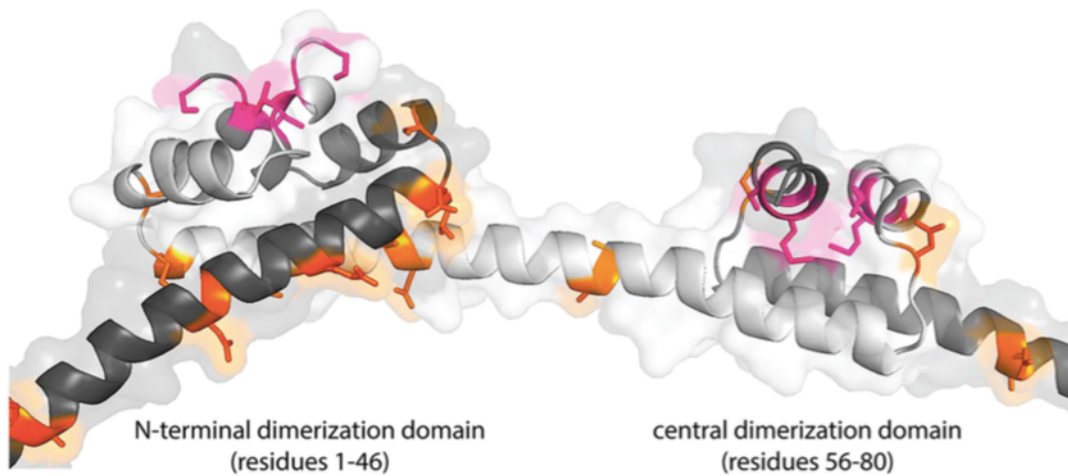
FIGURE 1.8. Locations of point mutations in StpA from Δ*hns* mutants of *S. typhimurium*. The pink positions are those that restored fitness, corresponding to the dimerisation domains. Image source: Ali et al. [42]

StpA binds to DNA with an approximately four times greater affinity than H-NS, with a dissociation constant, $K_D = 0.7$ μM [66, 107]. It has long been known that it can partially replace H-NS, for example as a "molecular adaptor" for truncated H-NS without a DNA-binding domain [108] or by upregulation when H-NS is repressed [109]. However, StpA is present at tenfold less of the amount of H-NS when *hns* is removed from the genome [107].

The binding behaviour of StpA on longer strands of DNA has also observed to be different from H-NS [95] as shown in Figure 1.7. StpA is less likely to oligomerise than H-NS and so competes with bridging behaviour, where each binding site of a dimer binds to different parts of DNA (or different strands completely). At higher salt concentrations StpA appears more capable of interacting with other StpA proteins and so it is suggested that it causes compaction of coated DNA rather than direct bridging.

1.4.3 StpA mutants from evolution of *S. typhimurium*

Sonnenfield et al. [107] showed that in Δ*hns* mutants StpA is up-regulated. Ali et al. took this further by making Δ*hns* mutants of *S. typhimurium* and letting them evolve for 300 generations. Point mutations were observed in the StpA that appeared to restore the bacteria's evolutionary fitness [42]. Figure 1.8 shows the location of

this point mutations. Those that restored fitness were almost all located in the two dimerisation domains of StpA. As StpA is known to not oligomerise as well as H-NS, it is possible that these restore some of the ability to form filaments upon DNA. This is further suggested by the mobility assays shown in Figure 1.9. Note that the DNA in these gels are short enough that the difference in AT and GC binding can be observed. The behaviour of H-NS and wild-type (WT) StpA are shown in the top two gels. H-NS displays co-operative like behaviour while StpA (WT) shows a gradual increase in binding as the concentration is increased. StpA (T37I) has a mutation away from either binding sites (see Figure 1.8) and so behaves like StpA (WT). StpA (A77D) is on the central dimerisation domain, and is thought to lead to a structural change similar to H-NS, as it moves similarly to H-NS on a gel-shift assay. StpA (M4T) has a mutation on the N-terminal dimerisation domain, where StpA usually forms dimers so only has an intermediary effect - with both StpA WT and H-NS behaviour present. These experiments show that even though *hns* is not vital for cell survival this may be because of partial homologues that can rapidly evolve to replicate its functions.

1.4.4   Integration host factor (IHF)

Integration host factor (IHF) is named as such because it was initially discovered aiding in the integration of the the phage-λ. Unlike H-NS and StpA, IHF can bind specifically to certain sequences and so does not form filaments readily, instead causing "kinks" in the DNA - large bends not possible without the presence of a bending protein. These bends have been shown by crystal structure to be at least 160° [110], and very similar to that of another NAP, HU. The consensus sequence, which is bound with nanomolar affinity ($K_D = 5-56$ nM [111]) , is (A/T)ATCAANNNNTT(A/G) (where N is any nucleotide) [112]. However, it can also bind non-specifically with micromolar affinity. IHF is formed of two similar subunits, IHFα and IHFβ. IHFα binds to DNA more tightly that IHFβ. The region 5'-(A/T)ATCAA-3' is bound by IHFα, while two residues, R42 and R46 in IHFβ bind to the minor groove at the end of the consensus sequence, 5'-TT(A/G)-3'. As can be seen, IHF shows a preference for AT-tracts as with many other NAPs.

There are only a few hundred binding sites for IHF in the in the *E. coli* genome and the amount of IHF in the cell vastly greater than required for this (around 55,000 in the stationary phase [114]). Therefore, it is likely that IHF also binds
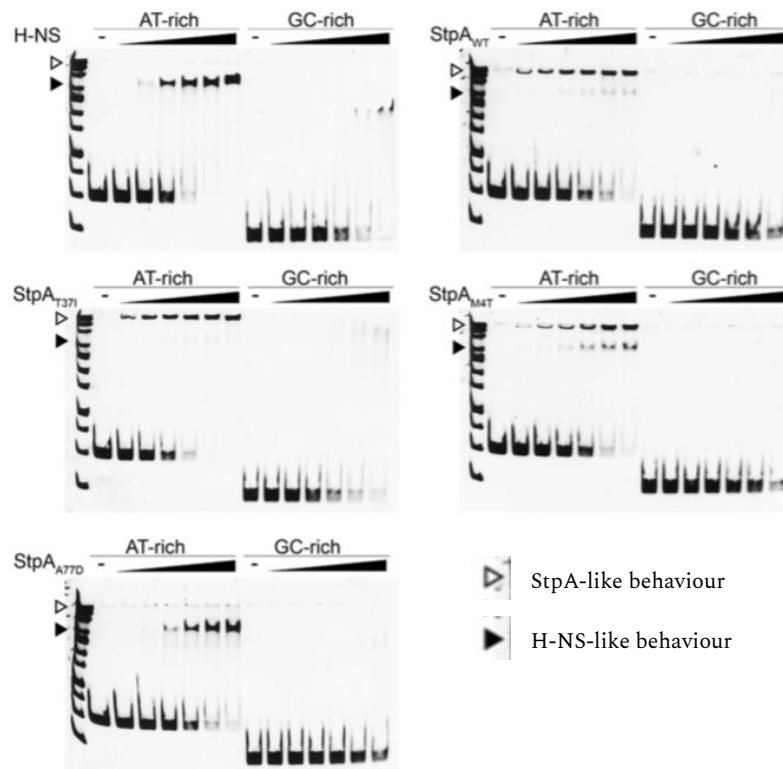
FIGURE 1.9. Electrophoresis gels of DNA/StpA mutant complexes. On DNA
200-300 bp long the difference between binding to AT-rich/GC-rich DNA
for H-NS and StpA can be clearly seen. On the AT-rich DNA H-NS
binds strongly, and with almost a step change suggesting cooperative
behaviour (i.e. filament formation). However, StpA(WT) does not show
this behaviour or any GC-rich binding. The three mutants below show
increasingly H-NS-like behaviour, from T37I which appears WT-like,
M4T which is mixed and A77D which appears almost identical to H-NS.
Image source: Ali et al. [42]

non-specifically in the cell and therefore may also have a role in DNA compaction,
possibly by modifying polyamine behaviour [115] or even alone [116]. In the cell this
may be in conjunction with another (40% homologous) DNA-binding protein, HU,
which generates similar bends and binds non-specifically. The specific binding sites
however, show how IHF is vital to certain genes, for example it is involved in setting
up transcription complexes that start the replication of the genome [117, 118].
It is also involved in the CRISPR-Cas system, by bending DNA allowing for a
secondary binding site on the Cas complex, thereby also aiding in the bacterial
immune response [119]. At high concentrations *in vitro* IHF can also bind non-
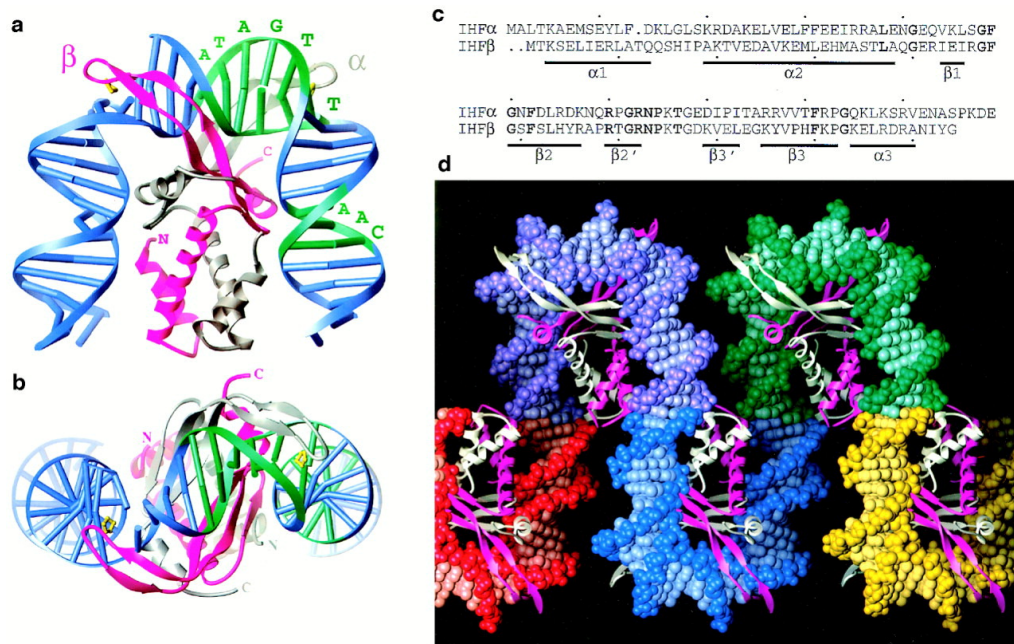
FIGURE 1.10. The crystal structure obtained for IHF shows a sharp bend (a), including a 10-15° bend out of the plane (b). The sequence and secondary structure of the two subunits (c) shows the two 'arms' that bind to DNA as strands 2 and 3. Finally, the crystal packing (d) exhibits bending angles in excess of 180°, although this level of packing is unlikely in a cell. Image source: [113].

specifically, and even bridge DNA, possibly due to their being so much IHF that only one part of IHF can bind to DNA, and not wrap the DNA around it [120]. Additionally, clusters of IHF may help to organise the chromosome [121].

IHF has also been shown to be essential in the formation of some biofilms [122]. A biofilm is a large collection of microorganisms that stick together forming a colony (one common example being dental plaque). This behaviour is activated by quorum sensing, and bacteria in a biofilm behave differently to a less dense environment - becoming more resistant to antibiotics and generally more resilient to environmental conditions [123–125]. The stability of biofilms are dependent upon DNA [126, 127], while *Burkholderia cenocepacia* biofilms were also found to be dependent on extracellular DNA that was bound by IHF [122]. Removal of IHF from the biofilm led to its disruption, suggesting that IHF was stabilising the biofilm in a non-specific manner.

Recent experiments by Connolly et al. [128] have also shown that the binding of
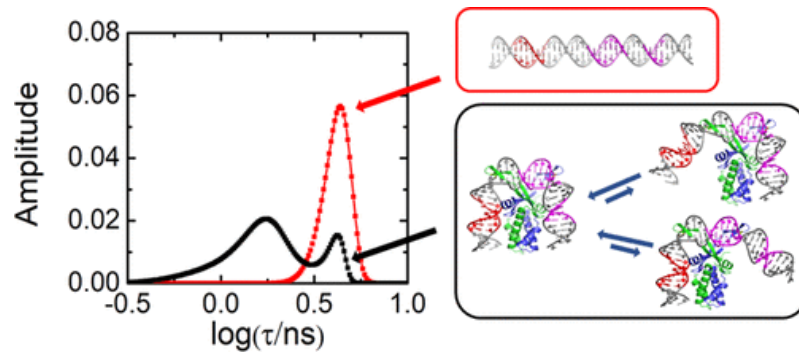
FIGURE 1.11. Fluorescence-lifetime FRET measurements show the introduction of multiple binding modes, where the DNA is partially bent through attachment to one arm of the IHF subunit (with each being of slightly different energy) and the more stable conformation of fully-bound IHF. Image source: [128].

IHF is more complicated than the single sharp (>160°) bend. Fluorescence-lifetime FRET showed that IHF actually has multiple binding modes, including one that is proposed to be partially bent in addition to the "U-turn" described above. As can be seen in Figure 1.11 these modes exist in equilibrium and they suggest that this is to allow some flexibility in IHF complexes may provide a functional role, such as aiding the assembly of the phage-λ integration complex. Although two states can be seen in their model they propose the partially bent DNA could be the DNA attached to either of the 'arms' with slightly different free energies. The multiplicity of these binding modes will be investigated in Chapter 4.

2

EXPERIMENTAL TECHNIQUES

I n this chapter I describe the theory behind the single-molecule techniques used in this thesis: tethered-particle motion (TPM), optical tweezers (OT) and atomic force microscopy (AFM), used to determine the polymer properties of DNA and complexes of DNA with nucleoid-associated proteins.

2.1   Surface-tethered assays

The tethered-particle motion and optical tweezers experiments in this thesis use tethers that are surface-attached. Although in general they are less accurate than experiments decoupled from a surface they can still achieve base pair resolution if required [129]. To be able to perform single-molecule experiments with an optical microscope on DNA, the DNA must first be attached to another object (either the coverslip surface or bead) to be able to hold it in place (although microfluidics are providing ways to overcome this [130, 131]).

2.1.1   Polymerase chain reaction

Polymerase chain reaction (PCR) is a molecular biology technique to make large quantities of DNA (see Figure 2.1). An initial piece of DNA, the "template" is needed, and "primers" are then designed. These are ~20 bp pieces of single-stranded DNA that are complementary to each side of the region of the template that is to be

1 Denaturation at 94-96℃

2 Annealing at ~68℃

3 Elongation at ca. 72 ℃

FIGURE 2.1. Schematic drawing of a polymerase chain reaction. The template DNA (green) is denatured at high temperature. Primers (red) then bind ("anneal") to the separate strands and DNA polymerase can then make a copy of each strand using nucleotides (blue) in solution. This process continues repeatedly, exponentially increasing the amount of DNA. Image source: [132]

amplified, and so can lead to the duplication of either some or all of the template DNA. The primers must be designed to have approximately the same melting temperature so that they anneal to the template at the same point during the thermocycle (see below). They must also not self-anneal or anneal to each other. The primers and DNA template are then added, with DNA polymerase and nucleotides (dNTPs, e.g. deoxyadenosine triphosphate (dATP), which is used to make adenine) to a reaction mix. This reaction mix includes a buffer designed for the DNA polymerase, including Mg^{2+} that acts a catalyst, and additives such as DMSO (which reduces DNA secondary structure). The reaction mix is then cycled through a denaturation step (which separates the template/replicated strands at 95°C). The temperature is then lowered to one that depends on the primers and DNA polymerase (DNAp) being used, to allow the primers to anneal to the template DNA, and DNAp to bind. The temperature is then increased slightly to allow for the DNA polymerase to transcribe the DNA, creating a copy. By repeating this process many times an exponential growth in the desired DNA region is obtained.

TABLE 2.1. Overlap primers for DNA functionalisation

Lam-Bio-F	5′-Biotin-ACCTGATATTGAGTGGCCT - 3′
Lam-Dig-R	5′-Digoxigenin-TCATTCAACACCCGCACTA - 3′

2.1.2 Experimental method

First, the DNA being analysed needs to be functionalised to be able to bond to the microspheres and the glass surface. Rotationally-free bonds are desired (so torsion is not introduced into the system) and the bonds must be stable over long timescales. The biotin-streptavidin bond was first chosen as it is one of the strongest non-covalent bonds [133, 134] and streptavidin-coated microspheres are readily available (Polysciences). For the other bond the antibody anti-digoxigenin (Roche) was chosen as it was found to stick well to the glass coverslip.

To be able to bind to streptavidin and anti-digoxigenin the DNA must first be functionalised to contain biotin and digoxigenin at each end respectively. This was done using polymerase chain reaction (PCR) (Sec. 2.1.1), first with a set of primers that added overhangs and then again with primers that can now be used for any DNA with the overhang added (Table 2.1). The second set of primers contained biotin and digoxigenin at the 5' end, so the molecules would be at each end of the DNA strand. As the DNA was relatively long for PCR (4-5 kbp) LongAmp Taq (New England Biolabs) was used. For the protocol see Section 3.2.

2.2 Tethered particle motion (TPM)

Many single-molecule techniques that are capable of observing a single strand of DNA apply force to the molecule of interest, or fix it in some way. Tethered-particle motion (TPM) is an alternative approach that provides a relatively small disturbance [135, 136] allowing for the the relaxed behaviour of a polymer to be observed. A polymer is attached to an immobile surface at one end while the other end is attached to a microsphere (the "tethered particle") as an optical marker, which can be tracked with nanometre (sub-pixel) precision [137]. The main force applied is therefore only an entropic force [138]. However, this can be reduced by decreasing the size of the microsphere (for example using gold nanoparticles [139]) or even further reduced by using a fluorophore instead of a microsphere as an optical marker [140, 141].

2.2.1 Tethered-particle motion theory

Tethered-particle motion (TPM) experiments determine the end-to-end distance of a polymer and by measuring this over time the distribution can be matched to its polymer properties, such as the length of the contour or its persistence length. The polymer and bead motion is confined to a hemisphere (Fig. 2.2) due to the surface providing a hard barrier. Note that the actual range of motion is less than a hemisphere as the bead has a non-zero volume. The bead creates a volume-exclusion force, which can be calculated. Note that this assumes freely-rotating tether points, that are at equilibrium - though TPM can also be used for dynamic experiments [142, 44].

The larger the bead is compared to the size of the polymer the larger an effect it will have. Segall et al. [138] define the "excursion number", N_R to define two possible forms of motion in a TPM experiment. For a bead of radius, R, and polymer of contour length, L_c, and persistence length, ℓ_p,

$$(2.1) \qquad\qquad N_R \equiv \frac{R}{\sqrt{L_c \ell_p / 3}}.$$

If $N_R < 1$ then the polymer length scales are larger and the motion is dominated by the molecule. However, if $N_R > 1$, then the bead is larger and will constrain the motion. This is based upon a model which takes into account the interactions of the polymer with itself and the surface, the interaction of the polymer with the bead (which are negligible) and finally the bead with the surface. At the length scales of a TPM experiment (on the order of 100-10,000 nanometres), this can be reduced to treating the bead as interacting with a hard surface, and ignoring bead-polymer interactions.

Although TPM provides minimal disturbance it is not strictly force-free. There is an entropic force caused by the excluded volume - the region below the surface. This volume is in fact increased by the bead size as mentioned above. Taking this into account Segall et al. [138] derive the following equations for the bead motion that allow the persistence length to be calculated if the contour length is known (or vice versa) [143]. Measuring the bead position over time allows the expected radius of

bead motion $(r_z, r_\perp)$ to be calculated, from which we can then determine ℓ_p,

$$(2.2) \qquad \frac{\langle r_z^2 \rangle}{L_c \ell_p/3} = 2 + \frac{4N_R}{\sqrt{\pi}\,\mathrm{erf}(N_R)} + N_R^2,$$

$$(2.3) \qquad \frac{\langle r_\perp^2 \rangle}{L_c \ell_p/3} = 2 + \frac{4N_R}{\sqrt{\pi}\,\mathrm{erf}(N_R)}.$$

The force felt by a polymer is then,

$$(2.4) \qquad \langle F_{\text{effective}} \rangle = \frac{k_B T}{\sqrt{\pi}\sqrt{L_c \ell_p/3}} \left(\frac{1 - e^{-N_R^2}}{\mathrm{erf}(N_R)} \right).$$

For a DNA molecule with $\ell_p = 50$ nm and $L_c = 15000$ nm, monitored by a bead of radius $R = 500$ nm, we have $N_R = 1$. This then gives an effective force, $F_{\text{effective}} \sim 3.48$ fN, which is negligible compared to the 0.1-10 pN for most biological forces.

2.2.2 Similar techniques

There are many other techniques that utilise large numbers of DNA tethered at one end. The main advantage of techniques such as TPM and those described below is the large amount of data that can be collected simultaneously, though they do apply force to the DNA tether so cannot be used to investigate relaxed systems.

A methodology known as "DNA curtains" allows for large amounts of DNA to be extended and protein interactions observed. First a lipid bilayer with some chemical modifications for tethering are deposited on a surface. The surface has a "nanobarrier" which prevents lipids from crossing. Therefore, when DNA attaches to a lipid it cannot cross this barrier. Flow is then introduced which creates a hydrodynamic force that both pushes the DNA against the barrier and extends it linearly in the direction of the flow. This then creates a large number of parallel DNA polymers which can then be imaged (with fluorescence microscopy) and proteins can also be introduced. This technique can be improved by adding an anchor downstream of the nanobarrier that the free DNA end can attach to, allowing for a fully extended tether without fluid flow.

Another technique uses a centrifuge to apply force to the DNA tethers. This "centrifuge force microscopy" allows for large forces to be applied to a large number
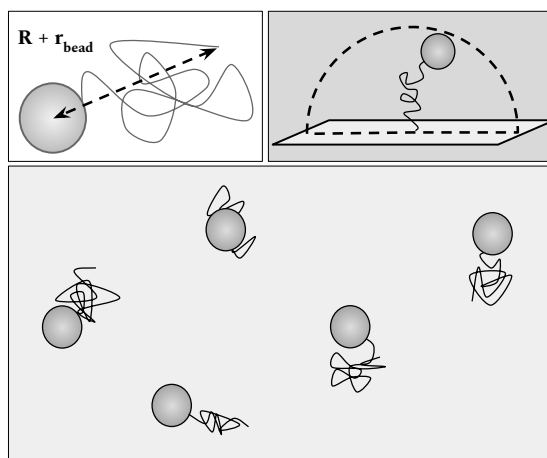
FIGURE 2.2. Schematic of a tethered particle motion experiment. A polymer (DNA) is immobilised to a surface. The free end is then attached to an optical marker (usually a microsphere) that can then be monitored to show the motion of the polymer. Many particles can be seen within a field-of-view (bottom) and each is constrained within a hemispherical region (top right) which does lead to a small entropic exclusion force. By tracking the bead over time the tether point can be determined and therefore the position of the bead (typically with diameters of 100-1000nm) relative to it, giving the end-to-end distance (top left). This is related to the conformations available to the polymer and can be used to calculate the properties of the polymer under nearly force-free conditions.

of DNA tethers. This was first demonstrated by Halverson et al who determined the rate of unbinding of the antidigoxigenen-digoxigenen interaction, well beyond the force levels available to optical trapping (described below) [144]. Yang et al. extended this by allowing for finer control of force and demonstrated this by measuring the force required unzip an artificial DNA loop [145].

2.3 Optical trapping

Optical trapping of micron-sized particles was developed by Ashkin, first by using two beams and overcoming the thermal noise [146], before developing the single-beam gradient force optical trap known as optical tweezers [147]. Optical tweezers are an incredibly accurate technique, capable of accurately applying piconewton-level forces to a polymer such as DNA.
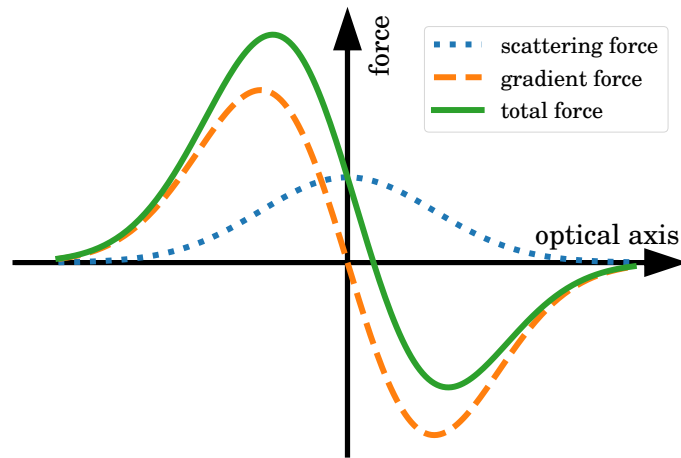
FIGURE 2.3. Forces of an optical trap. Optical trapping is a balance of the scattering force (radiation pressure due to a Gaussian beam) and the gradient force. As can be seen from the green (solid) curve, the equilibrium point is below the focus.

2.3.1 Optical trapping theory

Two optical forces combine to generate an optical trap. These are the scattering force, due to radiation pressure, and a gradient force - due to the change in light intensity at the trap focus. These two forces balance to give an equilibrium position slightly above the trap focus as shown in Figure 2.3. A stronger trap can be generated by increasing the gradient force compared to the scattering force. This is accomplished when the beam is tightly focused by using an objective with a high numerical aperture. Near the trap centre the force scales linearly with distance, in other words it is a Hookean spring, with a trap stiffness κ, where $F = \kappa x$.

The optical forces are best explained using ray optics. When the light rays pass through the transparent microsphere they are refracted, and these cause a net restoring force (Fig. 2.4(a),(b)). For example, if the bead moves to the left, there is greater laser intensity on the right-hand side of the bead, so when refracted it causes a larger force towards the right (i.e. the trap centre) as the net momentum is to the left. In the axial direction the restoring force is caused by a change in the divergence of the laser after the trapped particle. For example, if the bead moves below the trap centre the light becomes more divergent after the particle, decreasing the light momentum and creating a restoring force upwards. This approach strictly only applies when the radius of the particle is much less than the wavelength
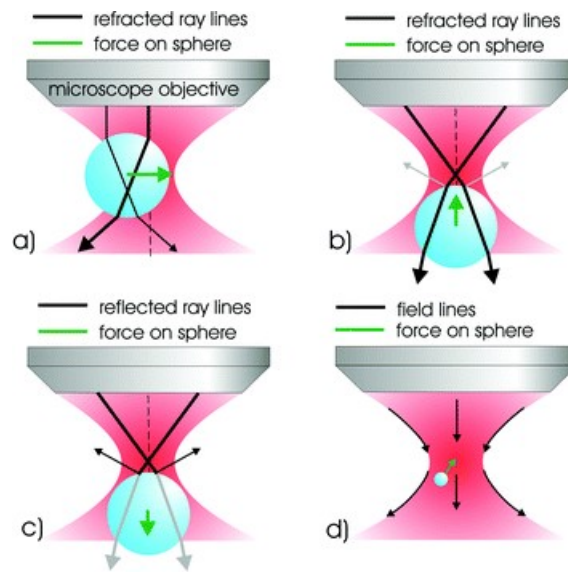
FIGURE 2.4. (a)-(b) A transpararent particle is displaced from the trap and the light that refracts through it causes a net restoring force back to the trap centre. (c) At larger displacements above a trap the radiation pressure causes the trapped particle to "fall out" of the trap. (d) When the particle is much smaller than the wavelength of the trap an electric field approach can be used to explain the trap. An induced dipole from the laser-generated electric field creates a restoring force. Image source: [149]

of the trapping laser. When the particle is much smaller than the trapping laser wavelength Rayleigh scattering generates a dipole as the particle moves away from the trap centre (Fig. 2.4(d)), leading to a restoring force. When the particle size is approximately the same as the laser wavelength neither of these explanations strictly hold true and Mie theory must be used [148]. However, the result is qualitatively the same as these explanations.

2.3.2 The optical potential

The forces applied by optical tweezers are normally modelled by a Hookean spring, and so is a harmonic potential. However, this is an approximation that is only valid near the centre of the potential well generated by a focused laser. In most cases this is all that is relevant because (a) it is this region that is also measured by back-focal-plane interferometry and (b) a free bead will want to fall into this region as it has the lowest potential energy. However, a more accurate approximation of the
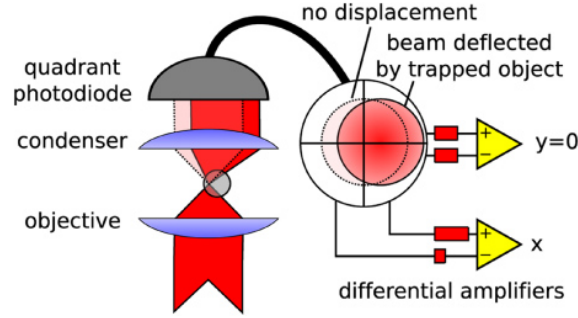
FIGURE 2.5. A quadrant photodiode conjugate to the back focal plane will cause lateral shifts in the laser spot at the QPD allowing the relative position to be measured. The axial position is related to the total intensity, while the lateral positions to the intensities in the four quadrants.

actual optical potential is that of a Gaussian (as most trapping lasers are Gaussian beams). In one dimension,

$$U(x) \propto e^{-(x-x_0)^2/2\sigma_x^2},$$ (2.5)

and so the force is therefore,

$$F(x) \propto (x-x_0)e^{-(x-x_0)^2/2\sigma_x^2}.$$ (2.6)

This can then be approximated as:

$$F(x) \propto (x-x_0)\left(1 + \frac{(x-x_0)^2}{2\sigma_x^2} + \mathcal{O}(x^4)\right)$$ (2.7)

In other words, the force is linear to a first approximation but can also be thought of as a cubic, with a point of inflection and this point of inflection that gives a region that can be used to trap a bead with an approximately constant force [150], i.e. when $(x-x_0)$ becomes comparable to σ_x... the trap width. Note that due to asymmetry in the axial direction, the proportionality factor will be different above and below the trap.

2.3.3 Back focal plane detection

One of the greatest advantages of optical trapping is that back-focal plane (BFP) interferometry can be used. This is a method that allows for nanometre spatial resolution on the order of nanoseconds. This is far higher than those of similar

(a) lateral   (b) axial
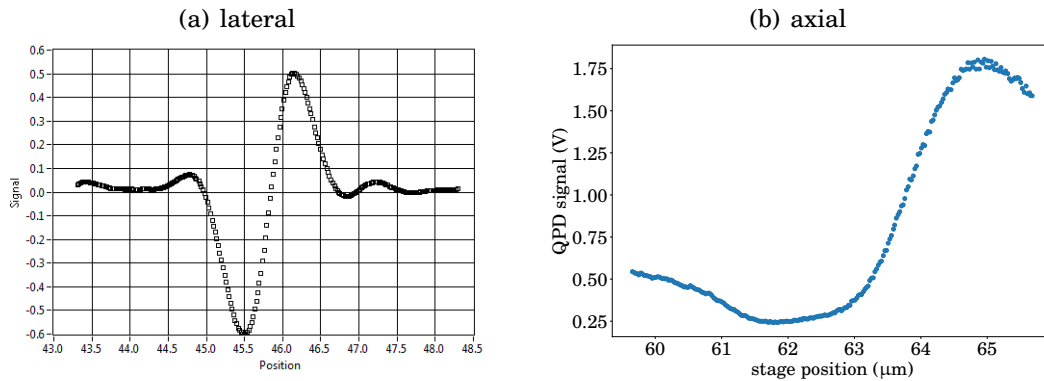
FIGURE 2.6. Example QPD signals when moving a bead across an optical
trap. Around the trap centre the scaling is linear, before turning over
and decreasing as the bead moves out of the trap.

methods such as magnetic tweezers, which is temporally limited to the frame rate of
an imaging camera, so closer to milliseconds.

By using a laser the detection signal can be isolated from the rest of the system.
When using a quadrant photodiode (QPD) in a plane conjugate to the back focal
plane of the condenser in the imaging path (Fig. 2.5) the laser signal translates
laterally as the particle moves across the focus of the laser, as the change in the
amount of refraction causes a lateral translation in the back focal plane. Similarly,
the total intensity changes as the particle moves vertically along the optical axis
because the amount of light collected by the condenser changes.

The relation of the QPD signal to the particle position can be calibrated in
multiple ways. The simplest is to use a piezostage to move a bead in three directions
along the trap, and measure the QPD signals to calibrate the change in signal with
particle displacement (Fig. 2.6). In this case the particle must be held in place (i.e.
stuck to the surface), so care must be taken to ensure the particle is centred in the
trap.

Obtaining a voltage signal using a quadrant photodiode to obtain the sensitivity

33

(β) in x, y and z. The signals in the three directions are

$$S_x = (V_{\text{left}} - V_{\text{right}})/V_{\text{sum}},$$

$$S_y = (V_{\text{top}} - V_{\text{bottom}})/V_{\text{sum}}$$

(2.8)
$$S_z = V_{\text{sum}},$$

where the V_i signals from the QPD for each direction (e.g. V_{left} being the left two quadrants) and they have a non-linear dependence [151] e.g.,

(2.9)
$$S_x = \frac{V_{left} - V_{right}}{V_{sum}} \approx \frac{16}{\sqrt{\pi}} \frac{\alpha k}{w^2} \exp\left[-2\left(\frac{x}{w}\right)^2\right] \int_0^{x/w} \exp\left(y^2\right) \mathrm{d}y,$$

where α is a constant, k is the wavenumber and w the beam waist. However, within the harmonic region of the trap (which we are constrained to), this is an approximately linear relationship, so we can simplify the expression to

(2.10)
$$\Delta r_i = \beta_i \Delta S_i,$$

where β_i is the linear sensitivity of the QPD in a given direction.

2.3.4   Calibrating an optical trap

There are three main methods to calibrate an optical trap, that is to measure the trap stiffness, κ and if using a quadrant photodiode its sensitivity, β.

2.3.4.1   Equipartition method

Close to the centre of the trap the potential is quadratic (i.e. a Hookean spring) in each direction. Within this potential the bead can still diffuse via Brownian motion, though it is constrained by the trap. By using the equipartition theorem we know that each direction has a kinetic energy equal to $\frac{1}{2}k_B T$, so

(2.11)
$$\frac{1}{2}\kappa\langle x^2\rangle = \frac{1}{2}k_B T, \text{ so}$$

(2.12)
$$\kappa = k_B T/\langle x^2\rangle,$$

where $\langle x^2\rangle$ is the mean square displacement of the bead within the trap over time.

This method has the advantage of also being able to be measured with a camera if the pixel size is known, but back-focal-plane detection is often used. Although this method is simple it has drawbacks in that not all of the energy is related to the

Brownian motion of a bead within a trap. A similar method, oscillating the stage so that the bead moves further up the trap can also be used but neither of this methods deal with noise in the signal, or simultaneously give both the sensitivity and trap stiffness, unlike the power-spectrum method described below.

2.3.4.2 Power spectrum method

A more accurate method of calibrating the the trap stiffness is to use the power spectrum of a trapped bead [152, 153]. This can be done with video microscopy [154], but BFP interferometry is usually used. Applying a Fourier transform to the intensity signals from a QPD converts them into the frequency domain, giving the power spectrum. This can be fit by a Lorentzian (Fig. 2.7), derived from the equation of motion of a sphere in a harmonic potential. At low frequencies the diffusion is flat, because the sphere is trapped at long timescales. At high frequencies (short timescales) there is a $1/f^2$ dependence, due to the free diffusion of the sphere within the trap. The full power spectrum can be fit by,

$$(2.13) \qquad P(f) = \frac{D/\left(n\pi^2\right)}{f^2 + f_c^2},$$

where $D = k_B T/\gamma$ is the diffusion coefficient, $n = \{1, 2\}$ depending on whether a one-sided or two-sided power spectrum is calculated, and f_c is the *corner frequency*, the characteristic turnover frequency from trapped to diffusive behaviour. Note that in some cases the fitting can be improved by accounting for frequencies near the Nyquist limit, f_{Nyq}, by taking account of the aliasing that occurs due to having a finite sampling frequency. The form of the aliased Lorentzian is then,

$$(2.14) \qquad P(f) = \sum_{m=-\infty}^{\infty} \frac{D/\left(n\pi^2\right)}{(f + m f_{\mathrm{Nyq}})^2 + f_c^2},$$

which in practice becomes a finite sum. However, as can be seen in Figure 2.7, this did not improve the fitting in this case and in most cases, if the corner frequency is well above low-frequency noise and below the Nyquist limit these regions of the power spectrum can be ignored when fitting.

Once the Lorentzian is fitted, the trap stiffness, κ, and the QPD sensitivity, β, can be determined. The fitted diffusion coefficient D_v is in terms of the QPD signal, and therefore, $D = \beta^2 D_v$, so,

$$(2.15) \qquad \beta^2 = \frac{k_B T}{\gamma D_v},$$
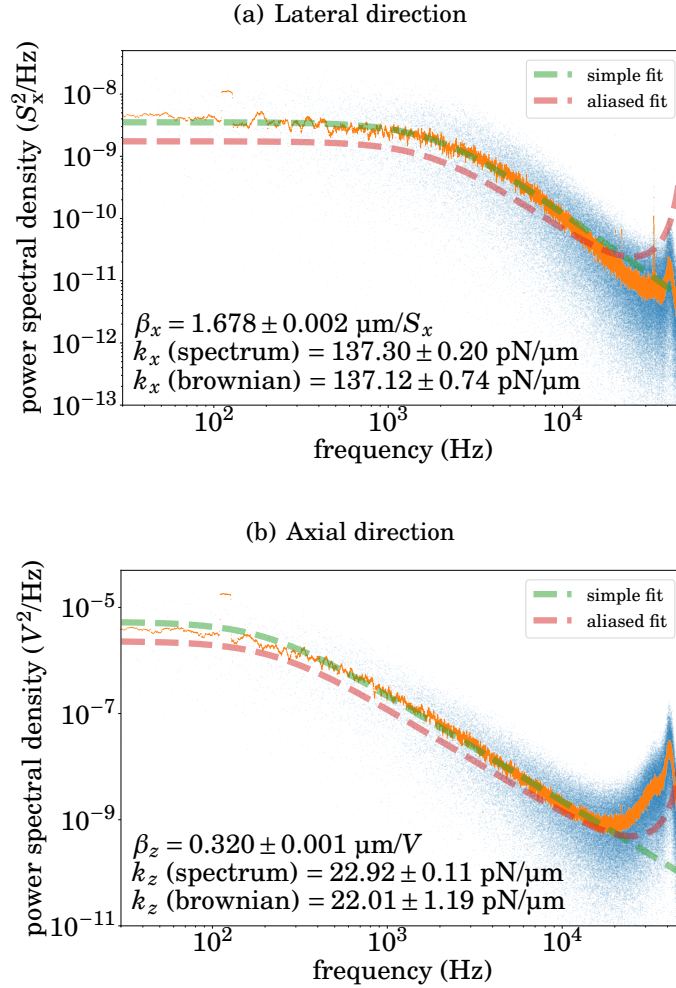
FIGURE 2.7. Example power spectra taken to calibrate the optical tweezers. The raw data (blue dots), was smoothed (orange), before fitting to a Lorentzian (green) and an anti-aliased Lorentzian (red). It can be seen here that for the equipment I used aliasing was not needed to fit the power spectrum well. This can be seen as the calibrated trap stiffnesses using the corner frequency, match that of the Brownian motion, calculated using the sensitivity β that was also derived from the power spectrum. The errors quoted here are the error of the fit, though in practice a standard error from multiple measurements was used to take into account differences in the size of the trapped microspheres.

and the corner frequency, f_c, is related to the trap stiffness, κ, by the equation,

$$(2.16) \qquad\qquad \kappa = 2\pi\gamma f_c,$$

where γ is the drag coefficient, which from Stoke's law, for a bead of radius, r, in a fluid with dynamic viscosity, η ($= 1$ mPa s for water at 20°C) is,

$$(2.17) \qquad\qquad \gamma = 6\pi\eta r.$$

This allows for a quick and accurate calibration of a trap, even for an individual bead in a trap.

2.3.4.3 Surface effects

Near the surface there are additional complications as surface effects increase the drag coefficient (γ) which alters the trap calibration of both the sensitivity and trap stiffness and should be taken into account. This is discussed in more detail in Chapter 5.

2.4 Atomic force microscopy (AFM)

Atomic force microscopy (AFM) is a type of scanning probe microscopy (SPM), a technique that uses a probe - consisting of a tip at the end of a cantilever - that moves across a surface in a raster scan to form an image [155]. By carefully designing a probe and accurately moving it, while reducing background noise sub-nanometre resolution can be achieved. As this is not an optical technique the diffraction limit is not a concern. Therefore, it is a single-molecule technique that is also capable of sub-molecular imaging [156–158], allowing for differences in molecular conformations to be seen in some cases [157]. It is well suited to biological molecules [159] and can even image deformations in the major and minor grooves of DNA [158]. It is also capable of measuring the strength of a single chemical bond [160, 161], or measuring other properties, such as the electric field or temperature [162–164]. AFM can also be used to apply forces to biomolecules [165, 166]. Unlike with optical tweezers, AFM force spectroscopy is normally used with proteins as the force range is 10-10,000 pN (instead of 0.1-100 pN), which would unwind DNA [9].

An AFM probe consists of a cantilever (~100 µm long) with a small tip at the end that makes contact with the surface (with a radius at the end usually <10 nm),
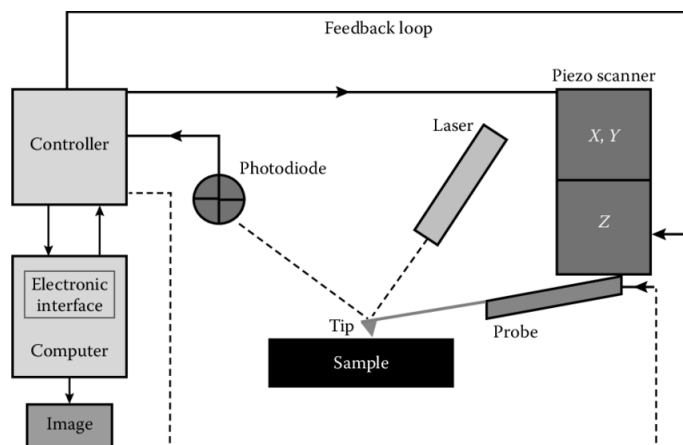
FIGURE 2.8. Diagram of the operation of an atomic force microscopy (AFM). A piezo scanner moves a probe in x and y along a sample. As the tip makes contact with the surface deflections in the detection laser are measured on the photodiode. This is fed into a controller which adjusts the height, z, in a feedback loop to maintain a constant tip-surface separation and an image is generated on a computer. Image source: [167]

that is moved by a piezostage. On the top of the cantilever is a reflective material and a laser reflects from this onto a QPD sensor that is zeroed for the cantilever at rest. When the tip makes contact with the surface this deflects the cantilever, which causes a deflection in the reflected laser beam, which is measured as a translation on the QPD. As the surface is moved relative to the cantilever a height map is determined (Fig. 2.8).

To be able to get an accurate height map an atomically flat surface should be used, that the molecules of interest are deposited on. The most common surface for biological AFM samples in mica, as it is relatively simple to make them flat by cleavage with adhesive tape. However, mica is negatively charged, as is DNA, so there must be some modification to mica or screening of the charge to allow the DNA to bind to the surface. The simplest method is to use divalent salts (such as Mg^{2+} or Ni^{2+}). However, increased charge can introduce increased static bending of ~5° for each nucleotide, although this is not seen with magnesium alone [168]. Other methods involve modifying the surface, such as using poly-L-lysine, which is positively charged, to coat the surface. However, poly-L-lysine is a large molecule so its deposition onto mica can make the surface less uniform, although it has been suggested that low molecular weight poly-L-lysine has a similar roughness to

mica [169]. Chemical modifications are also common, such as AP-mica, formed by silanising with APTES, which creates a smooth surface by covalently bonding to the hydroxyl groups on the surface of freshly-cleaved mica [170, 171]. This creates a weakly positively charged surface, that has also been found to alter the DNA conformation [172, 173, 170, 174, 171]. However, despite the more complicated method involved due to siliansing, AP-mica allows for a wide variety of molecules to bind to the surface in a variety of buffers.

Although AFM is capable of single-molecule imaging, care needs to be taken to evaluate the exact values. The image obtained is that of the surface at each pixel convolved with the much larger AFM tip. In some cases, the shape of the tip can be determined and be deconvolved [175–177] if required. For extended polymers, the perpendicular position of the polymer can be estimated with quasi-subpixel resolution by fitting a Gaussian to the cross-section of the height profile along the contour [178].

Theoretically, AFM can work in any environment as the specific interaction between the surface and the tip does not matter [179]. The simplest method is to dry the sample and image in air (vacuum is also an option). Nanometre resolution is possible but drying can alter the sample. For example, the measured height of DNA is approximately half that of solution (0.7 nm vs 1.4 nm), in part due to the layer (of e.g. salt) that the DNA binds to [180, 181], but primarily due to tip and surface/sample interactions. As shown in Figure 2.9, there are long range interactions between the tip and the sample, which cause an effective interaction area, which broadens the peak in height, lowering the volume and increasing the width [182]. This is particularly relevant when the lateral sample width is less than the interaction area, as is the case for DNA.

Ideally, biological AFM would be conducted under liquid. This allows for dynamic information to be obtained and is closer to the native environment of DNA. However, as the cantilever of the probe is now submerged its properties are altered [183–185]. When these conditions are taken into account liquid-AFM can reach a far greater resolution than AFM in air [186, 158, 179].

As most commercial atomic force microscopes have reduced noise to the thermal limit (e.g. by acoustic isolation) [188, 189] the resolution of AFM is determined by the interaction of the tip and sample. There are many different probes available, of different sizes and shapes. The shape and material of the tip can affect the
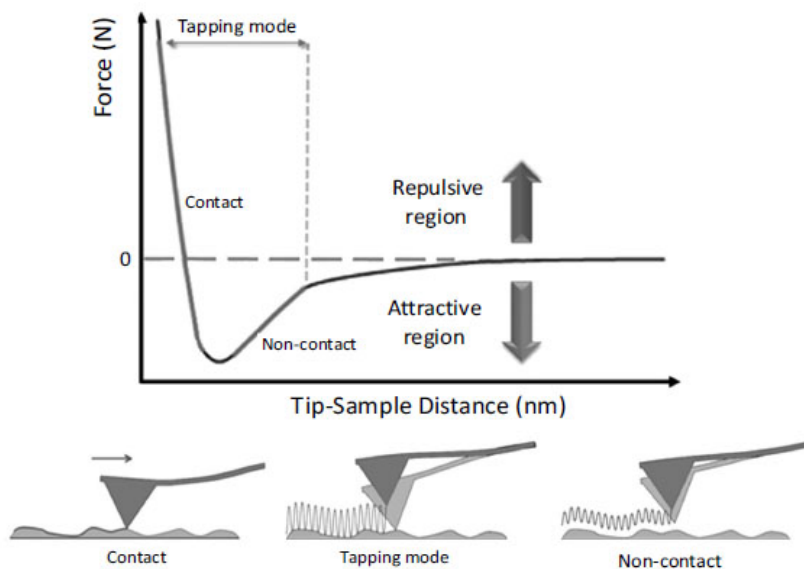
FIGURE 2.9. (Above) A schematic of the force-distance relationship between a sample and tip, composed of the short-range repulsive forces and the attractive *van der Waals* interaction and the regions that different AFM modes operate in. (Below) A schematic of how the tip moves in three different AFM modes. Image source: [187]

interaction with the surface. Ideally, the tip will be sharp enough to obtain detail without damaging the surface (for example a stiff tip will damage soft biological molecules). The cantilever can also be chosen with different stiffnesses (where a higher stiffness directly increases axial resolution [190]) and other properties which can affect the quality of the image. These are discussed in more detail when describing tapping-mode AFM below.

The tip of an AFM probe does not interact purely with the surface of the molecule of interest. For example, there can be salt deposits or other molecules that, as said above, alter the measured height of DNA. This is one reason why liquid-AFM can reach higher resolutions, as solvation lowers these salt effects [179]. In air, the forces involved include long-range *van der Waals* force (which is shielded in liquid), a capillary force from water molecules coating a dried sample forming a meniscus as the AFM tip approaches the surface [190], although this is overcome by tapping-mode AFM (see below). As the tip gets with ~1 nm of the surface short-range forces, such as electrostatic or Born repulsion force also affect the tip-surface interaction [190].

There are three main modes to image with AFM (see Fig. 2.9). The force applied

by the tip is determined by the *setpoint*, and using a PID controller to try and keep this constant while imaging. Contact mode aims to keep the tip at a constant height above the surface (i.e. moving up if the surface height increases). However, this can lead to large lateral forces as the tip drags along the surface [191], distorting the image and damaging the sample. Non-contact AFM keeps the tip of the probe a short distance above the surface [192] and therefore images the force interactions *between* molecules [193], although the oscillations must be kept small enough to not be caught by the attractive forces [194]. Tapping-mode AFM (explained in more detail below) tries to alleviate lateral forces compared to contact AFM by having the tip oscillate at the resonant frequency above the surface so that it only remains in contact with it for a short time [195]. This also has the added benefit of preserving the tip for longer.

2.4.1 Tapping-mode AFM

All AFM experiments in this thesis were conducted in tapping mode, a type of dynamic AFM also known as amplitude modulation AFM (AM-AFM). In tapping mode the oscillation amplitude (as opposed to e.g. frequency in non-contact mode) is varied dynamically by a feedback loop that allows for the interaction between the sample and the tip to be altered in real time. As described above, it has the advantage of lowering lateral torsion, which is necessary for a soft biopolymer such as DNA and the removal of this lateral friction increases resolution [194]. Unlike contact mode and non-contact mode it provides an average force readout across the distance it oscillates over (see Fig. 2.9).

To start in tapping-mode the resonant frequency of the cantilever needs to be determined. The cantilever is rapidly shaken vertically across a range of frequencies to find its resonance (for the tips used around 300 kHz). As can be seen in Figure 2.9 the probe is then driven sinusoidally at this frequency, such that the cantilever acts as a harmonic oscillator. The oscillations are also much larger than in non-contact mode to be able to overcome the attractive forces near the surface [194]. When the tip approaches the surface the cantilever can no longer oscillate fully. The oscillation amplitude is measured by the RMS of the detector signal, and near the surface it decreases. This change can be used to provide information about the height as the probe is moved up and down to maintain a constant oscillation amplitude [196].

The resulting image is primarily affected by the choice of probe and the feedback

parameters. First, there is the choice of tip, where a smaller tip gives better resolution but the increased sharpness can damage soft samples. Next, cantilevers come in different stiffnesses. The spring constant of the cantilever must not be too soft that there is no measurable interaction (or cannot overcome the attractive forces) but also not so hard that it damages the sample. Once the probe is chosen both the amplitude and frequency of the oscillation can be changed if needed. For example particularly rough samples may need a higher amplitude to be able to map the differences in height. Finally, the target amplitude when reaching the surface can be set. This is known as the 'setpoint' (essentially a percentage of the free vibration amplitude that was set above). Varying the setpoint therefore changes how much force is applied to the sample and a balance is needed to get a good image without damaging the sample or tip. There are many sources of noise such as air turbulence or electromagnetic interference that can be reduced with good microscope design, such as acoustic isolation [197]. However, thermal noise will always remain present, particularly in the case of biological experiments which cannot be conducted at low temperatures.

The feedback loops for tapping-mode AFM operate at different frequencies. During imaging the probe is moved slowly along the x and y directions with a nano-positioning stage that is controlled by a slow feedback loop that maintains the height, z, of the tip to maintain the constant setpoint. This allows for the probe to oscillate at approximately the same distance above the sample as the sample height changes. At higher frequencies, the probe is driven near the resonant frequency to keep it at resonance as it moves [198].

CHAPTER

3

DNA-PROTEIN FILAMENT FORMATION WITH H-NS AND STPA

The role of nucleoid-associated proteins (NAPs) are vital to bacterial function but they are not as well-conserved as their eukaryotic counterparts such as histones. Instead, there are many analogues. One such large family is that of H-NS, with numerous H-NS-like proteins. Here the filament formation of H-NS is investigated and compared to StpA, a paralogue with 58% sequence similarity - with differences mainly in the oligomerisation domains, to emphasise the role of oligomerisation in H-NS function. Here I perform tethered-particle motion (TPM) and optical tweezers (OT) experiments on H-NS and StpA filaments formed on DNA and show how they are permanently altered by the application of force by the optical tweezers, and how this behaviour differs depending upon the oligomerisation behaviour.

Contributions from others

- Some data used in Figures 3.6 and 3.8 in this chapter were collected by Haowei Wang.

- The code to analyse TPM and the optical setup were based on that of Haowei Wang.

- The genomic and overlap primers, H-NS, StpA, and the StpA mutants were provided by William W. Navarre.

(a) Tethered Particle Motion   (b) Optical Tweezers
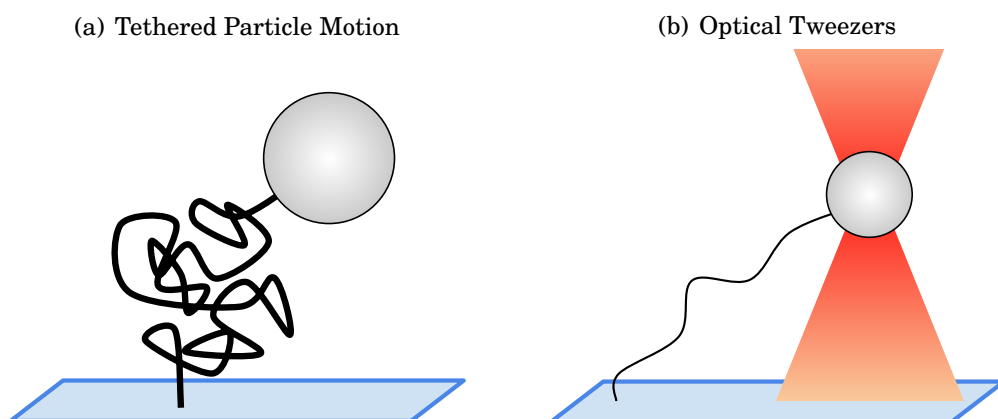
FIGURE 3.1. Experimental Design. A DNA tether is attached to a glass coverslip at one end and a polystyrene bead at the other. The same surface-tethered assays gave bead-DNA tether could be used for both (a) tethered-particle motion experiments and (b) optical tweezers.

3.1 Experimental design

The experiments in this chapter consist of a surface-tethered assay with a single optical trap that stretches the DNA laterally (Fig. 3.1). One advantage of a surface-tethered assay is that it allows for high throughput as many surface tethers can be formed, checked that they did so correctly, and then protein added. However, they are limited in how short the length of the tether can be (see Chapter 5) and for the tether lengths I used are difficult to combine with fluorescence imaging as the trapping laser and imaging laser would overlap and optical tweezers are known to photobleach fluorescent dyes [199].

The optical tweezer setup used is shown in Figure 3.2. All trapping was conducted 1 µm above the surface, which was found programatically by moving the bead downwards using a piezostage until the intensity spiked (indicating the bottom of the bead had hit the surface) and moving it up 0.5 µm above this point (with the other 0.5 µm due to the bead radius). The beads used (PolySciences, Inc.) had a diameter of 1 µm with a variance of 3% and so an average calibration could be used, instead of calibrating for each bead. The calibration was regularly conducted by measuring the power spectra of a large number of beads and averaging (see Fig. 2.7). This was also verified using the Brownian method for trap stiffness (κ) and scanning across a stuck bead for the sensitivity (β). Trap strengths were between
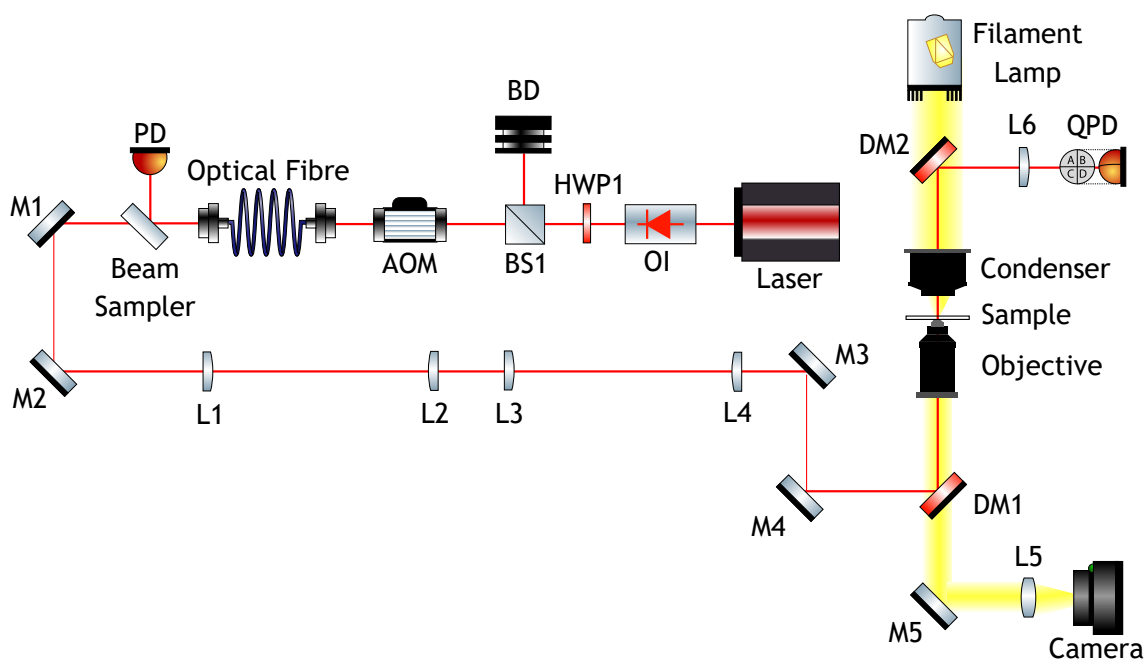
Figure 3.2: Optical setup for tethered particle motion and optical tweezers experiments. A 1064 nm Nd:YAG laser passes through an AOM that is controlled by a microprocessor to adjust the power based on a photodiode after the optical fibre (to reduce power fluctuations). After this, lenses (L1-L4) were used to magnify the beam to slightly overfill the back-aperture of the objective. Back-focal plane detection was achieved via a QPD after the objective.

100-150 pN/μm, so that the forces applied were biologically relevant (on the order of a piconewton).

For these experiments the buffer sometimes needed to be changed, for example to introduce or remove protein from solution. Therefore a simple flow chamber was used (Fig. 3.3) to allow for this. Not adding protein initially was important to verify the integrity of a DNA tether (as in Fig. 3.1) as tethers within a field-of-view could be checked using TPM, by examining the RMS motion. Asymmetric motion would indicated multiple tethers attached to a single bead. A small RMS motion suggests a stuck bead, while a large RMS motion implies non-specific binding or nicked DNA.

First, a bead stock and DNA stocks were made. The beads were washed with repeated steps of centrifugation, removing the supernatant and replacing with a blocking buffer, "HKE". This was composed of 25 mM HEPES, 50 mM KCl, 0.5 mM DTT, and 0.1 mM EDTA, and with 0.5 mg/mL of α-Casein at pH 7.5. 5 kbp regions
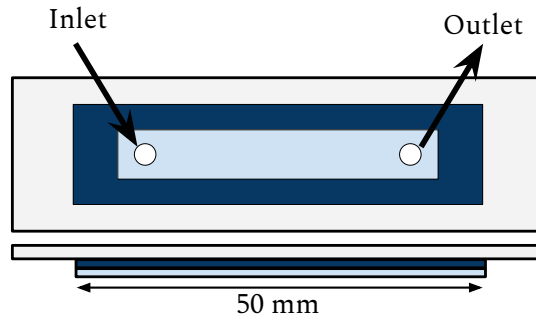
FIGURE 3.3. Chamber design for tethered-particle motion and optical tweezers experiments. Two holes were drilled in a glass slide (grey) and a flow chamber made with a glass coverslip (light blue) by heating parafilm (dark blue), with a cutout in the centre to bond the two. This allowed for the slides to be reusable and a region in the centre large enough that microfluidic flow was not a concern. Parafilm has an approximate thickness of 0.13 mm.
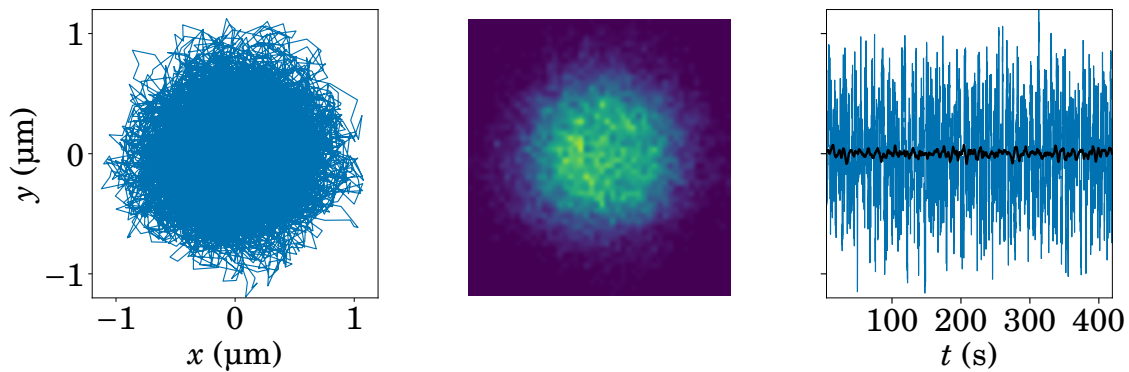
FIGURE 3.4. Example bead motion measured using TPM. The left shows the trajectory of the bead, the centre is a heatmap of the trajectory, while the right shows a time trace of one direction, where the black line is a moving average, showing the drift of the slide, and therefore the fixed tether point, which is then subtracted to calculate the root mean square (RMS) motion.
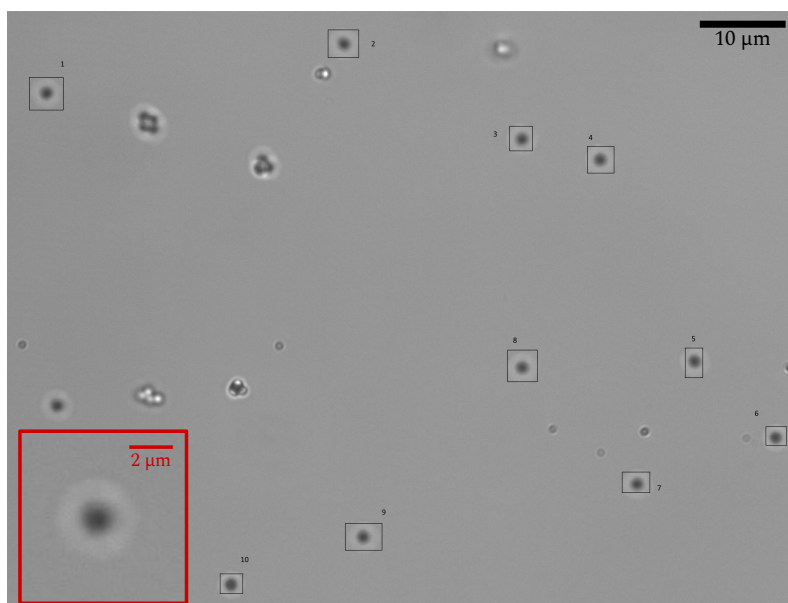
FIGURE 3.5. An example of beads selected for a tethered-particle motion (TPM) experiment. Multiple beads or those which appear stuck are rejected. The black boxes are bounding boxes, the centres of which (using a centroid algorithm) are tracked, to allow the determination of the RMS motion to determine the persistence length, ℓ_p. The image is out of focus to increase the effective size of the bead, allowing for greater sub-pixel accuracy. (inset) a zoom in of a bead.

of DNA (pagC, STM) was amplified from genomic DNA from *S. typhimurium* using overlap primers, before a second PCR was carried out to add biotin and digoxigenin handles (see Sec. 3.2).

To make a flow chamber, 10 ng of DNA was and 2 µl of bead stock solution was diluted in 10 µl of 2×HKE blocking buffer and left for at least 6 hours in a revolver at 4°C. Once the flow chamber was prepared, anti-digoxigenin (Roche) was diluted in PBS to 20 µg/µl and introduced into the flow chamber, then left to incubate for 1 hour at 4°C. The chamber was then washed with 400 µl HKE. After the HKE blocking buffer was added and left for at least 5 minutes to block the surface, leaving only the antibody sites. Finally, the bead/DNA mixture, diluted up to 20 µl was introduced into the slide and left overnight at 4°C. Before the chamber was used it would be carefully washed once more with 400 µl of HKE blocking buffer.

When imaging the DNA a field-of-view would be chosen with around 10-15 beads, so they remained well separated (Fig. 3.5). They were selected first by eye and then

the motion of the beads were tracked for at least 5 minutes and the RMS values (and so persistence length) were determined by following the motion of the bead and drift correcting (Fig. 3.4). Note that the effective force was ~13.8 fN, and so still negligible. If the bead motion was not circular or the persistence length did not match that expected for DNA (~40-50 nm) the tether was rejected. This was repeated for around 6 stage positions to get at least 20 good tethers. After this H-NS or StpA (diluted in HKE) is introduced into the chamber and immediately imaged as it did not need time to incubate. The non-rejected tethers were then measured again using TPM and then stretched using optical tweezers, before once again having the RMS measured for TPM. This then allowed for the persistence length to be measured both before protein, after the addition of protein and after stretching with optical tweezers (an example can be seen in Figure 3.6). The force-extension curve from optical tweezers provided another measure of persistence length as well as the contour length.
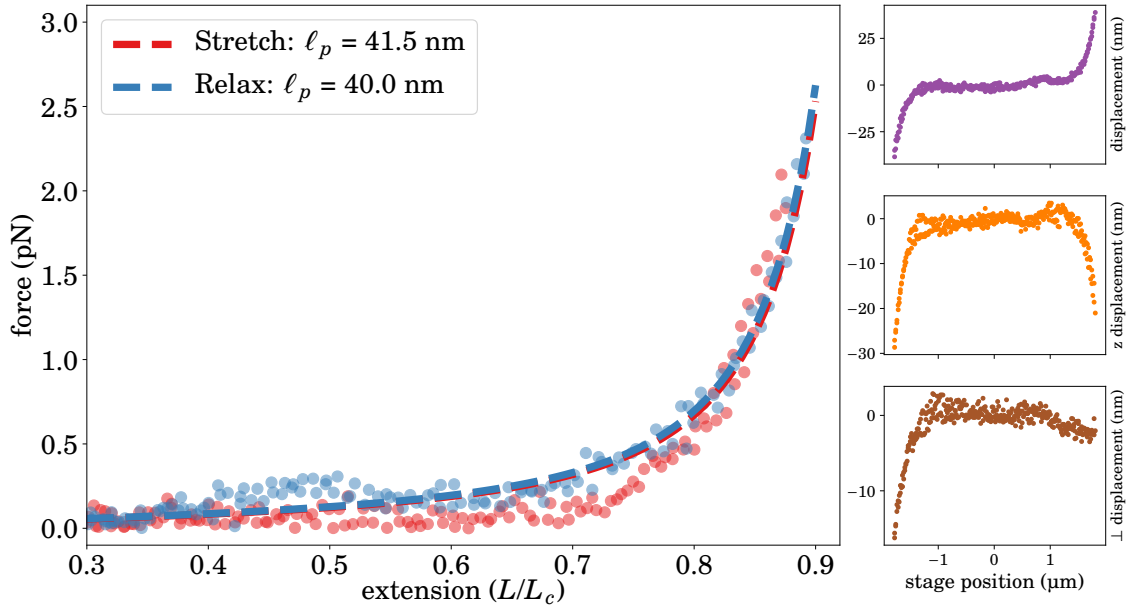
Figure 3.6: An example of a force-extension curve for a 5 kbp (~ 1.7 μm) segment of λ-DNA. The DNA is first centred and then stretched and relaxed in positive and negative directions in either the *x* or *y* axis. The stretch and relax curves are then plotted separately on the left and fitted to the worm-like chain (dashed lines). This gives a persistence length of ~40 nm, within the range expected [29]. The remaining three figures on the right, from top to bottom show the displacement of the bead in the stretching, axial and orthogonal lateral direction. These are what are initially used to centre the curve, and also contribute to the force at the extremes, in particular the axial direction as the tether is short enough relative to the bead size that there is vertical displacement. Note that there is hysteresis between the stretch and relaxation curves. This could be due to the buffer being low salt, so the electrostatic self-repulsion of DNA is not sufficiently screened.

3.2 PCR protocol

To get the genomic DNA fragments two PCRs were carried out. First, genomic DNA from *S. typhimurium* was provided by W. W. Navarre and was amplified to extract the *pagC* region using the two primers, pagC-F and pagC-R in Table 3.1, which not only select the region around *pagC* but also add the overhang sequences. The PCR was carried out with the reaction mix shown in Table 3.2, with the thermocycle as in Table 3.3. LongAmp Taq was chosen as 5 kbp is quite a long region of DNA for Taq DNAp to copy without falling off the DNA or making errors, which LongAmp Taq rectifies. The result can be seen in Figure 3.7.

49

TABLE 3.1. Primers for H-NS/StpA experiments to amplify DNA from the *S. typhimurium* genome and phage-λ. The overhang is italicised to show the overlap with the L5 primers.

Name	Sequence
pagC-F	5′ - *ACC TGA TAT TGA GTG GCC TGC T*CG CAC AGC TGA TTG TTG ATA - 3′
pagC-R	5′ - *TCA TTC AAC ACC CGC ACT ATC G*GA CAG CTT CGC AGG AGA TTT CTA - 3′
L5-Bio-F	5′ - f5Biosg / ACC TGA TAT TGA GTG GCC TGC T - 3′
L5-Dig-R	5′ - f5DigN / TCA TTC AAC ACC CGC ACT ATC G - 3′

TABLE 3.2. PCR Reaction Mix for functionalising DNA sequences

Component	Amount	Final Concentration
5× LongAmp TAQ Reaction Buffer	5 µl	1×
10 mM dNTPs	0.75 µl	300 µM
10 µM Forward Primer	1 µl	0.4 µM
10 µM Reverse Primer	1 µl	0.4 µM
Template DNA (e.g. 25 ng/µl)	4 µl	100 ng (<1,000 ng)
LongAmp Taq	1 µl	5 units/50µl
nuclease-free water	12.25 µl	to 25 µl

TABLE 3.3. PCR Thermocycle for functionalising DNA sequences

Step	Temperature	Time	
Initial Denaturation	94°C	30 seconds	
Denaturation	94°C	30 seconds	⎫
Annealing	52/57°C (overlap/genome)	45 seconds	⎬ Repeat 30×
Extension	65°C	280 seconds	⎭
Final Extension	65°C	10 minutes	

The PCR product was then cleaned using a PCR purification kit (QIAquick PCR Purification Kit, QIAGEN), resulting in a 5 kbp region of DNA, without functionalisation, but with ends complementary to the functionalisation primers. To add the functionalisation another PCR is carried out using the same steps as above, although the annealing temperature is lowered (see Table 3.3) to match the overhang primers, L5-Bio-F and L5-Dig-R.

FIGURE 3.7. Gel electrophoresis of *pagC* amplification from genomic DNA. A bright band at 5 kbp can be seen for the PCR of *pagC* from *S. typhimurium* genomic DNA

3.3   Shorter DNA sequences needed to see sequence dependence

First, the sequence dependence behaviour of H-NS was investigated. The *pagC* gene in *S. typhimurium* is known to be regulated by H-NS *in vivo*, while *STM1033* is not and these regions have high and low affinity for H-NS respectively. Therefore, by taking ~5 kbp regions around these genes, differences in binding should be able to be observed. However, as can be seen in Figure 3.8, no differences in the H-NS binding could be seen with the TPM assay, both show a steady increase in the persistence length of the DNA, corresponding to the formation of a filament of H-NS along the strand, increasing rapidly up to 200 nM and saturating by ~600 nM. Therefore, this assay is not suitable for observing the sequence dependence that is known to exist and shorter sequences are needed to reduce the averaging out of behaviour over the 5 kbp.
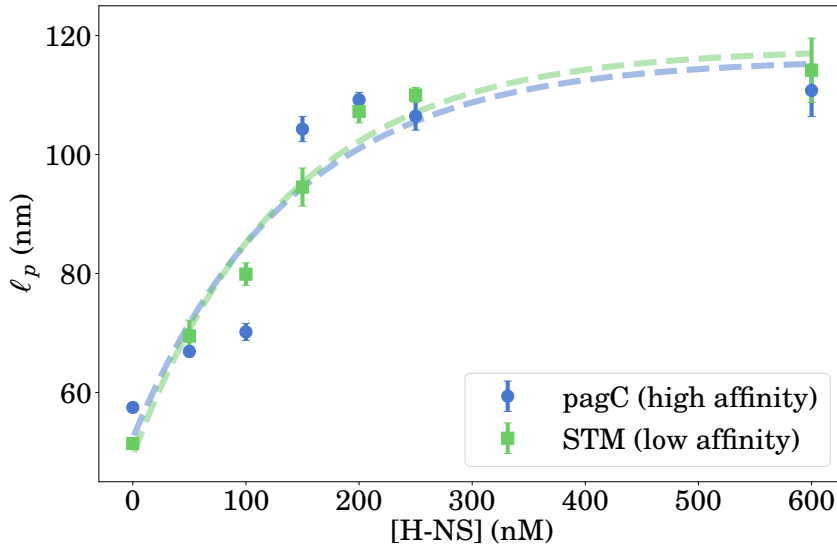
FIGURE 3.8. H-NS was added to surface-tethered DNA sequences of approximately 5 kbp. These sequences contained the *pagC* promoter region or the *STM1033* promoter region. The former is known to be regulated by H-NS and has high affinity, while the other does not. However, in this experiment no difference was observed at a range of concentrations due to remainder of the DNA averaging out any differences. The error shown is the standard error, with $n \sim 15$, and the fits are an exponential rise.

3.4 Stability of H-NS/StpA filaments

The stability of the filaments formed by H-NS and StpA in these experiments were checked by adding the protein to the DNA and then removing it from the solution, by washing with excess HKE buffer and waiting for up to an hour to see if the filaments remained or changed behaviour. As H-NS binds cooperatively by forming long oligomers it is expected to be more stable (i.e. have a slower off-rate) than the binding of StpA which forms a filament as dimers, albeit still cooperatively. Table 3.4 shows that there is no change in the filaments formed by either H-NS and only a slight decrease for StpA, suggesting that once these oligomers form they exist out of equilibrium. In other words, their removal must be through interactions with other proteins or via a biomechanical method, i.e. as part of a gene regulation system or reorganisation of the chromosome.

TABLE 3.4. Changes in root mean square deviation (of bead motion) (RMSD) of a DNA-tethered bead upon addition and removal of NAPs to solution in a TPM experiment. The errors shown here are the standard deviations. $n = 484$ for 0 nM and the range for $n = 6 - 15$ for the steps after.

[Protein]	ℓ_p (nm)		
	0 nM	600 nM	Wash (0 nM)
StpA (WT)		86 ± 14	78 ± 14
StpA (T37I)		87 ± 12	67 ± 6
StpA (M4T)	42 ± 7	93 ± 13	69 ± 4
StpA (A77D)		115 ± 9	89 ± 9
H-NS		94 ± 10	93 ± 8

3.5 Irreversible changes in H-NS/DNA filaments

In the cell DNA is subject to tension due to the interactions with other proteins and other biological processes. Therefore, I used optical tweezers to apply force to pre-formed H-NS/DNA filaments to observe their behaviour as the concentration of H-NS was increased (Fig. 3.9). As with the experiments above a surface-tethered assay was performed and H-NS added at various concentrations, with the quality of a tether checked before and after the addition of H-NS using TPM. Next, optical tweezers were used to apply tension to the DNA and a force-extension curve extracted to measure ℓ_p. This was then confirmed with TPM after (both immediately and up to an hour later, where no change was seen), an example of which can be seen in in Figure 3.10. Similar behaviour was also seen when vortexing preformed H-NS/DNA filaments before measuring with TPM, dropping from 61 ± 7 nm to 44 ± 5 nm, further suggesting it is force that irreversibly alters filaments.

The persistence length of the H-NS/DNA complex markedly decreased after stretching, but not back down to that of bare DNA. For the STM sequence at 600 nM H-NS the persistence length reduced from 114 ± 5 nm to 70 ± 4 nm after stretching, showing the same behaviour. The stability of this new structure suggests that the filaments were permanently altered and could not be reformed as H-NS remained in solution throughout this process and there was no change when more H-NS was added. This is significantly different to another abundant NAP, HU, which is also involved in compaction but is removed after application of force [200], presumably due to the lack of oligomerisation.
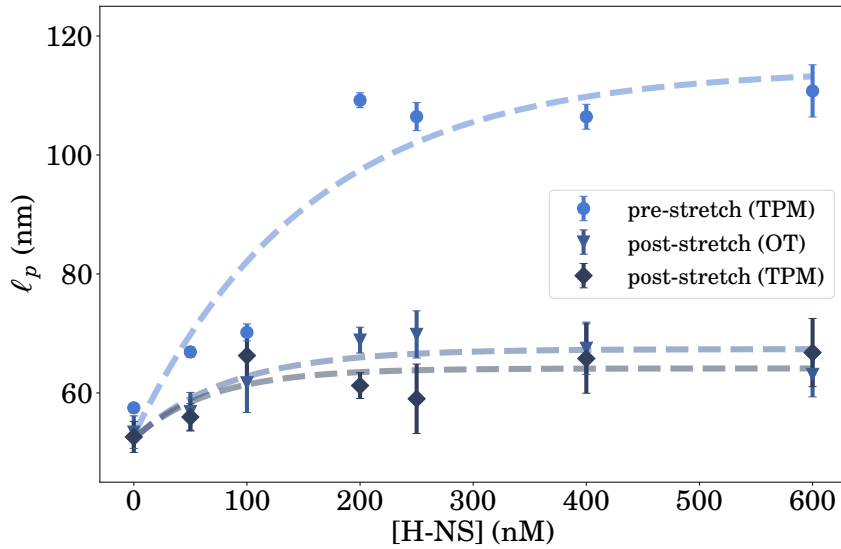
FIGURE 3.9. H-NS was added to DNA at increasing concentration leading
to an increase in persistence length due to the formation of filaments as
measured with tethered-particle motion (TPM). The beads were then
caught in an optical trap and stretched at forces on the order of a
piconewton. The resultant force-extension curve led to a significantly
lower persistence length (ℓ_p), which was verified with TPM. This was
a long-lasting change (at least 30 minutes) despite H-NS remaining in
solution. The fits shown are exponential rises, and the errors are the
standard error with $n \sim 15$.
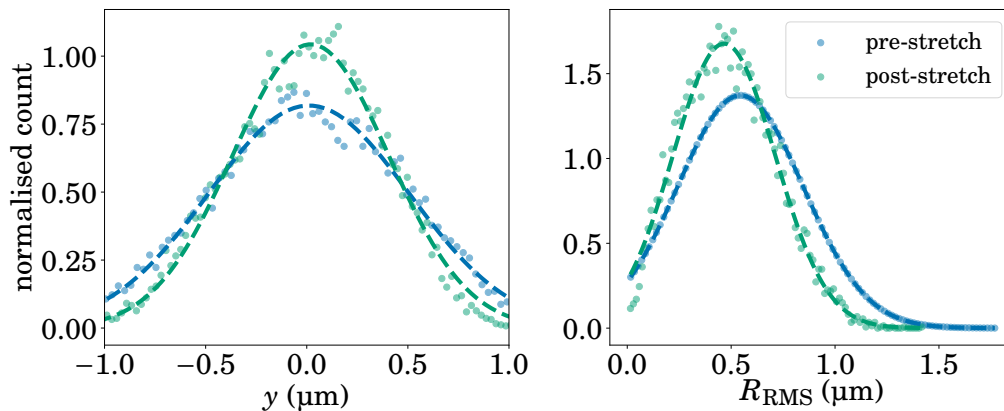
FIGURE 3.10. Change in bead motion for a H-NS/DNA filament after appli-
cation of force using TPM. After forming an H-NS/DNA filament with a
surface-tethered assay the motion of the bead (measured using TPM)
is restricted after stretching with optical tweezers (green) compared to
before (blue). The dashed lines are Gaussian fits of the random motion
of the Brownian motion.

3.6 StpA mutants give insight on H-NS filament formation

For these experiments both a 4 kbp (3096 bp) and 5 kbp (4764 bp) random segment of DNA was chosen from phage-λ, that did not contain a gene regulated by H-NS or StpA. The experiments were similar to above, and so unlike the work by Ali et al. [42] we can look at how filaments form on a longer tract of DNA. The three mutants investigated were all point mutations of StpA, from Δ*hns* mutants of *S. typhimurium*. These were StpA (T37I), StpA (A77D), and StpA (M4T) which, according to Ali et al. [42], behave respectively like StpA (WT), H-NS or somewhere in between respectively (Table 3.5), allowing a full range of behaviour to be investigated.

Looking at the behaviour of StpA with increasing concentration (Fig. 3.11), a gradual increase in the stiffening of the DNA can be seen, as opposed to the steep increase observed for H-NS (Fig. 3.8), which could be due to the lower amounts of oligomerisation, leading to less cooperativity. All of them, except StpA (A77D), cause less stiffening relative to H-NS, while StpA (A77D) shows a similar increase in ℓ_p at 600 nM, but less at lower concentrations - again suggesting that the mutation has given more H-NS-like behaviour, but with less apparent cooperative behaviour. Similarly, looking at the saturating behaviour, we can see that we see the other mutants also have the same behaviour as Ali et al., with the T37I mutant behaving at the wild-type, and M4T behaving somewhere in-between wild-type StpA and H-NS behaviour.

Figure 3.11 clearly shows that at 600 nM protein concentration, StpA (A77D) causes a far greater increase ($\sim 2.8 \times \ell_p^0$ of bare DNA) compared to that of H-NS or any of the other mutants. This could be because it has the greater binding affinity of StpA, combined with some of the oligomerisation that helps H-NS binding. To investigate this further, especially with the intermediate mutant StpA (T37I), I then decided to utilise optical tweezers to apply force to these preformed filaments. Figure 3.12

TABLE 3.5. Summary of StpA mutant behaviour

Mutation	Region of Mutation	Behaviour
T37I	Central	StpA-like
M4T	'Head' Domain	Intermediate
A77D	'Tail' Domain	H-NS-like
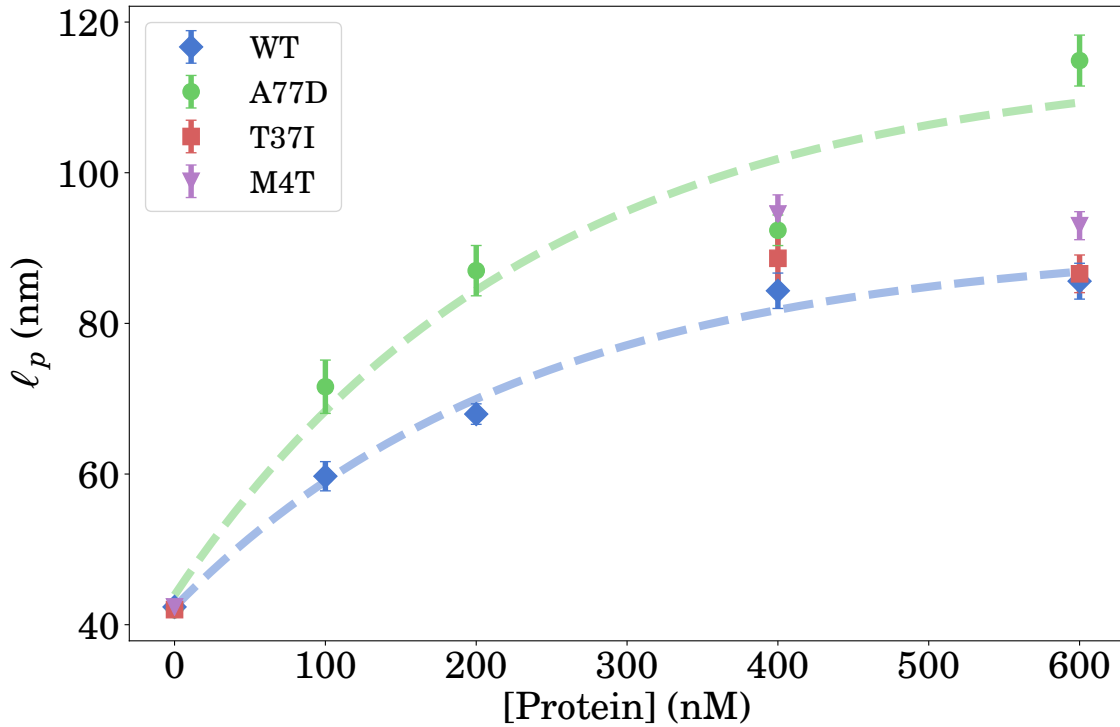
FIGURE 3.11. Wild-type StpA and three mutants formed filaments along the DNA and had their polymer properties measured using TPM, namely the persistence length (ℓ_p). StpA (A77D) clearly performs differently to the others (and has a persistence length increase greater than H-NS), while the other three are approximately the same. The fits are exponential rises and the errors are the standard error with $n \sim 20$.

shows how the persistence length of H-NS and StpA (A77D) protein/DNA filaments drop to a similar amount after stretching, suggesting that the drop is related to oligomerisation as StpA (WT) drops back down to almost that of bare DNA, possibly due to less oligomerisation. The intermediate mutant - StpA (M4T) - seems to behave more similarly to StpA (WT) after stretching, but has a higher ℓ_p before stretching. The head region is usually related to dimerisation so this is perhaps unsurprising.
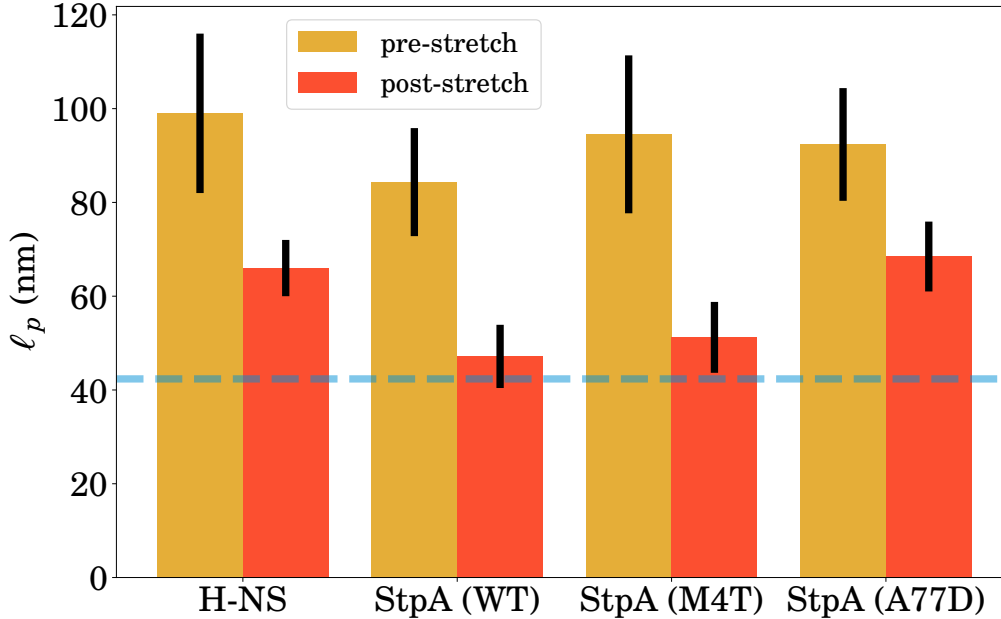
FIGURE 3.12. The behaviour of StpA mutants after application of force measured with TPM. 600 nM of protein was added and filaments allowed to form. The DNA/Protein filaments were then stretched with optical tweezers. The StpA-like variants (WT and M4T) show a larger decrease after stretching than H-NS and the H-NS-like StpA (A77D) , with the wild-type returning to the level of bare DNA (the dashed line). These changes were stable over time, suggesting that H-NS-like proteins behave differently under force than StpA-like proteins, possibly due to the differing oligomerisation behaviour. The error shown is the standard deviation while the ranges were 20-60 for n pre-stretch and 5-15 for post-stretch.

3.7 StpA cannot compete with preformed H-NS filaments

H-NS and StpA form filaments and are known to interfere *in vivo*. Although the behaviour is similar, it does appear that at 600 nM of each protein there is some divergence in the effect on persistence length (see Fig. 3.12). Therefore, I decided perform competition assays adding either H-NS or StpA at 600 nM and then the other once an initial filament had formed. Note that here I report the R_{RMS} values to show the difference due to the non-linear nature of the conversion to persistence length (Eqn. 2.3).

H-NS at 600 nM caused an increase in the R_{RMS} from 430 nm ($n = 484$) to 547 ± 5 nm (standard error, $n = 20$). Adding StpA, led to an $R_{RMS} = 537 \pm 6$ nm ($n = 18$), so there was no change within a standard error. Therefore, it is unlikely that StpA significantly affects H-NS/DNA filaments without other processes. When adding 600 nM StpA first, $R_{RMS} = 532 \pm 4$ nm ($n = 25$), increasing to $R_{RMS} = 553 \pm 6$ nm ($n = 14$) after the addition of H-NS. This increase is larger than a standard error away, but it is still small. Therefore, it is possible that H-NS is interfering with the StpA filaments to a greater extent, and it could be that their interaction *in vivo* requires StpA to be bound first. However, as with the sequence dependence experiments with H-NS, this difference would be more clearly seen on shorter strands of DNA or with additional proteins such as Hha or YdgT.

3.8   Discussion

H-NS and StpA are two closely related proteins that play a vital role in addition to structuring the nucleoid by silencing foreign DNA to protect the cell. The eventual integration of this xenogeneic DNA into the regulatory network of the genome allows for bacteria to rapidly gain genes, including those for antibiotic resistance, via horizontal gene transfer. The many functions of H-NS and its wider family makes it an intriguing protein to study. In this chapter I looked at the filament behaviour of H-NS but, as described in Sections 1.4.1 and 1.4.2, H-NS and StpA can also bridge DNA which provides another avenue to investigate in addition to the interaction with other helper proteins.

3.8.1   Model of H-NS and StpA filament formation

The increase in persistence length of DNA when bound by H-NS and StpA are clear examples of extended filaments forming along DNA. However the permanent change observed after the application of biologically relevant forces indicates that these filaments do *not* form reversibly, and that StpA filaments are either weaker or are composed of dimers instead of oligomers. This is because, unlike H-NS, their persistence length does not remain higher than that of bare DNA, suggesting it is not as strongly bound. The mutants of StpA that alter its oligomerisation behave more like H-NS, further demonstrating the importance of oligomerisation to H-NS behaviour. These results suggest that in the cell H-NS must be removed directly to

access the underlying DNA.

There is some evidence that H-NS does have some specificity, whether for curvature of certain sites or a consensus sequence (although the differences in binding affinity are small). It is also possible that the application of force breaks these filaments and through either steric hindrance or a change in DNA curvature, H-NS does not re-oligomerise (discussed in more detail below). This would leave regions of filament-bounded DNA and naked DNA, corresponding to a lower measured persistence length than a fully-bound H-NS/DNA complex but more than that of DNA alone. Identical experiments, but in the presence of magnesium or the protein Hha, both of which introduce positive charge to screen the negative charge of DNA, allow the DNA/H-NS complex to collapse over time, suggesting the formation of bridges forming from these disrupted filaments only after force is applied [44]. These are examples of how H-NS-bound genes can respond to force, which in the cell could be applied by other proteins, indicating how DNA topology plays a role in gene regulation.

3.8.2 Irreversible changes to H-NS/DNA filaments

As shown in Section 3.5, when H-NS forms stable filaments on the DNA that become permanently altered after the application of biologically relevant forces. One possible explanation, that would need further investigation as it is beyond the sensitivity of this experiment, is that the H-NS/DNA filament fractures under stress, leaving gaps that are either a monomer, dimer or a small number of them, which cannot be filled even if force is no longer applied. An imaging technique, such as fluorescence microscopy, in conjunction with optical tweezers, particularly if it can be super-resolved, could be able to image the H-NS filament both before and after stretching. However, care would need to be taken to ensure that either the addition of a fluorophore or fluorescent protein to H-NS would not alter its activity. If there do not appear to be apparent gaps in H-NS along the DNA this could be because (a) bridging occurred (which is unlikely due to the lack of magnesium and no reduction in the contour length) or (b) The gaps in the filament are too small to be measured. The latter could explain the inability of H-NS to reform a damaged filament, as the DNA would be far less flexible, and H-NS binding is dependent upon curvature. If there are large gaps in H-NS, another possibility could be that the extended filaments can only begin from a nucleation site and become less favourable

if the DNA is no longer completely flexible, or that the differences are between GC-rich and AT-rich regions (if the unbound regions are GC-rich they bind less favourably). Gulvady et al. [84] saw no difference in AT/GC-content but with a nucleation site with $K_D = 60$ nM they did see a three- to six-fold increase in binding affinity. However, they examined DNA hairpins (i.e. single-stranded DNA) and so is not definitive for double-stranded DNA. The role of such promoter sequences and AT-content could be investigated with new DNA sequences, preferably shorter, to allow these behaviours to be isolated using a combination of the techniques described above.

3.8.3 Improving TPM

Although tethered-particle motion is generally considered a force-free technique, the bead, due to it's relatively large size does affect the motion of the polymer, and, at significantly large bead sizes can even dominate the motion. This is particularly an issue for shorter tethers, so the polystyrene microsphere currently used would need to be replaced with smaller tracking particles if the experiments described above and similar experiments are to be performed on shorter DNA tethers. Bead sizes are commonly available with $R = 20$ nm, this gives $N_R \sim 1$ for a 100 bp tether, and a force of 22 fN. There are also limitations on how well sub-pixel tracking precision can perform so low below the diffraction limit. However, smaller beads are usually made of gold nanoparticles and imaged in dark-field to increase signal [201]. Gold nanoparticles can also be combined with TIRF imaging to give information on the height of the bead as well as the lateral position, as the scattering from the nanoparticle will decrease with height [202, 203]. Therefore, by switching to a gold nanoparticle as the tracking particle the effective force will be reduced and height information could also be obtained. It is still also possible to optically trap these particles to apply force in a similar manner as with the polystyrene beads, as gold nanoparticles as small as 9.5 nm have been successfully trapped [204]

An alternative method to TPM is the related tethered-fluorophore motion (TFM), where the microscopic bead is replaced with a fluorophore [141]. The choice between the two would depend upon the timescale of the experiment as the fluorophores can bleach in minutes and so would not be suitable for longer experiments, such as changing buffer conditions or adding/removing protein from solution.

AFM IMAGING OF DNA/IHF COMPLEXES

Due to the specific binding of IHF it does not make large global changes to longer strands of DNA like H-NS. Therefore, shorter strands of DNA with a small number of binding sites are needed. To study this I chose to use atomic force microscopy (AFM) as it is capable of imaging with nanometre pixel resolution. In this chapter I describe my results. Multiple states of binding were found, causing different amounts of bending in DNA. Additionally, when there were binding sites in close proximity to each other, or IHF was in large excess, IHF appeared to bridge DNA, causing clusters instead of bending DNA.

Contributions from others

- The molecular dynamics simulations mentioned here were carried out by George Watson and was used with the experimental data to devise the proposed model (Sec. 4.7.1).

- IHF was provided by Jamieson Howard.

4.1   Experimental method

A mica surface was prepared, which was functionalised with 1-5 kDa poly-L-lysine (Sigma-Aldrich). This functionalisation was chosen over using divalent cations as Mg^{2+} affects IHF binding and other methods such as AP-mica form covalent bonds, altering the structure. First, 20 µl of 0.01% w/v solution, diluted in filtered milliQ
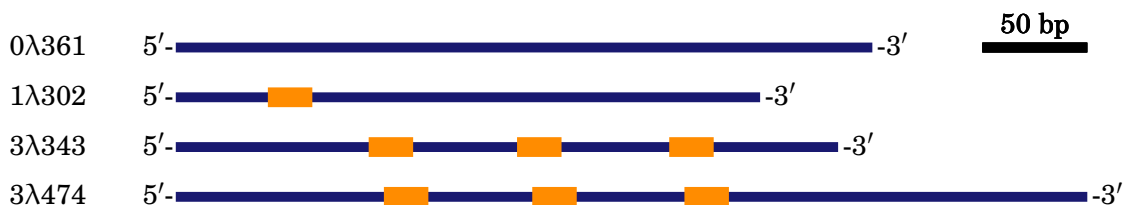
FIGURE 4.1. DNA constructs for AFM imaging with IHF. The lengths of the constructs are to scale (with the length of 1λ302 being 302 bp) and the red squares show the positions of the IHF binding sites. The full constructs can be seen in the appendix (A.2).

H_2O was deposited on freshly-cleaved mica and left for 5 minutes before rinsing with 400-1000 μl of filtered milliQ H_2O and vacuum drying.

While the functionalised mica was drying 20 μl samples with DNA with and without protein were made. A 1 nM concentration of DNA was found to give good coverage of the mica without being overcrowded, corresponding to a fraction of ~4-6 ng of DNA being deposited. This was diluted in a buffer with a final concentration of 10 mM Tris, 50 mM KCl. For samples with protein, the protein was added and left to incubate for 1 hour at room temperature. After, the 20 ul samples were deposited onto the functionalised mica, left for 5 minutes and then rinsed with 400-1000 μl of filtered milliQ H_2O and finally vacuum dried. The samples were then imaged on an atomic force microscope (Bruker Bioscope Resolve) in tapping mode using a TAP300AI-G tip (BudgetSensors) with a 10 nm tip radius. Data were primarily collected as 512×512px images, with a field of view of 2×2μm, resulting in a pixel size of 3.9 nm.

Short sequences (300-500 bp) of DNA from phage-λ were chosen that contained different numbers of binding sites and amplified using PCR (see Sec. 4.2). 0λ3361 is a control with no binding sites, while 1λ302 and 3λ343 have 1 and 3 binding sites respectively (see Fig. 4.1). This length was chosen to allow both the behaviour of a single IHF to be studied and allow for some flexibility in the DNA (being 2-3 persistence lengths long).

Figure 4.2 shows the image processing steps. The images taken were loaded using pySPM [205] (Fig. 4.2(a)) and pre-processed to flatten the image (correcting the slope and background) and removing 'scars', where feedback loop fails because

the AFM tip behaves abnormally, either due to contaminants sticking to the tip or a frictional interaction. (Fig. 4.2(b)). To isolate the individual DNA strands the image was first binarised with a threshold set using Otsu's method, which minimises the variances above and below the threshold [206] (Fig. 4.2(c)). The DNA strands were then separated into individual segments and skeletonised [207] to recover the DNA contour (Fig. 4.2(d)). If present the position of the protein was determined by finding the peak of the height profile of the DNA contour. From the recovered DNA contour the contour length (L_c), end-to-end distance (R), and radius of gyration (R_g) can be determined, where

$$(4.1) \qquad R_g^2 = \frac{1}{N} \sum_{k=1}^{N} (\vec{r}_k - \vec{r}_{\mathrm{av}})^2 .$$

There are two possibilities for DNA adsorbing onto a surface. Either it equilibrates on the surface (and so becomes flat, meaning the conformation is two-dimensional) or it is kinetically trapped, retaining a 3D structure, but held in place by the surface (in this case the positively-charged poly-L-lysine). However, only a 2D projection of this will be measurable.

The two behaviours of DNA can be distinguished based upon their end-to-end distance [208]. The original theoretical end-to-end distance (Eqn. 1.5) for a 3D polymer is reduced by ⅔ when projecting onto a 2D plane.

$$(4.2) \qquad \langle R^2 \rangle_{\mathrm{projection}} = \frac{4}{3} L_c \ell_p \left[1 - \frac{\ell_p}{L_c} \left(1 - \mathrm{e}^{-L_c/\ell_p} \right) \right] = \frac{2}{3} \langle R^2 \rangle_{\mathrm{3D}}.$$

In two dimensions the restriction in bending angles gives $\langle \cos(\theta)_{\mathrm{2D}} \rangle = \mathrm{e}^{-|s'-s|/(2\ell_p)}$ (i.e. the effect of the persistence length effectively doubles when compared to Eqn. 1.4), resulting in an end-to-end distance of [208],

$$(4.3) \qquad \langle R^2 \rangle_{\mathrm{2D}} = 4 L_c \ell_p \left[1 - \frac{2\ell_p}{L_c} \left(1 - \mathrm{e}^{-L_c/2\ell_p} \right) \right].$$

Table 4.4 shows the end-to-end distances for the constructs used in the AFM experiments. Taking 1λ302 as an example, for 100 nm DNA we expect an end-to-end distance, R_E, of approximately 62 nm for a kinetically-trapped DNA (i.e. measuring the 2D projection) or 86 nm for equilibriated DNA (i.e. two-dimensional). Note that the equivalent three-dimensional R_E is between the two at 75 nm. Experimentally, R_E was found to be 69 nm. This is closest to kinetically-trapped DNA, as

(a) original unprocessed image

(b) pre-processed image

(c) segmented image

(d) skeletonisation of a segment
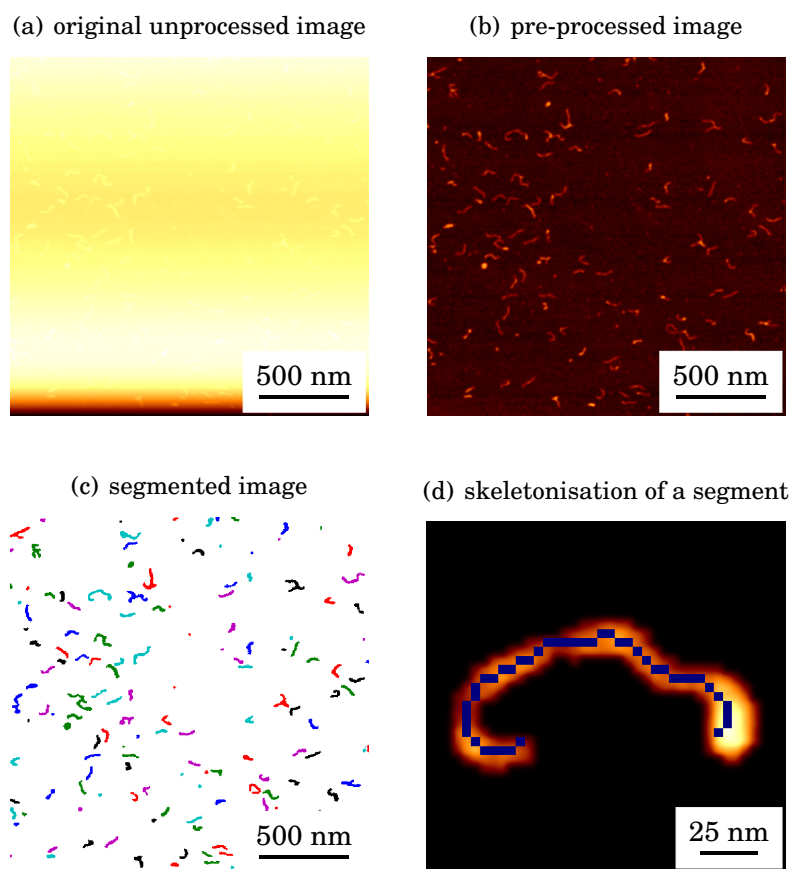
FIGURE 4.2. AFM segmentation and skeletonising. The raw image (a) is flattened (b), then thresholded to isolate the DNA segments (c). Each segment is then skeletonised (d).

expected [169]. It is not a perfect match as the theoretical value assumes a worm-like chain with a persistence length of 50 nm which may not be true, and the DNA contour is determined from a skeletonised image. The poly-L-lysine concentration was also low enough that further compaction of the DNA by the surface modification was not significant in most cases [169].

Measuring volume with atomic force microscopy is not an accurate method, due to the tip being much larger than the molecules being measured and the surface not being totally flat. This usually results in an underestimation of height and an increase in the width. However, zero volumes (the volume above the zero height) are reported for comparison.

To filter the DNA the volume distributions of the isolated segments were first measured (Fig. 4.4). A cutoff was then set depending upon the construct (and the presence of protein) ranging between 2500-5000 nm^3. This is a loose filtering to remove large clumps of DNA or segments of multiple DNA strands. The next filtering step was taken after skeletonisation - allowing those within 50% of the contour length. This was done to filter out unsuitable DNA strands, such as those condensed by partially mobile poly-L-lysine.

4.2 PCR protocol

As IHF is known to interact with phage-λ (as it is its integration host factor) this was selected to amplify short (<500 bp) sequences to image using DNA. A region without any binding sequences was chosen, which also has ~40% AT-content, (0λ361). A construct was chosen with a single binding site, that is near the promoter for the *xis* gene (1λ302), with ~60% AT-content. The final two sequences are different segments around a region with three binding sites in close proximity (3λ343, 3λ474) which have between ~63-70% AT-content. The higher AT-content of the latter three constructs, especially due to the ones with three binding sites are due to consensus sequence being rich in AT, but also AT-tracts increase the local flexibility of DNA. The primers that select these regions can be seen in Table 4.1, while the full sequences can be seen in the Appendix A.2.

The PCR was conducted using Q5 DNA polymerase, with the reaction mix shown in Table 4.2 and the thermocycle in Table 4.3. The PCR product was purified using a

TABLE 4.1. Primers for AFM experiments with IHF to amplify DNA from phage-λ

Name	Sequence
0λ361-F	5$'$ - GCATCATCAAGTGCCGGTCG - 3$'$
0λ361-R	5$'$ - TGCTGTTGGTTGCACTGCTG - 3$'$
1λ302-F	5$'$ - CAAGACACCGGATCTGCAC - 3$'$
1λ302-R	5$'$ - GCATATGATGTCTGACGCTGG - 3$'$
3λ343-F	5$'$ - CTTTGTGCTTCTCTGGAGTGCG - 3$'$
3λ343-R	5$'$ - GGCAGGGAGTGGGACAAAATTG - 3$'$
3λ474-F	5$'$ - GATTGCGAGGCTTTGTGCTT - 3$'$
3λ474-R	5$'$ - CTACCTTTCACGAGTTGCGC - 3$'$

TABLE 4.2. PCR reaction mix for DNA constructs for AFM

Component	Amount	Final Concentration
5× Q5 Reaction Buffer	5 µl	1×
10 mM dNTPs	0.5 µl	200 µM
10 µM Forward Primer	1.25 µl	0.5 µM
10 µM Reverse Primer	1.25 µl	0.5 µM
Template DNA (e.g. 25 ng/µl)	1 µl	15 ng (<1,000 ng)
Q5 DNAp	0.25 µl	1 unit/50µl
nuclease-free water	15.75 µl	to 25 µl

TABLE 4.3. PCR Thermocycle for functionalising DNA sequences

Step	Temperature	Time	
Initial Denaturation	98°C	30 seconds	
Denaturation	98°C	30 seconds	⎫
Annealing	68°C	45 seconds	⎬ Repeat 35×
Extension	72°C	20 seconds	⎭
Final Extension	72°C	2 minutes	

PCR purification kit (QIAquick PCR Purification Kit, QIAGEN) and the result is shown in the gel image in Figure 4.3.
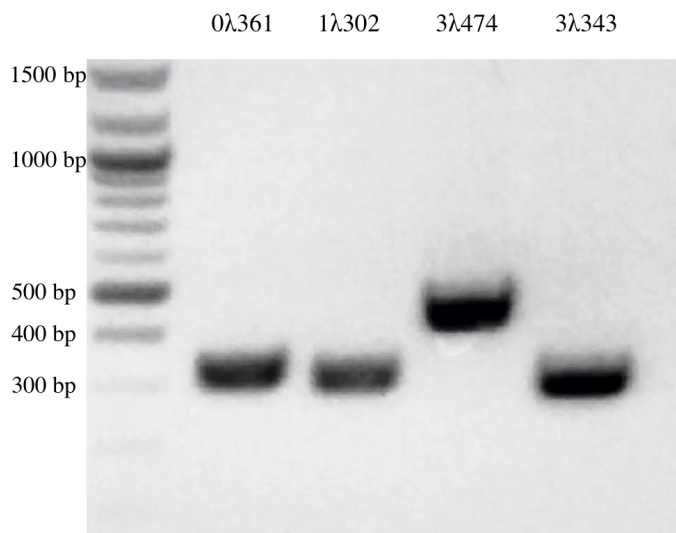
FIGURE 4.3. Gel electrophoresis of short constructs from phage-λ containing 0-3 IHF binding sites. The three constructs are pure and at their expected sizes.

4.3 Changes to DNA conformation upon IHF binding

Looking at the values of the contour length (see Fig.4.4 and Table 4.4) we see that these median measured lengths are less than contour lengths, suggesting that some of the DNA may be in the A-form (which has a lower rise per base pair of 0.26 nm/bp compared to 0.34 nm/bp for B-DNA). The means are as expected: 100 nm for 1λ302, 123 nm for 0λ361, 117 nm for 3λ343 and 161 nm for 3λ474, giving rises per base pair of 0.33-0.34 nm/bp. However, this is to be expected ass the DNA is kinetically trapped, as confirmed by the end-to-end distances. In all the constructs except 3λ343 we see a drop in all of these properties upon the addition of IHF, suggesting a global conformation change that leads to compaction of the DNA, with a reduction in the radius of gyration ranging from 10-17%. 3λ343 appears to behave slightly differently but this could be due to the low number of samples, n, of the negative control or its clustering behaviour (see below), and was excluded from further quantitative analysis.

67
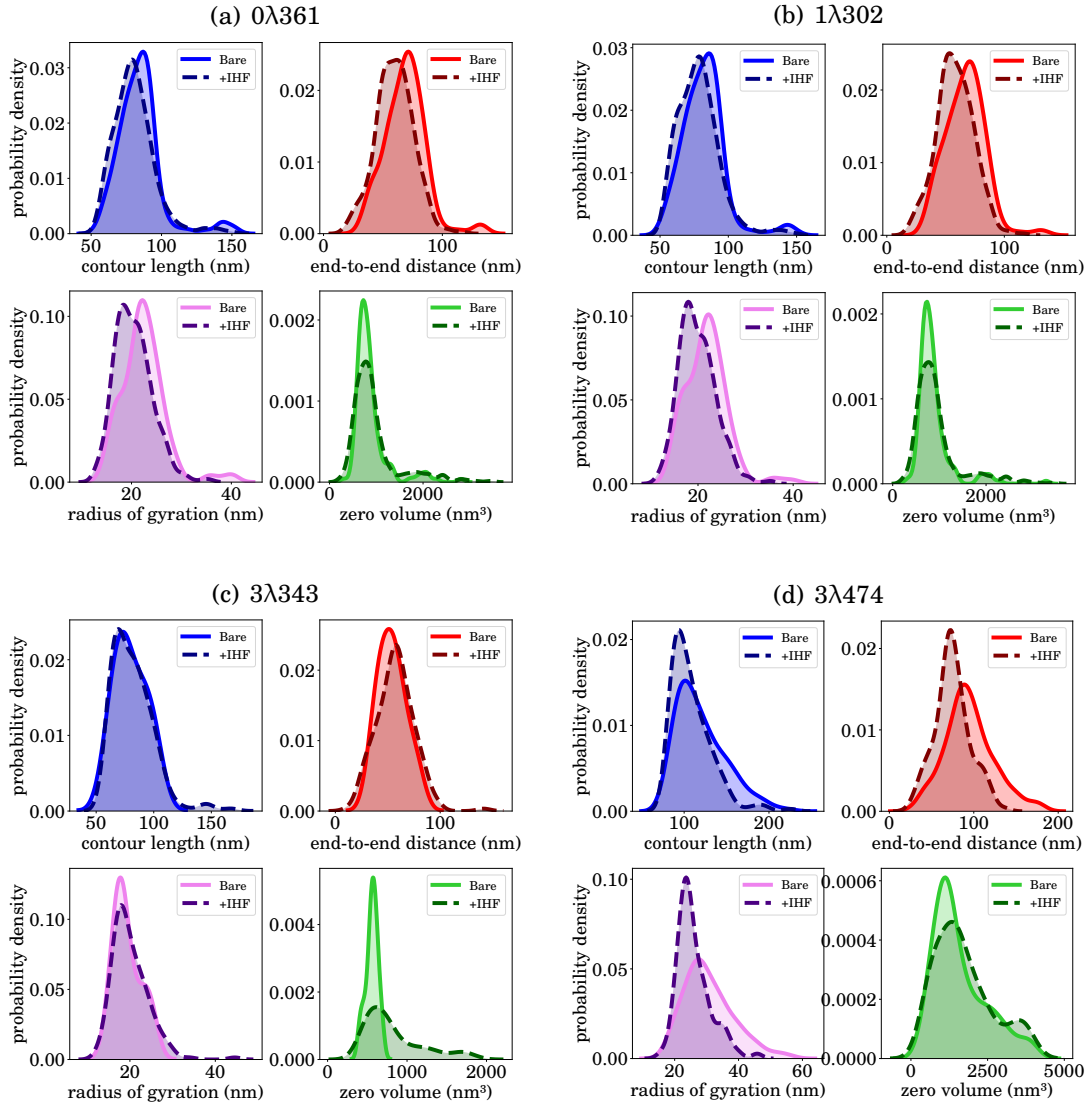
FIGURE 4.4. Segmenting and skeletonising AFM images of the four DNA constructs allows the polymer properties to be determined. Samples with (dashed) and without (solid) IHF show differences between the distributions (a kernel density estimate with bandwidths determined using Scott's method [209]) of end-to-end distance and the radius of gyration. IHF shortens the end-to-end distance and R_g due to the increased bending, while the contour length remains unchanged. Although there is a slight increase in volume both the DNA (302 bp) and protein (~10 kDa) are very small so the volume is hard to distinguish due to the size of the AFM tip.

TABLE 4.4. Polymer properties of DNA constructs for IHF binding. The values shown are given as the median with the interquartile range in brackets. It can be seen that in general the addition of IHF compacts the IHF reducing the length and end-to-end distance. 3λ343 is an exception, most likely due to the low n but was not used for any quantitative analysis.

Sequence	IHF	n	Length (nm)	End-to-End Distance (nm)	Radius of Gyration (nm)	Zero Volume (nm^3)
0λ361	-	98	111 (22)	94 (28)	30 (6)	631 (300)
	+	69	97 (30)	76 (33)	25 (8)	556 (691)
1λ302	-	151	84 (15)	69 (21)	22 (5)	791 (250)
	+	629	79 (18)	60 (21)	20 (5)	811 (365)
3λ343	-	9	78 (19)	51 (15)	18 (2)	551 (65)
	+	205	83 (25)	59 (24)	20 (5)	780 (843)
3λ474	-	232	116 (46)	92 (38)	30 (11)	1452 (1639)
	+	225	105 (34)	74 (27)	25 (7)	2151 (3173)

4.4 IHF has multiple binding modes

As described above, the addition of IHF causes changes to the DNA conformation (Fig. 4.4) but due to the broad distributions of the end-to-end distance and radius of gyration the exact behaviour is difficult to determine from these. Looking at the effect of IHF on individual DNA strands allowed for the clearest determination of the modes of IHF binding. The no-binding-site and single-binding-site constructs (0λ361 and 1λ302 respectively) were analysed as it is unlikely for more than one IHF to be present per DNA strand at low concentrations because the non-specific binding has low affinity and the higher affinity specific binding is only available at one site. By determining the position of IHF on the DNA strand, angles of IHF binding can be measured. This also required DNA that was not too long such that the natural curvature would dominate, hence choosing a construct that is around 2 persistence lengths long. Comparing the behaviour of 1λ302 to that of 0λ361 shows the difference between specific and non-specific binding.

Figure 4.5 shows the 1λ302 construct without IHF and with 1 IHF per 5 base pairs. Even at this concentration the DNA was clearly not saturated with IHF (as seen by others [210]) but protein-bound DNA can sometimes be seen by bright spots in the

(a) Bare DNA

(b) DNA with 1 IHF: 5 bp

(c) Examples of single DNA strands incubated with 1 IHF:5 bp
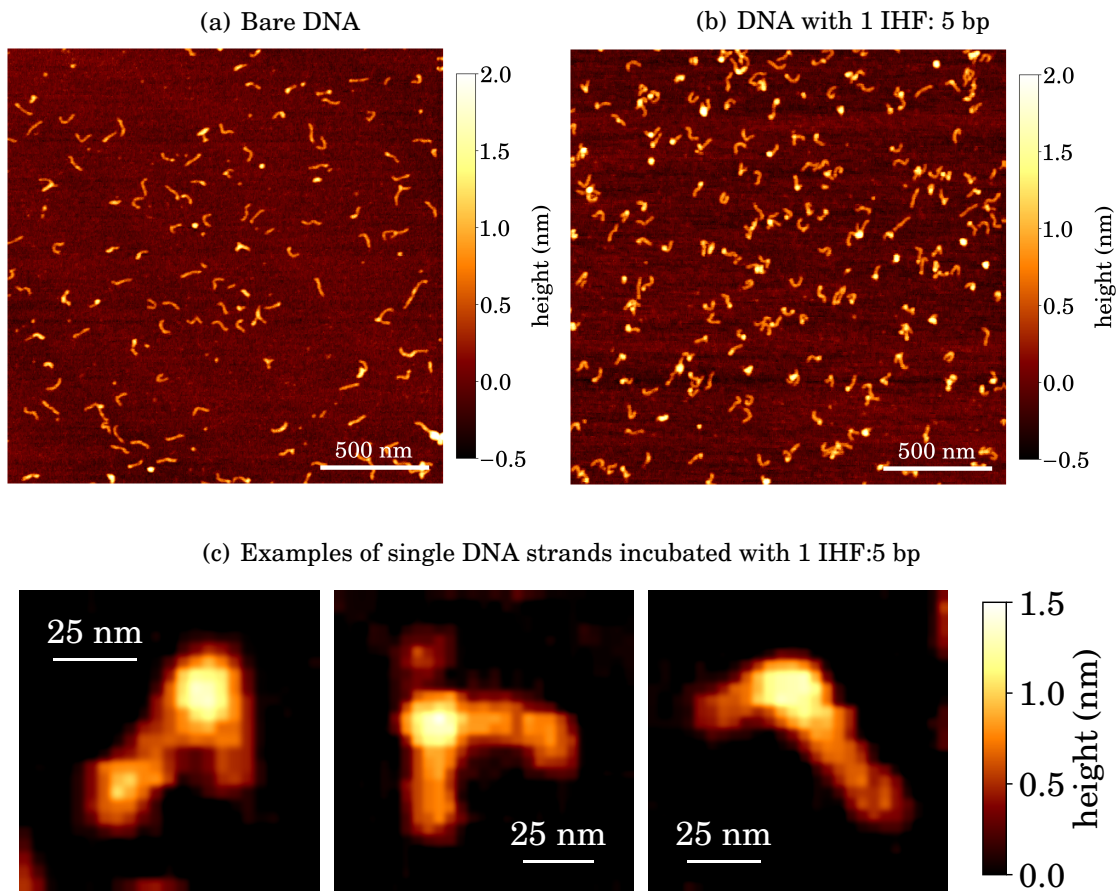
FIGURE 4.5. AFM images of a 302 bp segment of DNA around the *xis* promoter in λ-DNA (1λ302).There is a significant difference in DNA conformation for (a) bare DNA and (b) DNA with IHF. (c) Taking example segments we can see different bending behaviours, where the bright spot is IHF on DNA.

centre of the DNA strand, which are about 1 nm higher, which is roughly the height expected due to IHF ($R_g \sim 2$ nm) (bright spots at the edges are likely due to the poly-L-lysine). As can be seen in the polymer properties in Figure 4.4(b), when IHF binds the contour length and volume remain the same while the end-to-end distance and radius of gyration decrease. This can be compared to 0λ361 (with no binding sites) in Figures 4.9 and 4.4(a), where there also appears to be a difference upon addition of the same ratio of IHF to base pairs. The radius of gyration decreases and IHF can be seen to bind but bending is not immediately as apparent (Fig. 4.9(b)).

Following this, the bending angles needed to be determined to see if IHF binds

in more than one state (differentiated by bending angle) as has been proposed. This is achieved by further processing an AFM image. Starting with the skeletonised DNA contour, the peak in height along this contour (if protein is present as shown in Fig. 4.5(c)) will correspond to the approximate binding region of IHF onto the DNA, allowing the angle to be determined by taking contour vectors either side. Note that the vectors started 3 pixels (~12 nm) away form the peak to account for the size of the IHF in the image and if the contour did not go through the centre of the protein due to skeletonisation. However, this is well within a persistence length (~50 nm) so should not significantly affect calculations of angles.

To determine the angle distribution I first started with the images of $0\lambda361$ and $1\lambda302$ not containing IHF. This was to validate the method and also determine the distribution of bare DNA as this is also present in the images of $1\lambda302$ with IHF. Filtering methods to separate the two populations was attempted but due to the small and comparable height of the DNA and IHF this became too selective. Figures 4.6 and 4.7(a) show a Gaussian distribution of angles, centred around zero, which is characteristic of adsorbed DNA [211].

For both $0\lambda361$ and $1\lambda302$ the addition of IHF leads an increase in larger angles compared to that of bare DNA, consistent with that of IHF causing 'kinks' in the DNA (Figs. 4.6(b) and 4.7(b) respectively). It is also expected that IHF bending will lead to a Gaussian distribution of angles due to the central limit theorem. To determine the number of bending angles, different numbers of Gaussians were fitted and the goodness of fits determined (Fig 4.8). The best fit - when correcting for the number of parameters - is provided by three Gaussians for $0\lambda361$ and four for $1\lambda302$, where one of the Gaussians corresponds to that bare DNA, which has the width fixed from the bare DNA distribution, and two or three IHF-induced bending states. Note that with a specific binding site present this is one higher than the two bending states suggested in the literature, suggesting the existence of an extra state that was missed by FRET measurements.

From the fit of $1\lambda302$ (Fig. 4.7(b), where 29% of the DNA was bound by IHF) we can determine the properties of the three modes of bending, associated with the DNA at 73° (representing ~32% of measured binding), half-wrapped DNA at 108° (representing ~27% of measured binding) and fully wrapped DNA at 147° (representing ~41% of measured binding). The 'associated' DNA is the state that would be missed by FRET as the angle is relatively small compared to the other

two and so may not have generated a FRET signal. This angle distribution can be compared to the one for 0λ361 (Fig. 4.6(b), where 18% of the DNA was bound), which has two angles that match the first two from 1λ302, at 70° for the associated state and 116° for the half-wrapped state (Fig. 4.6). The larger bending angle is not present. This is to be expected as 0λ361 does not contain a consensus sequence and the canonical bending occurs for specific binding further demonstrating the difference between non-specific and specific binding. From these data, two of the three modes appear to be non-specific, and there has been hints of a weakly-bent non-specific binding state [120]. The 108° (half-wrapped) state matches a previous bending angle found for IHF with AFM [210], though this was an indirect measurement and most previous AFM work show a single broad distribution ranging from 80-160° peaked at around 125° [212]. Finally, the 147° bending angle may be a slight underestimate compared to the crystal structure estimate of 160° due to underestimation of large angles by AFM [210] but is the canonical binding 'fully wrapped' mode.

(a) Angle distribution for bare 0λ361

(b) Angle distribution for 0λ361 with IHF
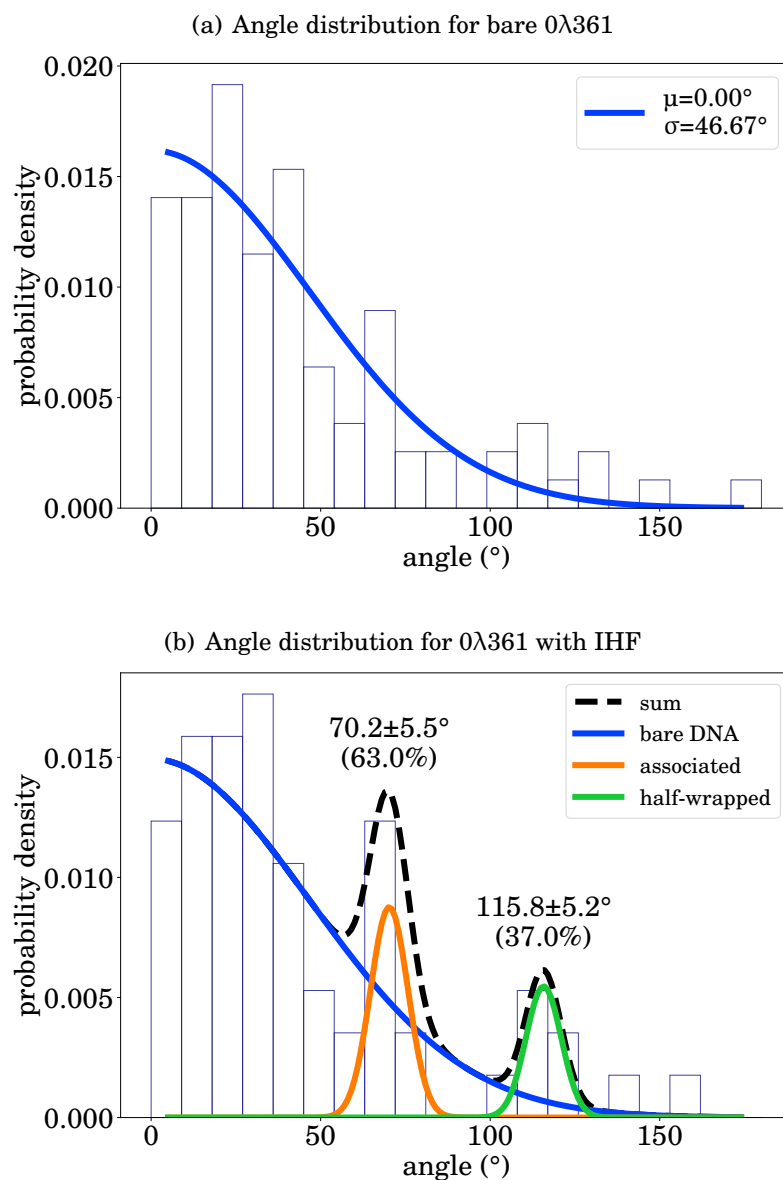
FIGURE 4.6. Distribution of DNA bending angle for 0λ361 with IHF. (a) Bare DNA shows a Gaussian distribution as expected for the worm-like chain, but in the presence of IHF two additional peaks are present at higher angles, corresponding to two bending modes of IHF. As 0λ361 does not contain an IHF consensus sequence these must be due to specific binding. See Figure 4.7 for comparison.

(a) Angle distribution for bare 1λ302

(b) Angle distribution for 1λ302 with IHF
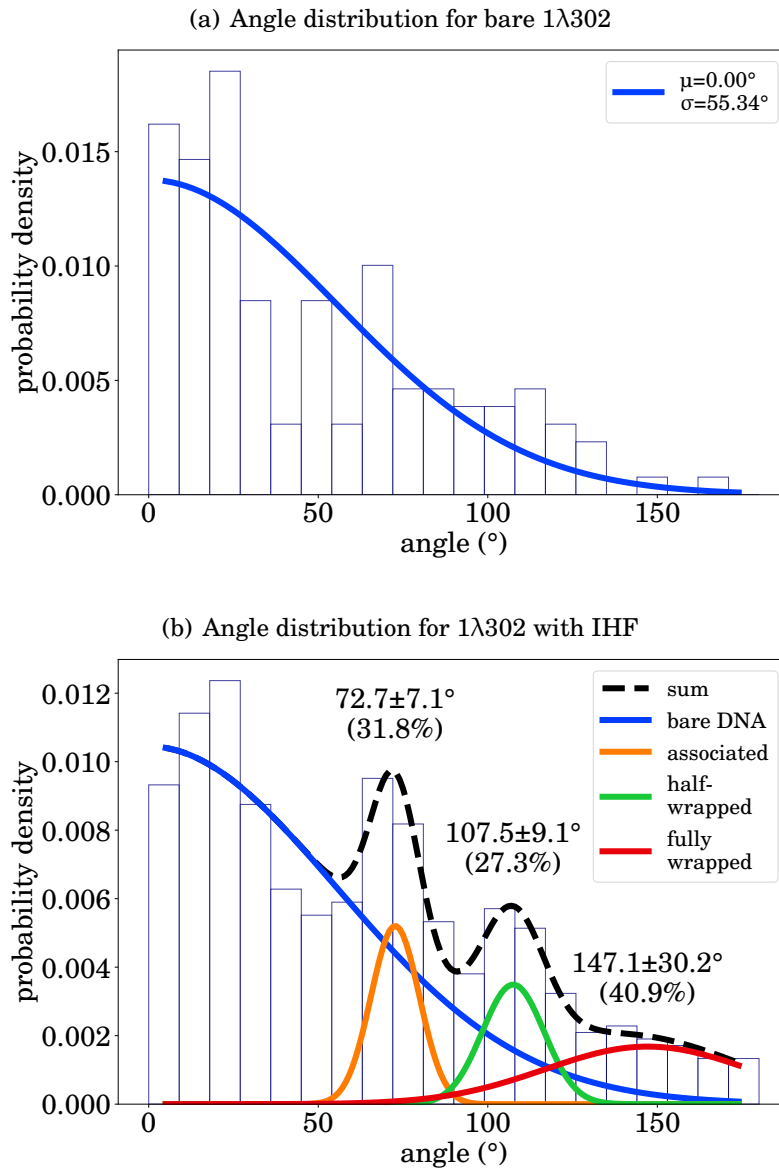
FIGURE 4.7. By finding the bright peak within the central region of the DNA, the position of IHF can be determined (or a random region on bare DNA). This allows the angle of bending (defined as the tangent angle) to be determined. In (a) the blue line is a fitted Gaussian distribution (as predicted from the worm-like chain in 2D), and this fit is also used in (b), scaling appropriately. The remaining three Gaussians in (b) correspond to three sub-states of IHF (where a Gaussian fit was chosen as random noise from a pixelated image dominates). The three peaks are fit at 73±7° (an associated state), 107±10° (a half-wrapped state) and 147±30° (the fully wrapped state as seen in the crystal structure). The percentages indicate the ratio of the three states and the errors quotes are the standard deviation of the Gaussians that were fitted.
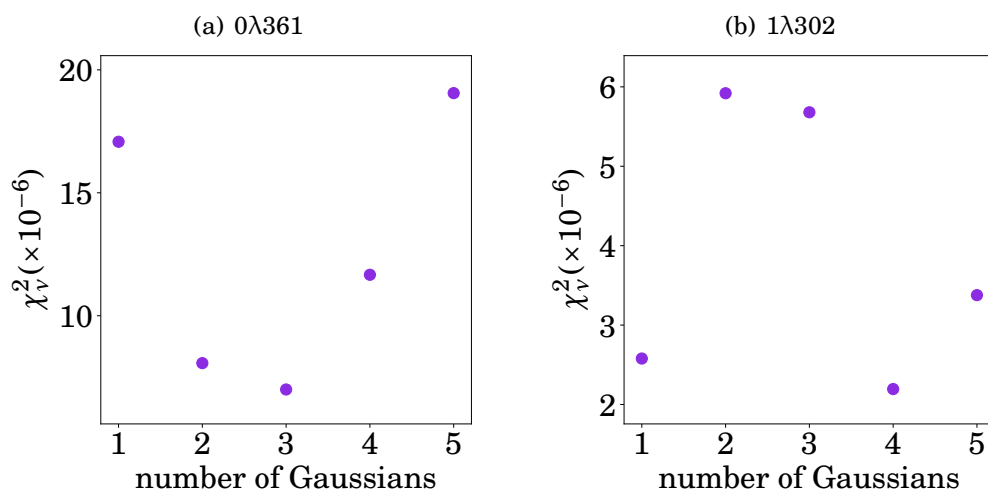
(a) 0λ361

(b) 1λ302

FIGURE 4.8. The reduced χ^2 goodness of fits for an increasing number of Gaussians (i.e. number of binding states) show that the angle distribution of 1λ302 with IHF is optimal at four, but three for 0λ361. Most of both distributions can be explained with a single Gaussian, representing unbound DNA, while the remaining three relate to different binding modes of IHF on DNA leading to multiple IHF-induced bending.

(a) 1 nM bare 0λ361

(b) 1 nM 0λ361 with 1 IHF: 5 bp
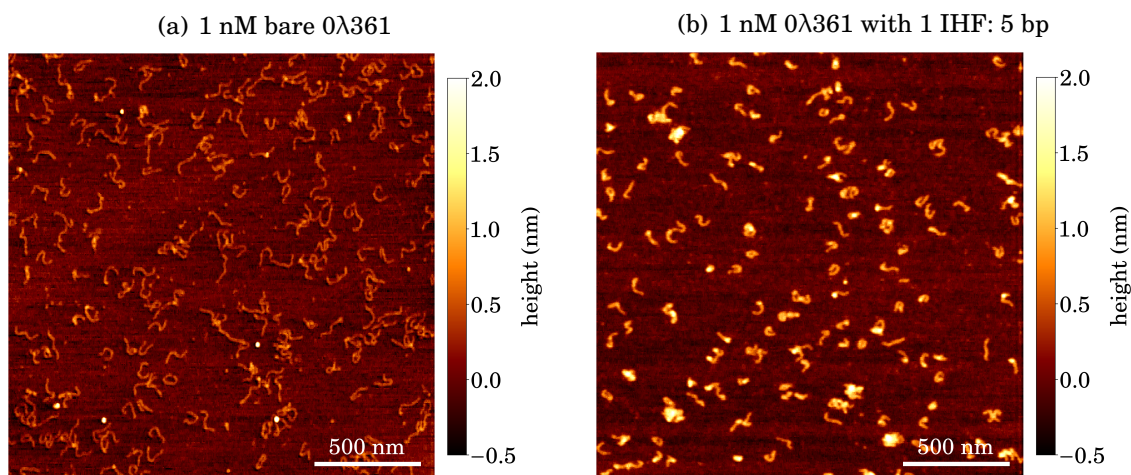
FIGURE 4.9. AFM images of (a) 0λ361 and (b) 0λ361 with IHF. Despite there not being a binding site present, IHF appears to bind non-specifically at this concentration in a similar manner to 1λ302.

75

4.5   Clustering of DNA stimulated by IHF

Lin et al. [120] showed that when the amount of IHF is comparable to the number of base pairs condensation of DNA can be seen. However, these amounts are only biologically relevant in the stationary phase of cell growth, and do not apply to extracellular DNA. They propose that this condensation is due to overcrowding of IHF, preventing the bending of DNA and instead only having one 'arm' of IHF bound, and the other free to bridge to a distal part of DNA. Although the occasional 'cluster' could be seen for both 0λ361 and 1λ302 at 1 IHF:5 bp, when the concentration is increased to over 100 nM IHF to 1-1.5 nM DNA (so ~1 IHF:3 bp) large clusters of DNA was observed in the 1λ302 construct, which increased in size as the ratio of IHF to base pairs increased (Fig. 4.10). It is possible that these clusters, once they begin to form, are preferable to single-site binding as the majority of the non-clustered 1λ302 appears to not be bound by IHF.

The two constructs with three binding sites behave very differently to the constructs with one or no binding sites (Figs 4.11 and 4.12). Even at low concentrations, from around 1 IHF:100 bp (compared to 1 IHF:3 bp for single binding) IHF/DNA clusters could be seen, larger than those for the other two constructs, especially in the case of 3λ343. This could be due to the shorter length (around ¾ of 3λ474) as most of the sequence is the same (including the binding sites), or that it has a much higher AT-content (70% vs 60%). Bright spots also appear where there is possibly more IHF present though this would need to be investigated further. As with 1λ302, there appears to be fewer DNA that are bound with single (or three) IHF.

As clustering occurs even at low concentration the amount of IHF cannot be the sole cause of this increased clustering. The increased number of specific binding sites could allow for IHF to bind with more than one per DNA at low concentration. However, this alone would be more likely to just lead to multiple bends except that the three binding sites are very close together, and likely interact. The tension in the DNA caused by one possibly modulates the binding of the other. In other words, it is harder to fully wrap DNA that already has IHF attached as the DNA becomes less flexible. The multiple partially bound IHF are then able to form bridges with multiple DNA (see Fig. 4.13). This could simulate the overcrowding seen by Lin et al. [120] at more biologically relevant concentrations and allow IHF to bridge DNA. This could explain the role of IHF in extracellular DNA within biofilms as it shows how IHF can be promoted to produce bridges dependent upon DNA sequence.

(a) 1nM 1λ302 with 1 IHF: 5bp

(b) 1nM 1λ302 with 1 IHF: 3 bp

(c) 1nM 1λ302 with 1 IHF: 2 bp

(d) 1nM 1λ302 with 1 IHF: 2 bp
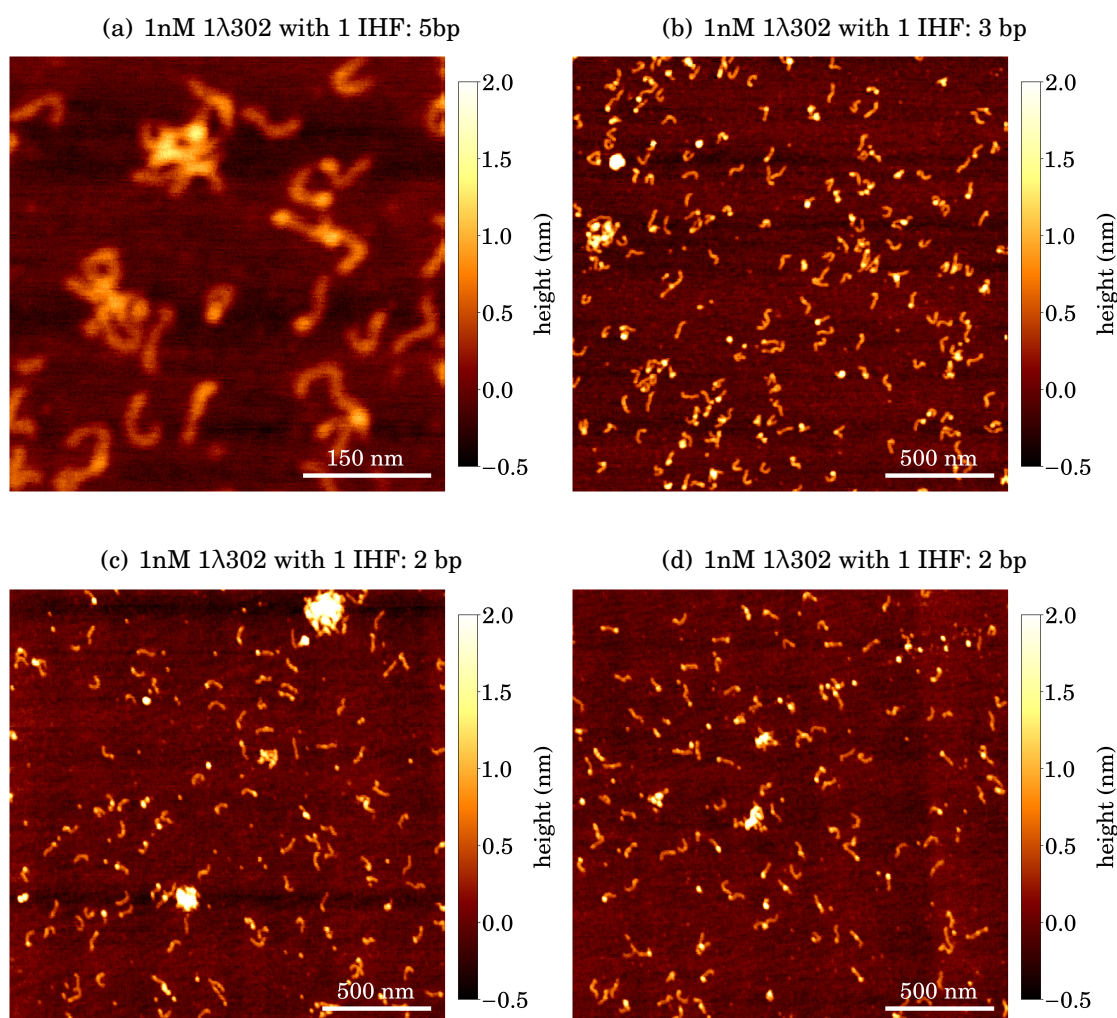
FIGURE 4.10. Examples of clustering of 1λ302 with IHF. For 1 nM of 1λ302 with [IHF] $\gtrsim$ 100 nM small clusters or bridges of DNA strands was observed. These appear to get larger/more common as the concentration was increased to 150 nM.

(a) 1 nM 3λ343 with no IHF

(b) 1 nM 3λ343 with ~ 1 IHF:70 bp

(c) 1 nM 3λ343 with ~1 IHF:17 bp

(d) 1 nM 3λ343 with ~1 IHF:7 bp
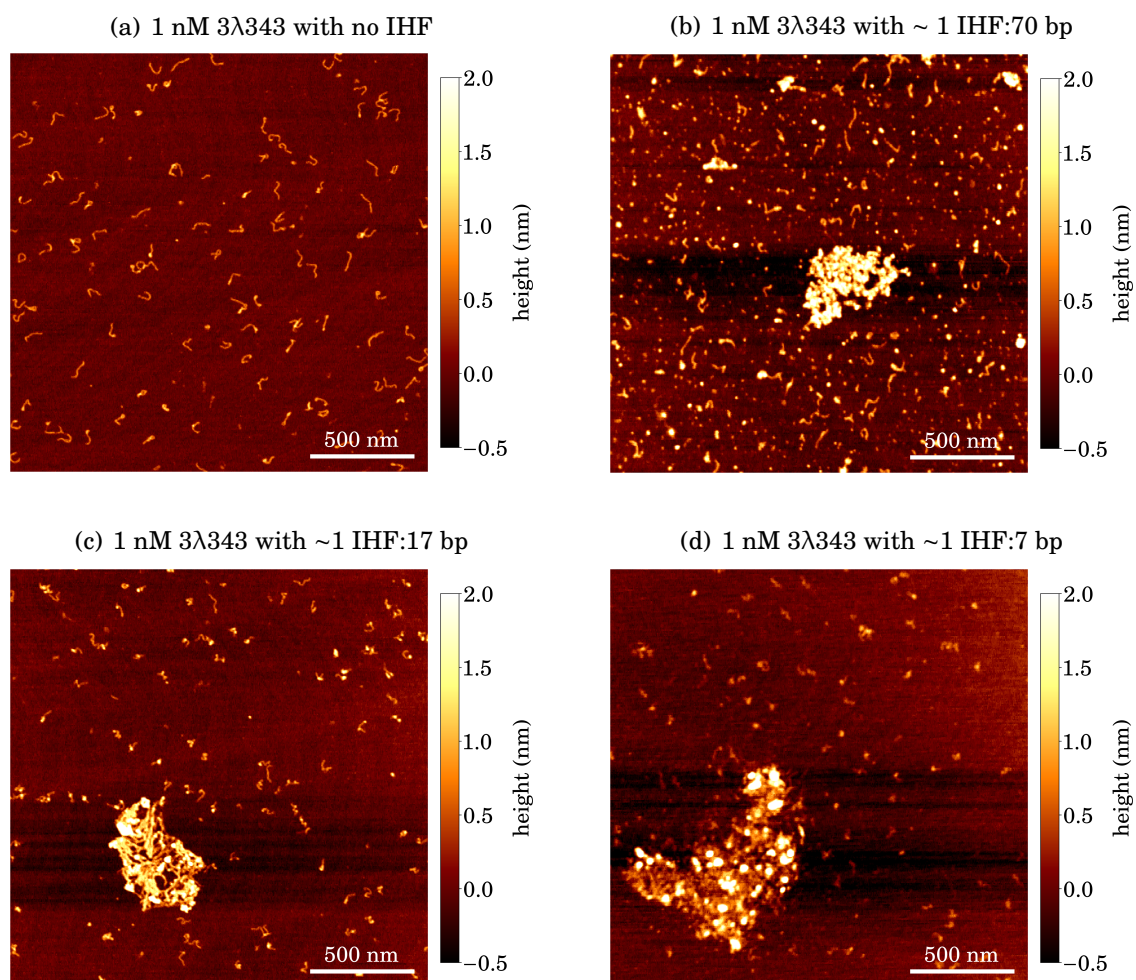
FIGURE 4.11. Examples of clustering of 3λ343 with IHF. Shown are example images of 1 nM of 3λ343 with (a) 0 nM, (b) 5 nM, (c) 20 nM and (d) 50 nM. Even at low concentrations, clustering can be seen and these are significantly larger than for the no or single binding-site constructs. This is possibly due to the three sites being close enough that the IHF cannot fully wrap the DNA and instead bridges to another DNA strand non-specifically

(a) 1 nM 3λ474 with no IHF

(b) 1 nM 3λ474 with ~1 IHF:95 bp

(c) 1 nM 3λ474 with ~1 IHF:24 bp

(d) 1 nM 3λ474 with ~10 IHF:95 bp
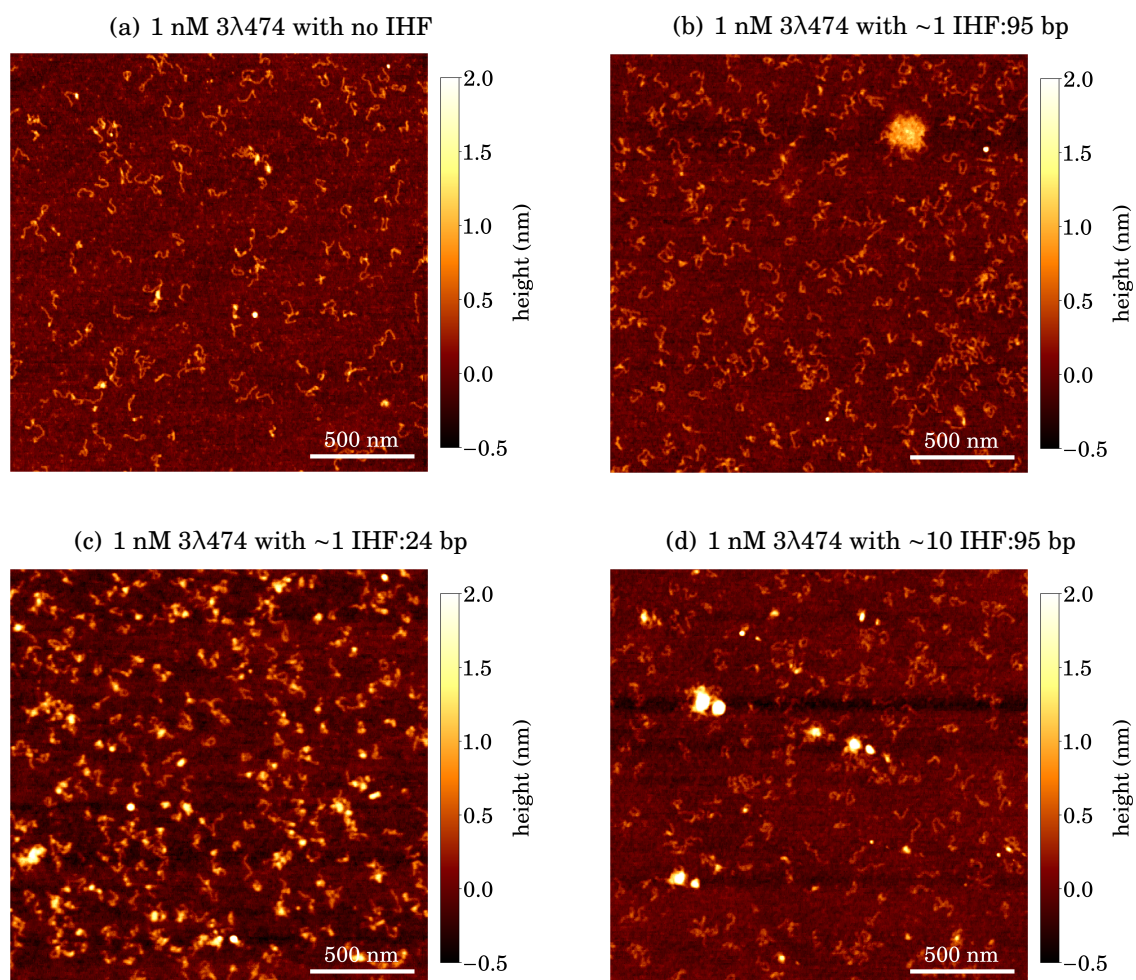
FIGURE 4.12. Examples of clustering of 3λ474 with IHF. Shown are example images of 1 nM of 3λ474 with (a) 0 nM, (b) 5 nM, (c) 20 nM and (d) 50 nM. Even at these concentrations clustering can be seen, though smaller for the similar 3λ343 construct, these re still more significant than for the DNA constructs without three binding sites suggesting that the proximity of these three binding sites modifies the behaviour of IHF to prefer to bridge instead of bend DNA.
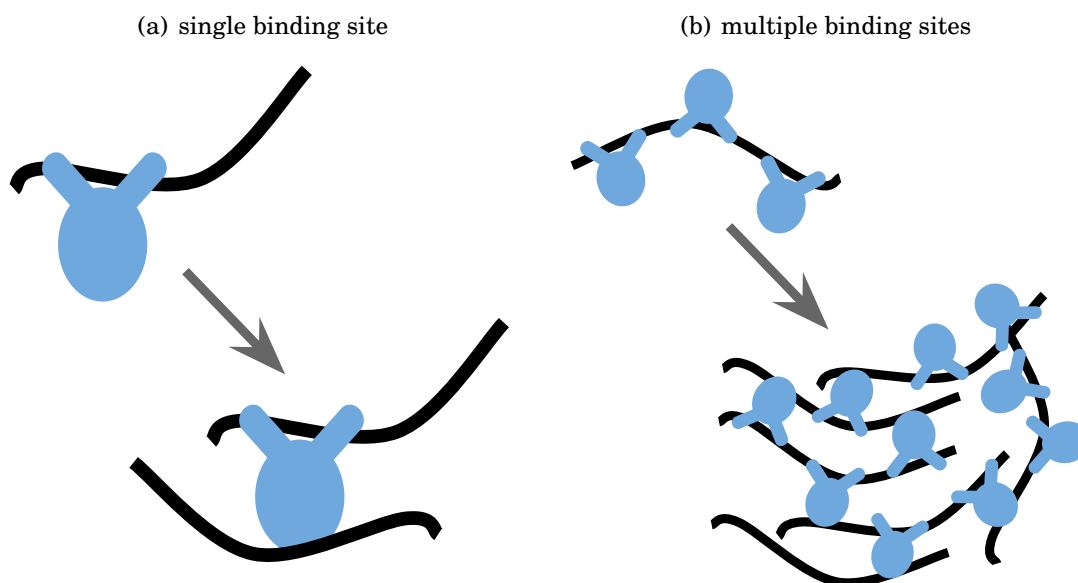
FIGURE 4.13. With a single binding site (a) a single strand of DNA can only be bridged to one other DNA by a single IHF (unless the concentration increases to allow non-specific binding). However, with multiple binding sites (b) each DNA strand can bridge with up to three others, forming larger clusters at lower concentrations.

4.6   Effects of IHF binding on DNA minicircles

Another avenue of investigation with NAPs is to use a DNA "minicircle" instead of a linear strand of DNA. These are short pieces of circular DNA, and so introduce topological constraints similar to those of circular DNA within bacteria - both the genome and plasmids.

The use of minicircles is important as circular DNA involves supercoiling, leading to twist and writhe in the DNA, helping to condense it. Twists in DNA introduce strain but the introduction of kinks by IHF can help to relax this, as it makes DNA more locally flexible. It may also be possible, with increased resolution to see bridging of two regions in a minicircle by IHF, which could imply it plays a role in separating the supercoiled domains of the bacterial nucleoid. Therefore, the study of circular as well as linear DNA is vital in fully understanding the role of IHF in the cell.

Preliminary work on minicircles was carried out by performing AFM. Figure 4.14 shows minicircles that are 336 bp in size (*mc336*) both without IHF (Fig. 4.14(a)) and

with (Fig. 4.14(b)). One issue here is the resolution and the compaction of the minicircles. This is due, in part, to the minicircles being supercoiled. Using liquid AFM may help increase the resolution to observe this [213]. However, differences between the two can still be seen as shown in Figures 4.14(c)-4.14(e). An ellipse was fitted to each of the minicircles (using scikit image [214]) to determine the major and minor axis. The compaction caused by the presence of IHF can be seen in the the major axis decreasing and the minor axis losing a second peak corresponding to open minicircles. The volume distribution for bare DNA has two peaks, where the larger one is expected to be that for open DNA (due to the poor measurement of volume by AFM). This peak disappears when IHF is added, but the original distribution broadens due to the presence of IHF.

Bending angles were also measured, by manually defining the contour vectors for minicircles which had identifiable bright spots, assumed to be IHF (Fig. 4.15(a)). The kernel density estimate is shown in Figure 4.15(b). We see angles that could correspond to the associated and half-wrapped state (although these may not necessarily match due to the DNA being circular). We do not see the fully wrapped state but this is likely due to DNA in this state being completely compacted, preventing the angle from being measured.
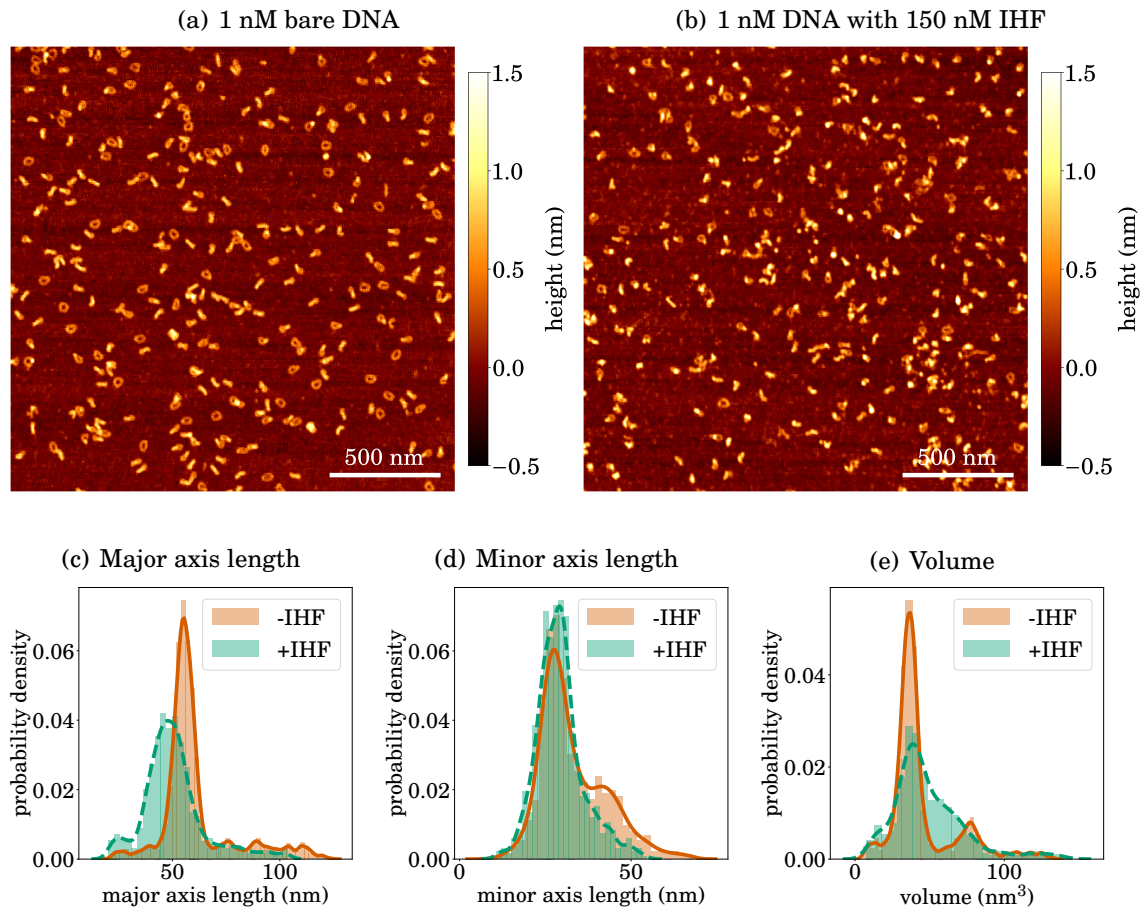
FIGURE 4.14. (a) AFM images of 336 bp minicircles that contain both closed and open conformations due to supercoiling. (b) The addition of IHF causes a large amount of compaction and a reduction in the number of open minicircles. This can be seen in (c) and (d), the distributions of the major and minor axes of an ellipse fitted to the minicircle ($N = 1996$ for bare DNA and $N = 877$ with IHF). The major axis length decreases, suggesting overall compaction. The minor axis length also decreases, losing a peak at around 45 nm (i.e. that of the open minicircle). (e) The zero volume distribution has two peaks without IHF, possibly due to a second larger peak for the open minicircle. With IHF this peak decreases (as there are fewer open minicircles) and the volume appears to broaden due to the addition of IHF.

(a) Example images of minicircles

(b) Bending angle distribution
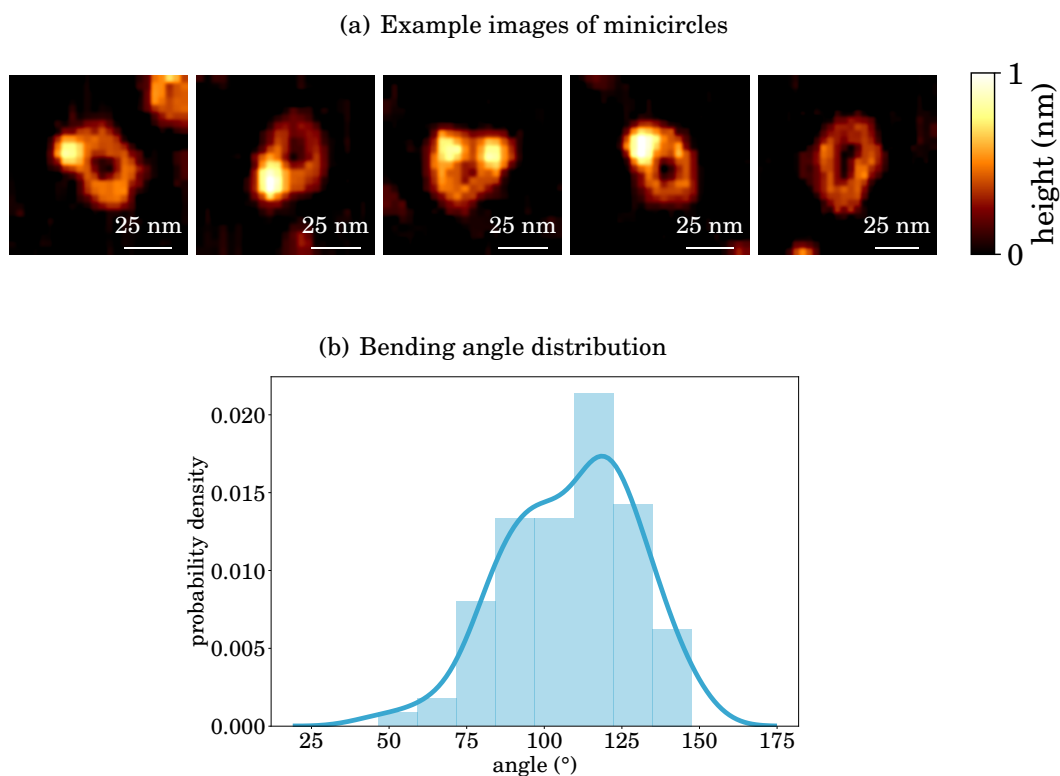
FIGURE 4.15. IHF bending angles on of minicircles (of length 336 bp) ($N = 89$). (a) Examples of the minicircles (zoomed in), where the first four show bright spots corresponding to IHF. (b) Angles were estimated by identifying a peak in the minicircle image and then estimating the angle. Although more work is needed there appear to be two peaks around the angles of the associated and half-wrapped state (which may alter due to torsional constraints). The fully wrapped state was not seen but this is likely due to fully wrapped state being compacted. The fits (solid lines) of the histograms are kernel density estimations with bandwidths determined using Scott's method [209].

4.7 Discussion

Unlike many NAPs, IHF has a consensus sequence that it strongly binds to, creating one of the sharpest DNA bends seen in nature. However, I have shown that there are a variety of bending modes that IHF exhibits, in particular the additional 'associated state', and how this can explain some of the differences between specific and non-specific binding. The difference in bridging behaviour in the three-binding-site constructs suggests a way in which IHF can stabilise extracellular DNA and compact the genome.

4.7.1 Suggested model for IHF binding

IHF has four regions that make contact with DNA, that exist on the 'body' of the protein (see Fig. D.1). There are two roughly on the top half of the IHF (on each side) and another two on the bottom half. In addition, there are prolines at each arm that intercalate with the DNA. From my experimental results and molecular dynamics simulations by G. D. Watson (example images of which can be found in Appendix D), the following model is proposed (see Figure 4.16).

IHF intercalates the DNA via the 'arms' before or simultaneously with binding [215]. The 'associated' state, where the DNA is loosely bound to the IHF is formed by contact at one binding site near the arms, leading to an increase in bending to approximately 73°. Alternatively two points of contact on the same side of the body of IHF, leads to the 'half-wrapped' state with a bending angle of 108°. Finally, the other side of the body can also bind via one of these two partially wrapped states, leading to a fully wrapped DNA segment around the IHF protein causing a bend angle of 147°. Only the associated and half-wrapped state is present in the DNA construct without a consensus sequence, suggesting that these are due to non-specific binding.

Simulations found that bridging occurs by the upper and lower contacts on the body binding to different regions/strands of DNA, possibly due to intercalation occurring first. The bridging behaviour could be caused by overcrowding of IHF, where there are multiple IHF so there is not enough flexibility in the DNA to fully wrap it around the IHF, and so instead the upper half binds while leaving the lower half free to bind to other DNA non-specifically. While this is possible with a large amount of IHF that can then bind non-specifically, multiple binding sites that are close together also allow this to occur. Furthermore the number of binding sites
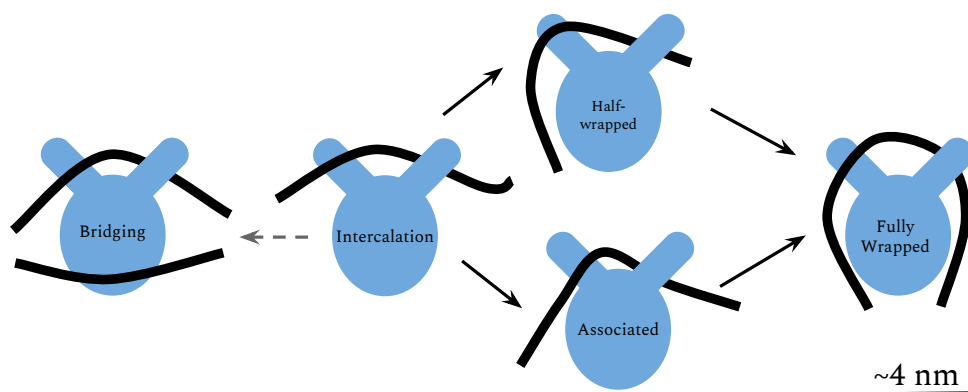
FIGURE 4.16. The possible binding modes of IHF start with the intercalation of DNA between the two 'arms' of IHF. Then either only one of the upper binding regions make contact with DNA stabilising a higher angle of bending (the associated state at ~ 73°) that is uncommon in bare DNA or one side of the IHF now binds causing a large deflection (the half-wrapped state at ~ 108°) that is rarely seen in the bare DNA. IHF can then further wrap either of these states forming the canonical sharp kink around the IHF, leading to the fully wrapped state at ~ 147°. Finally, IHF can also bridge DNA if the lower region cannot bind to the intercalated DNA, possibly due to tension on the DNA. This allows the lower region to bind non-specifically to another region or strand of DNA. The scale bar is to show the approximate size of IHF and molecular dynamics simulations of these (by G. D. Watson) can be seen in Appendix D.

available to the IHF appear to make large clusters preferable. This could be due to being able to form larger networks as each IHF could attach to a different strand of DNA, resulting in up to three other DNA strands attaching (Fig 4.13).

4.7.2 The role of IHF binding multi-modality

IHF, as with many NAPs has many binding modes as it performs a wide variety of functions in the cell. Both bridging and bending was observed, with the bending occuring in at least three modes.

The multiple (semi-)stable binding modes could be to allow flexibility around an IHF-bound complex, allowing the DNA to partially unwind (so that e.g. other proteins in a transcription complex can bind) without the IHF falling off the DNA completely. A transition between IHF binding states has been seen under tension [120], again

shows the role of tension along the DNA in modulating nucleoid-associated protein (NAP) behaviour. The two non-specific binding modes would also allow for IHF to compact DNA when at high concentration as well as allowing IHF to bridge DNA.

The clustering of DNA observed in the presence of IHF lends support to its role in stabilising extracellular DNA in biofilms or organising the nucleoid. Although this has been seen before (and also shown above) at high concentrations, the DNA constructs with three binding sites also show large cluster formation at small concentrations, from as low as five times that of the DNA. Although extracellular DNA is usually tens of kilobases long [216], it has been seen as short at 400 bp [217]. More importantly the selection of what DNA is excreted by the cell, to include regions which are preferentially bound by multiple IHF would provide a basis for formation of an extracellular DNA matrix within a biofilm at realistic IHF concentrations. Wang et al. [121] observed IHF clusters in *E. coli*, and these could be formed by regions that contain many close IHF binding sites, helping to organise the nucleoid.

To better understand the role of IHF in the nucleoid, DNA minicircles are a promising avenue of investigation. Minicircles are likely to form kinks to relieve torsion [218] and IHF could therefore play a role in minicircles in the same manner as the nucleoid, while still allowing for single-molecule measurements such as AFM. The preliminary work shown in Section 4.6 suggests there may be a similar multi-modal behaviour although the angles may shift as the DNA is no longer linear. The data also appear to show that compaction is the primary outcome of IHF binding but higher resolution data may allow for the DNA contour to be more accurately determined allowing for a better determination of bending angles.

Minicircles could be studied further with TPM, but in this case tethered-fluorophore motion may be more appropriate (see Section 3.8.3). As circular DNA coils it has a smaller radius of gyration (so the effect of even a 20 nm bead would be larger). This can be seen in Figure 4.14(a), where the minicircles have a radius of approximately 20 nm. However, TFM does have the advantage of being able to use multiple fluorophores with multi-colour imaging. This would allow FRET to be simultaneously carried out to determine, for example, the distance around an IHF binding site.

BUILDING AN AXIAL OPTICAL TRAP

T o better resolve the behaviour of nucleoid-associated proteins (NAPs) one needs to be able to investigate their behaviour on short strands of DNA because they can bind non-specifically and sometimes make small changes on DNA that are not detectable if the DNA is too long. Therefore, in this chapter I describe my building upon previous work in the field in designing optical tweezers that can apply force - in a well-calibrated manner - in the axial direction. I successfully stretched DNA axially and worked towards building an all-optical/passive force clamp by accurately measuring the optical potential axially, to find the region of constant force.

5.1   Why axial tweezers?

Optical tweezers are a fantastic tool to study the interactions of DNA and polymers but are limited by the length of the DNA tether. Efficient trapping of microspheres require the diameter to be around the wavelength of the trapping laser, which is usually an NIR laser (Nd:YAG, 1064 nm). This sets a lower limit on the length of tether for lateral optical tweezers (Fig. 5.1(a)) before the bead is moved so far down that its motion in the axial direction pulls it out of the trap. For a dumbbell trap the interference of two traps (or an oscillation of a time-shared dumbbell trap) prevent accurate measurement (Fig. 5.1(b)). However, moving the trap in the axial direction
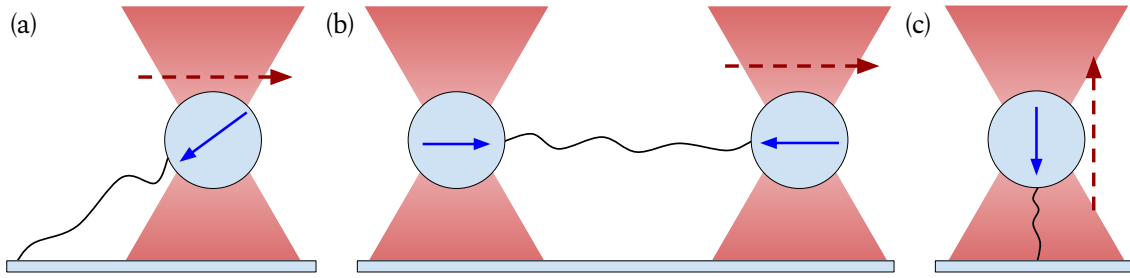
FIGURE 5.1. Three examples of possible trapping geometries with optical tweezers. The dashed arrow shows the movement of the trap and the blue arrow the movement of the trapped microsphere(s). (a) A dumbbell trap uses two beams to hold a tether. This requires a more complicated optical setup but holds a tether in the plane and can be used to achieve base pair resolution more easily than other methods. It also provides a convenient approach to image the tether itself, particularly with fluorescence imaging. However, interference between the two beams sets a lower limit on the tether length. (b) Many optical traps apply force by moving the laser laterally. However, this can cause the bead to be pulled downwards at extreme lengths, and is particularly challenging for short tethers which are comparable to the size of the bead. (c) If instead a single trap moves axially the tether is not held at an angle and so the tether can in theory be arbitrarily short. However, surface effects, a weaker trap in the z direction and more difficult detection can complicate this measurement so it is rarely used.

ensures the motion of the bead is on the same axis as the trap movement (Fig. 5.1(c)) allowing a tether to be much shorter [219].

5.1.1 Surface effects

The axial drift in lateral tweezers is particularly important for short tethers, as the bead must be held near the surface and the trap properties, i.e. the trap stiffness (κ) and QPD sensitivity (β) can change dramatically due to a surface effects, where the drag coefficient, γ, is lowered relative to that expected by Stoke's law, $\gamma_0 = 6\pi\eta r$, where η is the viscosity and r is the bead radius. In the lateral direction the value of γ for different bead heights ($h = r + z$) is shown by Faxén's law,

(5.1)
$$\gamma_\parallel = \frac{\gamma_0}{1 - \frac{9}{16}\left(\frac{r}{h}\right) + \frac{1}{8}\left(\frac{r}{h}\right)^3 - \frac{45}{256}\left(\frac{r}{h}\right)^4 - \frac{1}{16}\left(\frac{r}{h}\right)^5 + \dots},$$
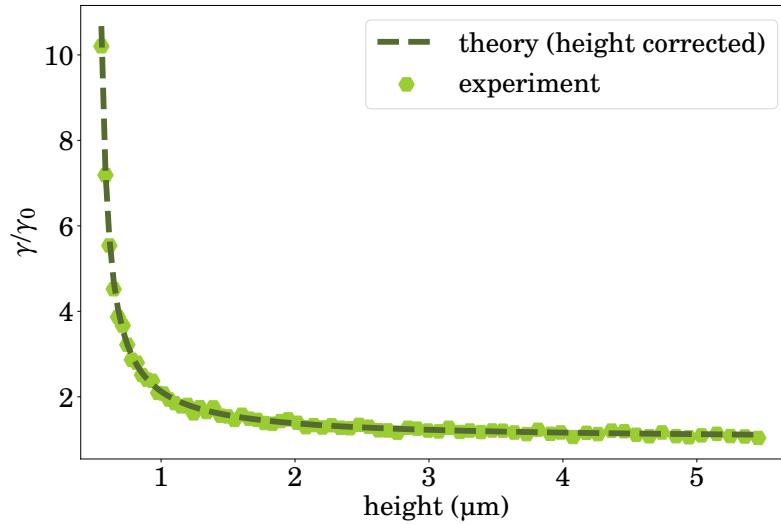
FIGURE 5.2. Drag coefficient (γ) at different heights. Below ~ 2 µm there is a radical difference in the drag coefficient, which causes large changes in the trap properties if the bead height changes. The theoretical data is using Eqn. 5.2 after correcting for the height using Eqn. 5.5.

while in the axial direction it is described by Brenner's infinite sum formula, which can be approximated by [220],

$$(5.2) \qquad \gamma_\perp = \frac{\gamma_0}{1 - \frac{9}{8}\left(\frac{r}{h}\right) + \frac{1}{2}\left(\frac{r}{h}\right)^3 - \frac{57}{100}\left(\frac{r}{h}\right)^4 + \frac{1}{5}\left(\frac{r}{h}\right)^5 + \frac{7}{200}\left(\frac{r}{h}\right)^{11} + \frac{1}{25}\left(\frac{r}{h}\right)^{12}}.$$

Figure 5.2 shows how γ can easily approach ~ $10\gamma_0$ within the first micron above the surface for a bead with a radius of 0.5 µm, which would cause large difference in the measured trap stiffness if not calibrated for correctly.

5.1.2 The need for short strands of DNA

Nucleoid-associated proteins (NAPs) often bind non-specifically or are only weakly specific and so performing experiments on the length scales usually seen in optical tweezers (typically a minimum of approximately 4 kbp/1.4 µm) will result in any small sequence dependence not being seen (see Figure 3.8). There are complications in shortening the tethers in non-axial geometries (Figure 5.1), whether it is inter-ference between multiple lasers for a 'dumbbell' assay or the bead being pulled out of the plane (i.e. axial drift) [219]. For many applications this is not necessary as proteins can perform large changes on DNA structure or are site specific so longer tethers can be used and protein behaviour still isolated. However, as NAPs can be

both non-specific and have small effects on DNA, isolating this behaviour would require a sensitive method that works with short tethers. By applying force along the direction of the DNA extension, very short strands (~500 bp) can be measured, while still maintaining the high spatio-temporal resolution characteristic of optical tweezers. As I previously found that the structure of H-NS/DNA and StpA/DNA filaments were permanently changed after the application of force and repeating these experiments on shorter strands of DNA would allow for sequence dependence to be better investigated. In addition, H-NS with Hha causes slow (~ 30 min) condensation of an H-NS filament along the DNA [44]. However, this was only studied with TPM. A more accurate method, using an optical force clamp, would allow not only for the force of this condensation to be determined, but also to observe if there are any steps in the process (such as a domain forming an extended bridge) or if it is a continuous process.

5.1.3   Optical tweezers *vs* alternatives

Axial optical tweezers are the least common configuration for optical trapping. Although simple geometrically it is only truly advantageous for short tethers and there are simpler alternatives (namely magnetic tweezers). However, none of these alternatives are capable of the high spatio-temporal resolution characteristic of optical tweezers, which is achieved by back-focal plane (BFP) interferometry. The increased resolution and trapping strength [9] are of great importance for short strands. The increased stiffness allows for smaller bead deviations, while the resolution of magnetic tweezers corresponds to around 15 bp and the minimum displacement is 5 nm. There are other methods which can apply force in an *in vitro* assay, such as DNA curtains [221], but these are often optimised for long strands of DNA to allow for (single-molecule) imaging to be carried out at the same time.

5.1.4   Previous work in the field

By increasing axial sensitivity Neumann et al [222] saw oscillations in the measured intensity of an optical trap, which they used to accurately measure the focal shift due to refractive index mismatch (see Sec. 5.2). This was then extended to calculate optical trapping parameters as they change with height [220]. Mack et al. [223] then used these calibrations to build an axial optical trap with accurate measurements of the height of the bead above the surface, and developed an iterative method

to use the parameters to generate force-extension curves. Additionally, Y-F Chen et al. [224] built a passive force clamp [150] in the axial direction. This allowed short DNA (1298 bp) to be stretched as changes in short DNA are too small for accurate active feedback. However, their technique was limited by the use of video cameras for measurements, vastly lowering their sample rate compared to that of a quadrant photodiode (QPD). By accurately calibrating an axial trap with a QPD and measuring the optical potential, this would allow for an accurate passive force clamp to be built.

5.2 Axial optical trapping theory

An axial optical trap differs from a lateral optical trap (Chap. 2.3) in a few key ways, which are avoided in lateral optical traps by keeping the bead at an (approximately constant) height. The biggest complication for stretching in the axial direction is that generating a strong trap requires a high numerical aperture (NA) objective. To get a high NA oil-immersion objectives are usually used but this leads to a refractive index mismatch with the aqueous solutions required for biological assays. This in turn causes the beam profile to change depending upon the height above the surface, in particular it focuses below the expected position in a (usually) non-linear manner (Figure 5.3), which cannot be ignored when changing the stage height. The focal shift changes by

$$(5.3) \qquad \frac{d_{\mathrm{MF}}}{d_{\mathrm{AF}}} = \sqrt{\left| \frac{n_{\mathrm{medium}}^2 - \mathrm{NA}^2}{n_{\mathrm{oil}}^2 - \mathrm{NA}^2} \right|},$$

where d_{MF} is the focal height if the refractive indices of the aqueous medium (n_{medium}) and the immersion oil (n_{oil}) are matched, and d_{AF} is the actual focal position. Therefore, these issues can be reduced by using an aqueous objective (resulting in a weaker trap) or corrections are otherwise made (e.g. by a spatial light modulator) but both lead to weaker traps for the equivalent laser power, so ideally a way of dealing with the complications of oil-immersion objectives is preferable.

An additional complication is that the surface of the slide and the microsphere form two walls leading to a standing wave being generated between them (Fig. 5.4). This leads to oscillations in the laser intensity, which can be measured by the QPD [222]. However, as these are dependent upon the properties of the laser they can be calibrated for and in fact give a more precise measure of how the trap height
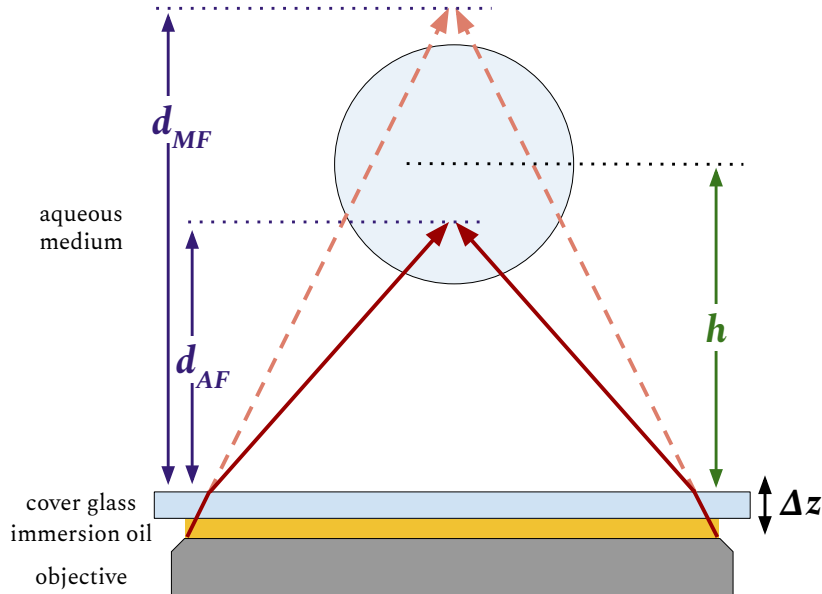
FIGURE 5.3. As high numerical aperture (NA) objectives are a requirement for effective optical trapping oil-immersion objectives (NA~1.4) are preferred. However, this leads to a mismatch due to the aqueous solution required for biological samples. This leads to the actual focus being a lower height (d_{AF}) than would be seen if the refractive indices matched (d_{MF}) and this difference does not scale linearly with the stage position (z) - especially as the trap height (h) is actually above d_{AF} due to radiation pressure.

scales with the position of the piezostage [223]. This then allows the scaling of trap height with stage position to be precisely calibrated, although this does require the loss of some lateral measurement sensitivity.

5.2.1 Empirical method for trap calibration

When a microsphere is trapped by a focused laser a weak standing wave is generated between the bead and the coverslip due to a reflections from the bead (and coverslip). This oscillation is small and so is normally undetectable but reducing the NA of the condenser isolates the intensity along the centre of the bead where the signal is strongest. The following empirical method was determined by Mack et al. [223]. When moving up the optical axis (z), the intensity (at the back-focal plane) can be fit by a third order polynomial.

$$(5.4) \qquad\qquad P(z) = p_0 + p_1 z + p_2 z^2 + p_3 z^3,$$
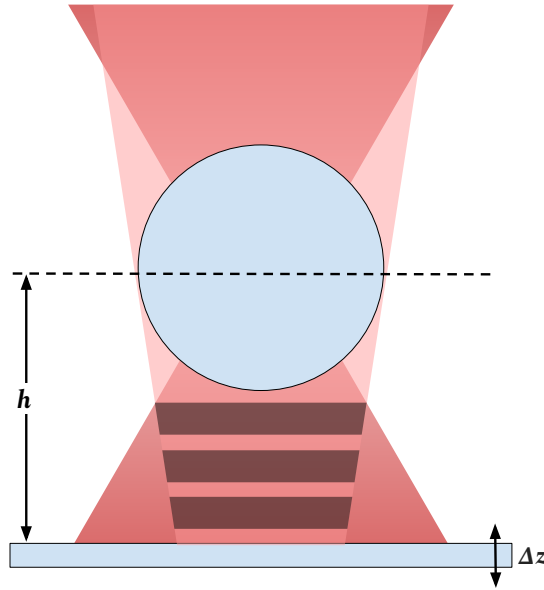
FIGURE 5.4. When the trapping laser passes through the bead some reflects back to the surface, and some of this is again reflected upwards and transmitted/reflected. This generates a standing wave between the bead and the surface that has long been seen. However, Mack et al. [223] used this to calibrate the trap height as the standing wave depends on the distance between the bead and surface (h), and does not vary linearly with stage displacement (Δz).

where z is the stage position (relative to the surface). Due to aberrations the relationship between the distance from the surface to the bottom of the bead, L (where $h = L + r$), and the stage height, z, is non-linear but can be well described by a second order polynomial,

$$(5.5) \qquad L = v_1 z + v_2 z^2.$$

With an equation for the bead height, the oscillations of the intensity which was numerically fitted by [223] as

$$(5.6) \qquad I(z) = P_I(z) + A_I e^{-\lambda_I L} \sin(2kL + \phi_I).$$

We expect the oscillations to get weaker with height ($e^{-\lambda_I L}$), where λ_I^{-1} is the decay length. Otherwise the wave will oscillate as a normal standing wave, with respect to the bead height (and not stage position). Mack et al. [223] showed that the wavenumber,

$$(5.7) \qquad k = \frac{2\pi}{\lambda_{\text{laser}}/n_{\text{water}}},$$

TABLE 5.1. Summary of axial trapping terms.

Variable	Description	Units	Equation
γ	drag coefficient	-	5.2
r	bead radius	μm	
h	height of bead above surface	μm	
z	stage position	μm	
L	length of tether	μm	5.5
I	beam intensity	V	5.6
κ	trap stiffness	pN·μm^{-1}	5.8
β	QPD sensitivity	μm·V^{-1}	5.9
P_x	polynomial fitting non-oscillating curves	function of z or L	
A_x	amplitude of oscillations	function of z or L	
λ_x	inverse of decay length of oscillation	μm^{-1}	
ϕ_x	oscillation phase shift	rad	
k	angular wavenumber of laser (in water)	μm^{-1}	5.7

where $\lambda_{\text{laser}}/n_{\text{water}} = 1064\ \text{nm}/1.33 = 800\ \text{nm}$ is the wavelength of the laser in water.

The oscillations in the beam intensity lead to subsequent oscillations in both the trap stiffness (κ) and the detector sensitivity (β),

$$(5.8) \qquad \kappa(L) = P_\kappa(L) + A_\kappa e^{-\lambda_\kappa L} \sin(kL + \phi_\kappa) \quad \text{and}$$

$$(5.9) \qquad \beta(L) = P_\beta(L) + A_\beta e^{-\lambda_\beta L} \sin(kL + \phi_\beta),$$

where $P_k(L)$ and $P_\beta(L)$ are second order polynomials (as now a function of $L = h - r$. not z). A summary of these terms can be found in Table 5.1.

The above description is strictly only true for an free bead (denoted by the subscript F) as a tether will act to lower the bead axially, shifting L. There are now two ways to approach generating a force-extension curve. One can either use the above equations to determine the force and extension in the free-bead coordinate system or transform to the actual bead position. The latter (as derived by Mack et al. [223]) is advantageous as it allows for real-time manipulations such as force clamping, but is otherwise unnecessary. If we stay in the free-bead/trap-height coordinate system then be bead displacement from the trap centre is determined by the difference between the measured intensity (I) compared to what is expected for a free bead (I_F) for a stage displacement z, corresponding to a free tether length L_F.

$$(5.10) \qquad s = \beta(L_F)[I(z) - I_F(z)],$$
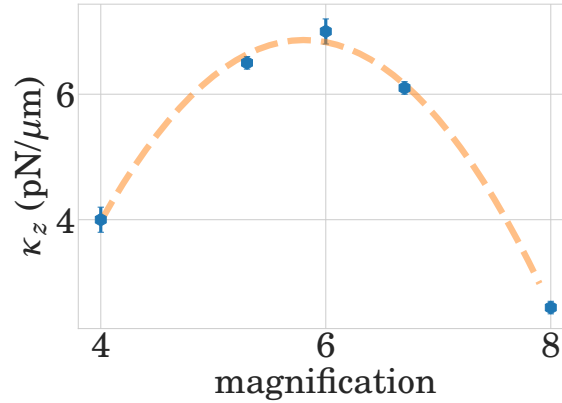
FIGURE 5.5. Changing the magnification of the laser used for the optical
tweezers allowed it to be optimised for better trapping efficiency in the
axial direction. $\sim 6\times$ magnification of the laser was found to be optimal.
The error shown is the standard deviation and the fit is a quadratic.

and so the force at an extension $L = L_F - s$ is therefore,

$$F(L) = \kappa(L) \cdot s = \kappa(L) \cdot \beta(L_F)[I(L_F) - I(L)], \tag{5.11}$$

This is essentially the conventional method of determining force but noting that
both κ and β oscillate and are not constants.

5.3 Optical design

An axial optical trap requires no alteration in optical components to conventional
optical trapping except for a piezostage that is needed for precise (nanometre)
movement in the axial direction. However, to measure the optical potential a second
trap (the "probe" beam) is needed to perturb the first (the "stationary" beam). This
requires a dual beam setup where one of the traps can be moved relative to the other
along the optical axis, while remaining co-aligned in the lateral plane. This was
done by modifying the original setup (Fig. 3.2) as shown in Figure 5.6. After *BS2*
the two beam paths are independently shuttered, one path (the stationary path)
has an AOD to modify the power independently from the other (probe) path. The
probe path has a translatable lens (on a custom-built mount) that allows it to be
moved over ~ 20 mm, corresponding to the focus shifting by ~ 4 µm in the axial
direction. The back-focal plane is imaged onto *L5* (allowing the height for both traps
to be adjusted), which is then additionally imaged onto *M2/M2'*, two piezomirrors

that allow for the two beams to be co-aligned at the trap focus. This leads to two optical paths which can have independently controlled powers, different relative focal heights, and different lateral focal positions. The lenses were selected to give optimal trapping efficiency (as the available laser power is now split between the two paths), and was found to be around $M = 6$ as can be seen in Figure 5.5. This was checked as there are examples of both overfilling and underfilling the back-aperture of the objective to optimise trapping strength.
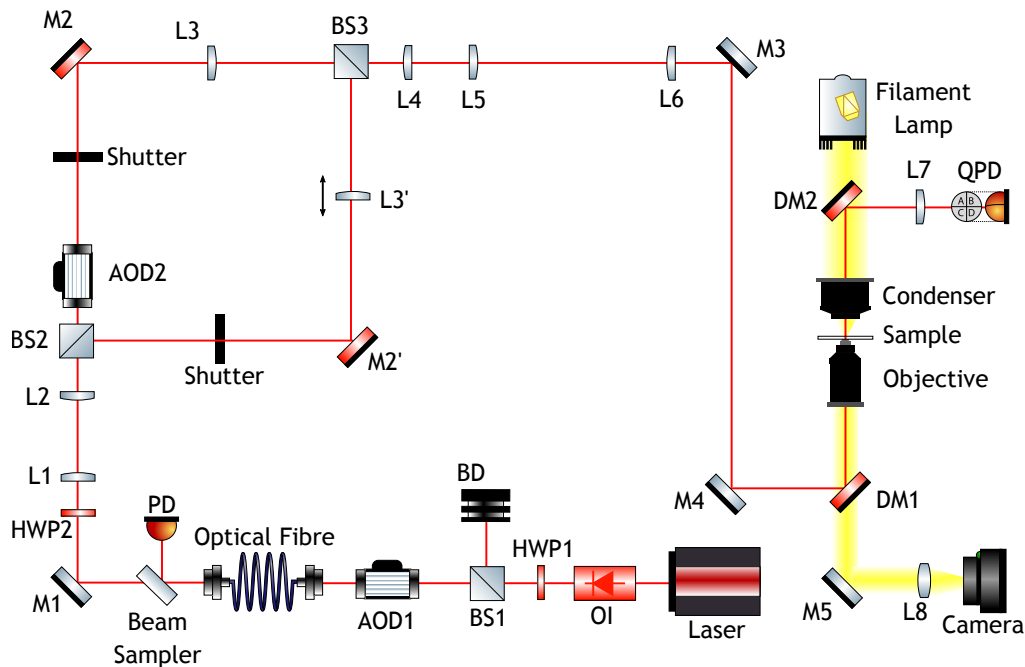
FIGURE 5.6. Optical Setup to measure the axial optical potential. A 1064 nm laser goes through an optical isolator (OI) and the power is varied by using a half-wave plate (HWP1) and a polarising beam-splitter (BS1) to dump unwanted power (BD). The laser then passes through an acousto-optic deflector (AOD1) and an optical fibre to give a single mode. A beam sampler then deflects a small percentage of the beam onto a photodiode (PD). This signal is analysed and AOD1 modulates to keep the power out of the optical fibre constant. The beam then passes through a second half-wave plate (HWP2) which controls the power going to each path for two separate traps after (BS2/BS3) L1/L2 is a telescope and L3/L4 is a 1:1 telescope, where one path (L3' can be moved and the other can have it's power modulated with another AOD. L5/L6 is a final telescope which images the back-focal plane onto L5. M2/M2' are piezo-mirrors to allow the two beams to be accurately co-aligned, while M3 and M4 are steering mirrors to align the trap. The laser then enters the microscope body where a dichroic mirror (DM1) reflects the beam into the sample and another (DM2) projects it onto a quadrant photodiode (QPD).

5.4   Calibrating an axial optical trap

To improve axial detection the numerical aperture of the condenser is significantly reduced to ensure that the axial sensitivity is increased by cutting off-axis rays (at the cost of lateral sensitivity), though the exact numerical aperture depends upon the height of the condenser (i.e. whether it is air or oil etc.). Examples of this can be seen in Figure 5.7. At a low NA - Fig. 5.7(c) - no oscillations can be seen so the bead height cannot be calibrated, whereas at too high an NA generates too much noise - Fig. 5.7(a). However, a well-optimised detection path displays the characteristic oscillations which can be used to precisely calibrate the trap properties with bead height - Fig. 5.7(b).

Once the detection path is optimised, a free bead is trapped and then with a piezostage moved axially down towards the surface (the reverse is possible but can lead to the bead getting stuck to the slide). By analysing the intensity at each height when the axial sensitivity is sufficiently high, the oscillations generated by the standing wave (Fig. 5.4) can be observed and empirically fit to obtain the scaling of the trap height to the piezostage position, using the method described in Sec. 5.2. I used 1 μm beads to optimise trapping efficiency and oscillations can clearly be seen (Fig. 5.8). These were fitted using Equation 5.6. Additionally, the linear region, once the bead hits the surface was also fitted - as both an additional check between calibrations and to more accurately find the surface position (where the two fits coincide).

The calibration confirms that the instrument is sensitive enough for axial trapping, with oscillations in the intensity clearly visible. The decay was also not pronounced within the trapping region we are interested in, suggesting the trap remains sufficiently strong. Additionally, the trap stiffness (κ) and sensitivity (β) both oscillate and are fitted using the oscillation parameters from the intensity as shown in Figure 5.8.
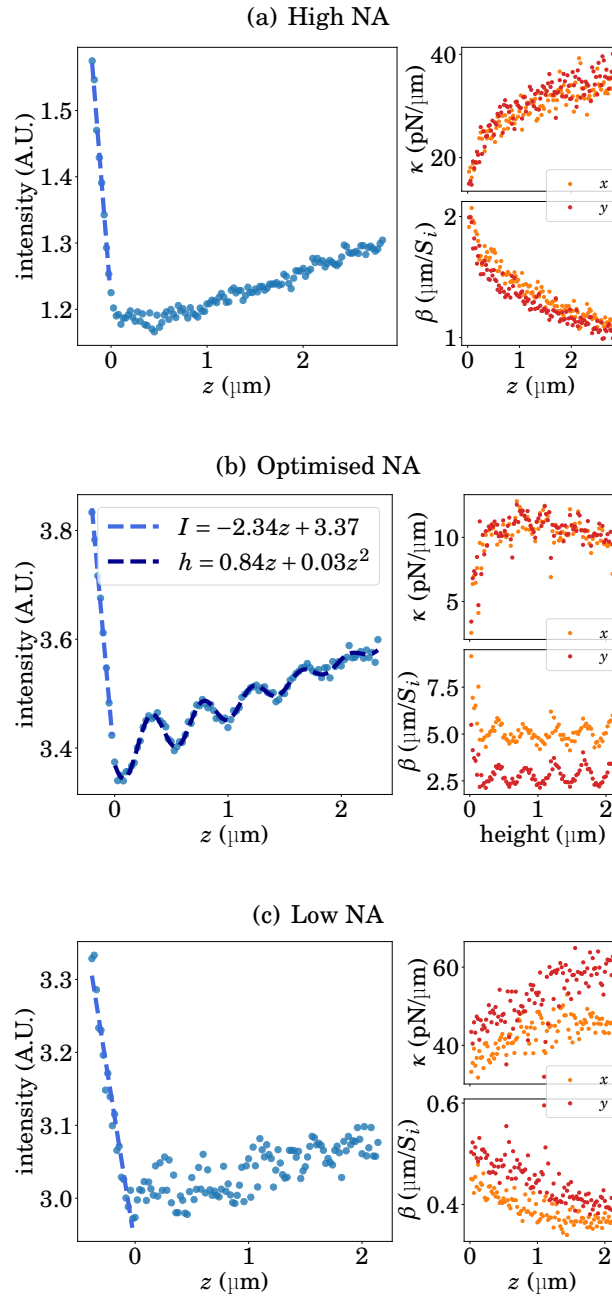
FIGURE 5.7. Optimising axial detection. (a) When the numerical aperture (NA) is high the lateral signal is optimised at the expense of the axial signal. So no oscillations can be seen in the intensity, but the lateral stiffness (κ and sensitivity β are well measured. (b) When the NA is optimised for axial detection, oscillations can now be seen in the intensity and sensitivity, but the lateral stiffness is slighly noisier. (c) Reducing the NA too much makes the signal too noisy, so the oscillations cannot be seen in I or β, and the stiffness is much noisier.
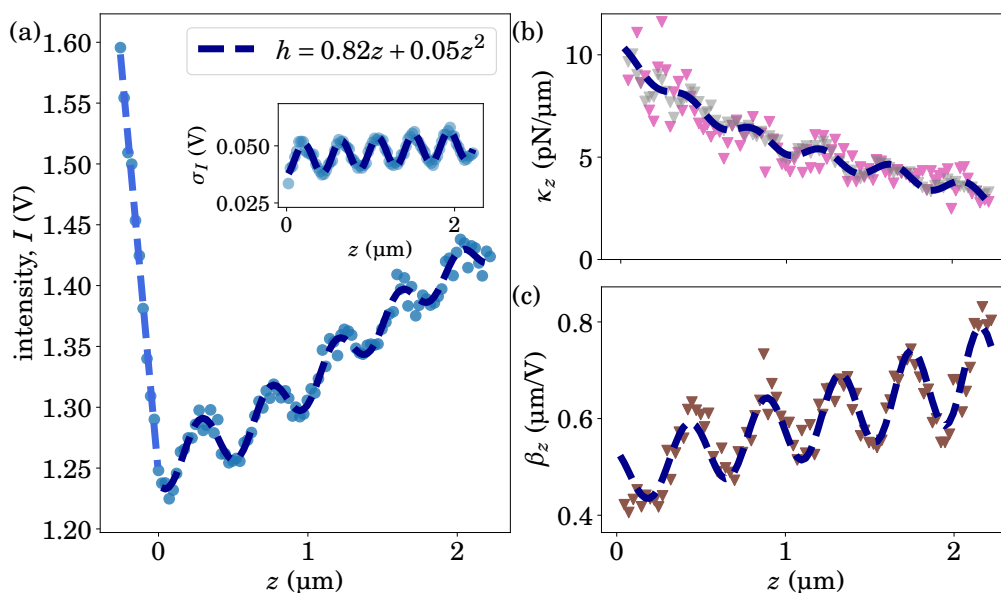
FIGURE 5.8. Example of an axial calibration. (a) The linear region below the surface is due to the beam moving through a fixed bead (akin to how displacement from a centre of a trap is measured). Above the surface, oscillations can be seen due to the standing wave between the bead and the surface of the slide. These are fitted to a decaying sinusoidal to give the scaling of trap height with stage height as shown. This can then be used to correct for the stage height and find the calibrations for the trap stiffness, κ, and sensitivity, β.

5.5 Stretching DNA axially

Now that the position of the bead with stage position is well calibrated the trap can be used to stretch DNA. A 5 kbp region of phage-λ DNA was chosen and functionalised with digoxigenin and biotin using the earlier overlap primers (see Table 2.1).

To stretch the DNA axially the trap must first be centred over the tether point. This is done by repeated stretching either side of the tether point in the x and y directions to find the centre, i.e. where the force is at a minimum. The bead is then moved to the surface and moved upwards (Fig. 5.9, left). Initially, oscillations can still be seen as the tether is slack. This allows the pre-calibrated curve to be overlaid by matching the calibrated curve to the initial 1.5 oscillations. As the bead is moved further away from the surface, the DNA tether begins to exert a measurable force on the bead, pulling it downwards relative to the trap centre. This deviation can be seen as the intensity dips compared to the free-bead behaviour (dashed line).
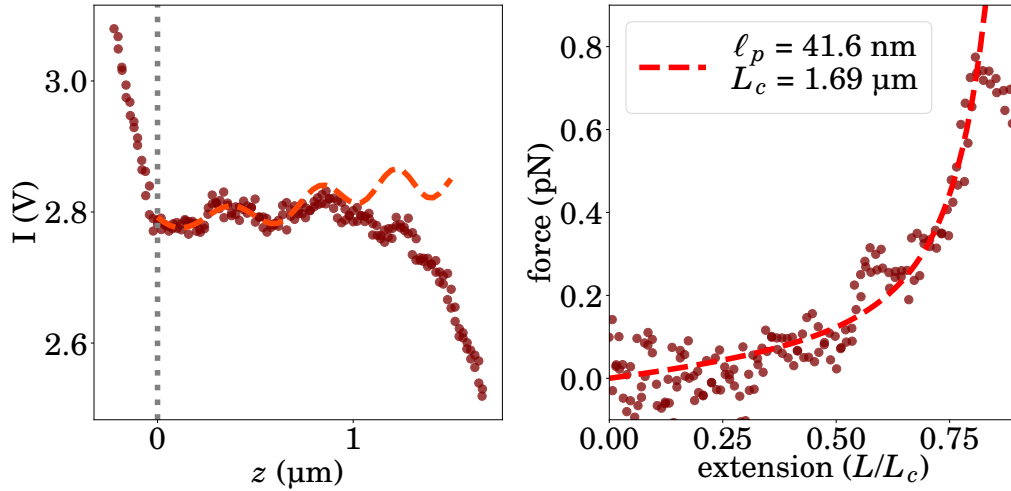
FIGURE 5.9. Example of stretching DNA with an axial trap. A 5 kbp ($L_c = 1.69$ µm) strand of DNA, the bead is relatively unaffected for the first 1 µm. This allows (a) the oscillations to be fit to the original signal (using the parameters from a free bead) to accurately find the surface and measure displacement as deviations from the fit . Then, using the calibrations for stiffness and sensitivity (b) a force-extension curve is produced, that was fitted to a worm-like chain, giving the expected result of $\ell_p = 42 \pm 1$ nm. The turnover past $0.8L_c$ is thought to be due to bead falling out the trap.

This difference in intensity is then converted to a displacement using Equation 5.9 (i.e. taking into account the stage position), and also force using Equation 5.8. As can be seen the persistence length was measured to be 41.6 ± 1.1 nm, which is in the expected range of the worm-like chain (47.5 nm when corrected to l_p^∞ using Eqn. 1.9). This shows that the instrument is capable of stretching DNA axially, and the optimised axial detection can be used to measure the optical potential along the axial direction.

5.6 Accurately measuring the axial optical potential

One of the greatest advantages of the simpler geometry afforded by axial optical trapping is that it allows for force to be applied to (in theory) arbitrarily short strands of DNA (or other polymers), whilst maintaining the high spatio-temporal resolution of optical tweezers compared to similar techniques.

Although the method described above is capable of stretching DNA axially, and a force-clamp with active feedback could be built, there is an issue that, with shorter DNA the changes are so small that is hard to maintain active feedback within the timescale of a biological process, without overshooting etc. (i.e. a change of 5 nm for a 100 nm tether is a lot more significant that for a 1500 nm tether). However, Greenleaf et al. [150] showed that it was possible to create a passive ("all-optical") force-clamp by trapping in the linear region of the optical potential (Sec. 2.3). Here, the force is approximately constant within a narrow region (~200 nm). In the axial direction however, the trap is a lot weaker and wider, so the force is approximately constant within a larger range, albeit weaker, as shown by Chen et al. [224] who built an axial passive force-clamp, though this was limited to camera tracking. As I built an instrument that was capable of precise axial detection with a QPD I aim to combine the two approaches to obtain the axial optical potential more accurately, allowing for an improved all-optical axial force clamp in the future.

5.6.1 Experimental method

To measure the optical potential of a trap, the optical force it applies must be measured. One way of doing this is to build a second trap, which will hold a bead. The original "stationary" trap (which must be weaker) will then apply a small force on the other "probe" trap which can then be measured (ensuring the QPD only measured the signal of the probe trap by blocking the polarisation of the stationary trap). This probe trap must be able to be moved axially, to be able to measure the applied force at different heights (see Figure 5.10). The required setup I built is described in Section 5.3. The key issue here is to co-align the two traps, and maintain this co-alignment throughout the motion of the lens. Additionally, the movement of the lens changes the properties of the probe trap, and the lens must be selected to minimise this. A compromise here was made between the sensitivity of the translation stage and not wanting too long a beam path to fit an optical table ($f = 100$ mm was the final focal length).

The first step is to calibrate the probe trap. Firstly, this requires a scaling of micrometer stage position to change in focal height (achieved by simply moving the micrometer various amounts and moving the bead down to the surface each time, looking for the change). This is a linear scaling. However, this was further improved by matching the height to stage position values for the piezostage to the translation
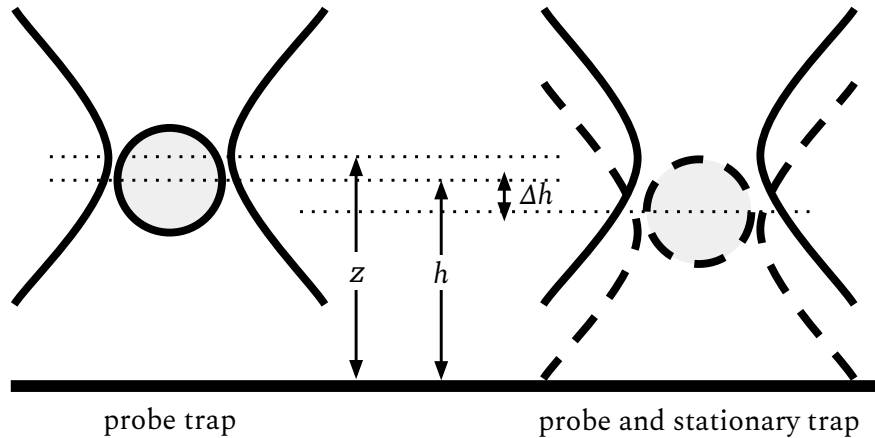
FIGURE 5.10. Schematic of measuring axial optical potential. At each height the probe trap is first calibrated. Then the stationary trap is switched on and the change in bead position, Δh, is related to the force applied by the stationary trap, as $F = k(h) \cdot \Delta h$. By moving the probe trap across the stationary trap the force profile can be measured and the optical potential calculated.

stage. At each position the trap stiffness and QPD sensitivity must also be measured (using the power spectrum method). This is important not only due to surface effects but also due to the changing beam profile due to the translation of the lens.

Once the probe trap is calibrated, the stationary trap can now have its potential mapped. This is achieved by trapping a (1 µm) bead, then finding the surface (looking for the characteristic linear rise in the intensity signal) and then moving 1-2 µm above the surface. Next, a custom LabVIEW interface (App. C.1) automatically moves the translation stage (i.e. lowering the probe trap) and the signal is measured with the fixed trap off (i.e. the unperturbed system) and then with the fixed trap on (i.e. measuring the force it applies on the probe) as shown in Figure 5.10. This is repeated until the surface is reached. This results in two intensity profiles, allowing the effect of the fixed trap to be determined, and it was determined by scanning without any bead that the signal from the two traps do not interfere.

5.6.2 Result

The largest complication in measuring the optical potential in this way was the limited range of travel with the translation stage drifting causing the two traps to drift relative to one another for larger distances away from the midpoint. Addition-
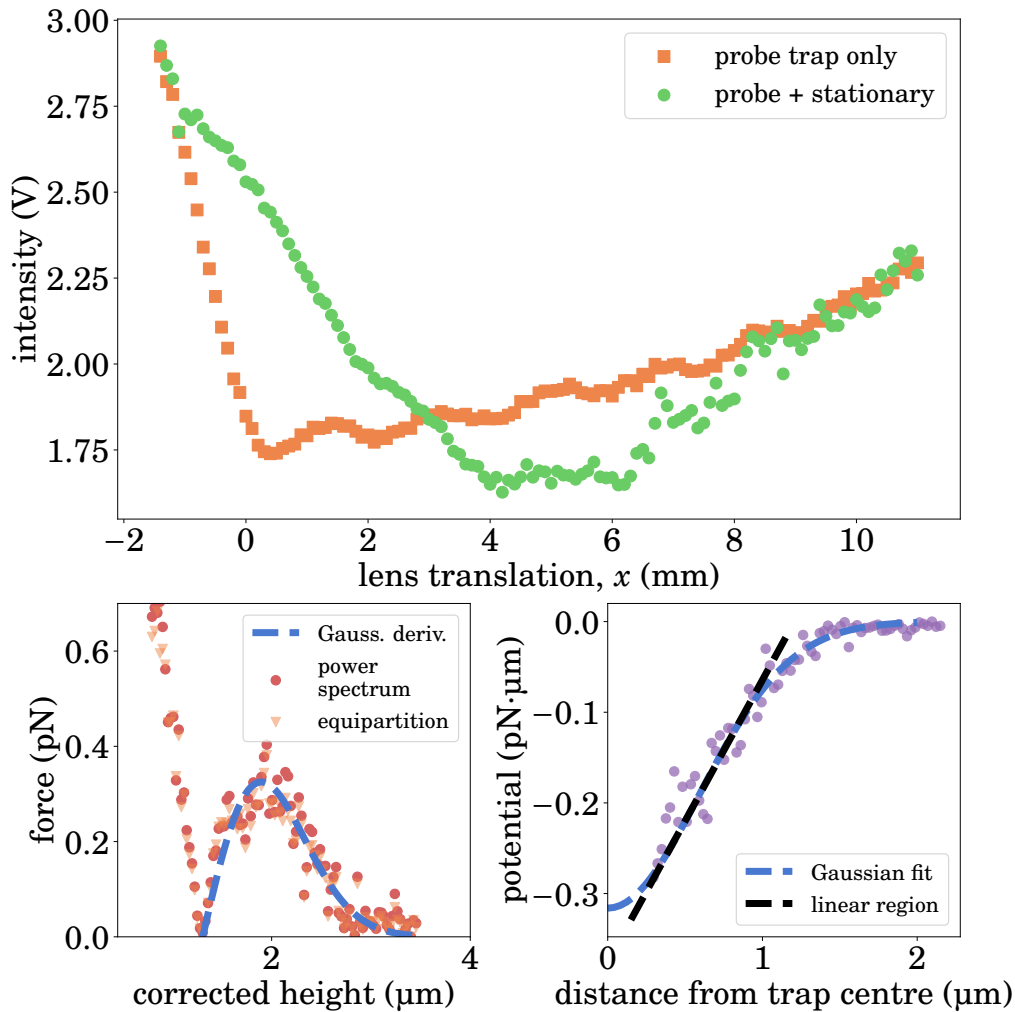
FIGURE 5.11. Measuring the axial optical potential above the trap centre. The axial potential here is measured above the optical trap modifying the method as described by Chen et al. [224]. A strong trap holds a bead which is moved axially by translating a lens. Meanwhile a weaker (fixed) trap is switched on and off allowing the deviation to be measured at each height. The change in height can be converted to a force of the fixed trap. Below the trap surface effects dominate the signal The linear region of the trap can be seen around the trap centre (~0.8 µm). Further above the trap the turnover of the force can be seen, until the two traps are significantly distant such that they no longer interact (~2 µm away from the trap centre). By integrating this force the Gaussian potential can be recovered. The Hookean region can be seen within the first 300 nm and from 300-800 nm a linear region of potential (i.e. constant force) can be seen.

ally, balancing the powers of the two traps was challenging, as there was limited power after the optical fibre (~180 mW) to be shared between them, so there was a compromise between having a stationary trap that was strong enough to cause measurable deviations from the probe trap, while not using so much power that the bead moves between the traps or that the probe trap cannot be well calibrated. When the two traps were well co-aligned the lateral force applied was as low as 8 fN (compared to axial force of over a piconewton).

Initially, the range of travel of the translation stage while maintaining a trap for the probe path was not sufficient to image both above and below the trap centre. This was, in part, due to the extended range of the axial trap, where the potential is non-zero over several microns. This required choosing where to place the stationary trap relative to the surface, to allow the potential to be measured. Figure 5.11 shows the trap placed approximately 1.5 µm above the surface, with the stationary trap at 28 mW and the probe trap at 100 mW. In this case the probe trap applied a relatively small force (on the order of 100s of femtonewtons). Although the Hookean region can clearly be seen on both sides, the full profile can only be seen above the trap.

To move further from the surface and image both sides of the optical potential, the translation stage was extended allowing for a greater range of motion. As can be seen in Figure 5.12 the potential has a width of approximately 2 µm as before, and the force and potential can clearly be seen above the trap centre. Below the trap centre it is still difficult to measure. However, there is a small region that does follow the same ze^{-z^2} behaviour, albeit far from symmetric. The optical potential is weaker above a trap centre, so it could be this imbalance in the probe trap causing the differences. However, it is also possible that the addition of the two scattering forces increase the force above the trap. Chen et al [224] only measured the axial potential below the trap centre and stretched DNA with a calibration similar to the method above. Therefore, it is possible that the scattering force causes the stronger and wider potential above the trap centre (cf. Fig. 2.3 and Fig. 5.12).

As the two sides are so mismatched, and the forces below the trap weaker, I also measured this separately. By moving the trap significantly higher, to the edge of the range of the translation stage, ~3.5 µm above the surface, the lower half of the optical potential could be isolated (Figure 5.13). This appeared to show a wider potential (possibly due to a change in height), though the behaviour was otherwise the same. It is possible that surface effects, in particular increased drag
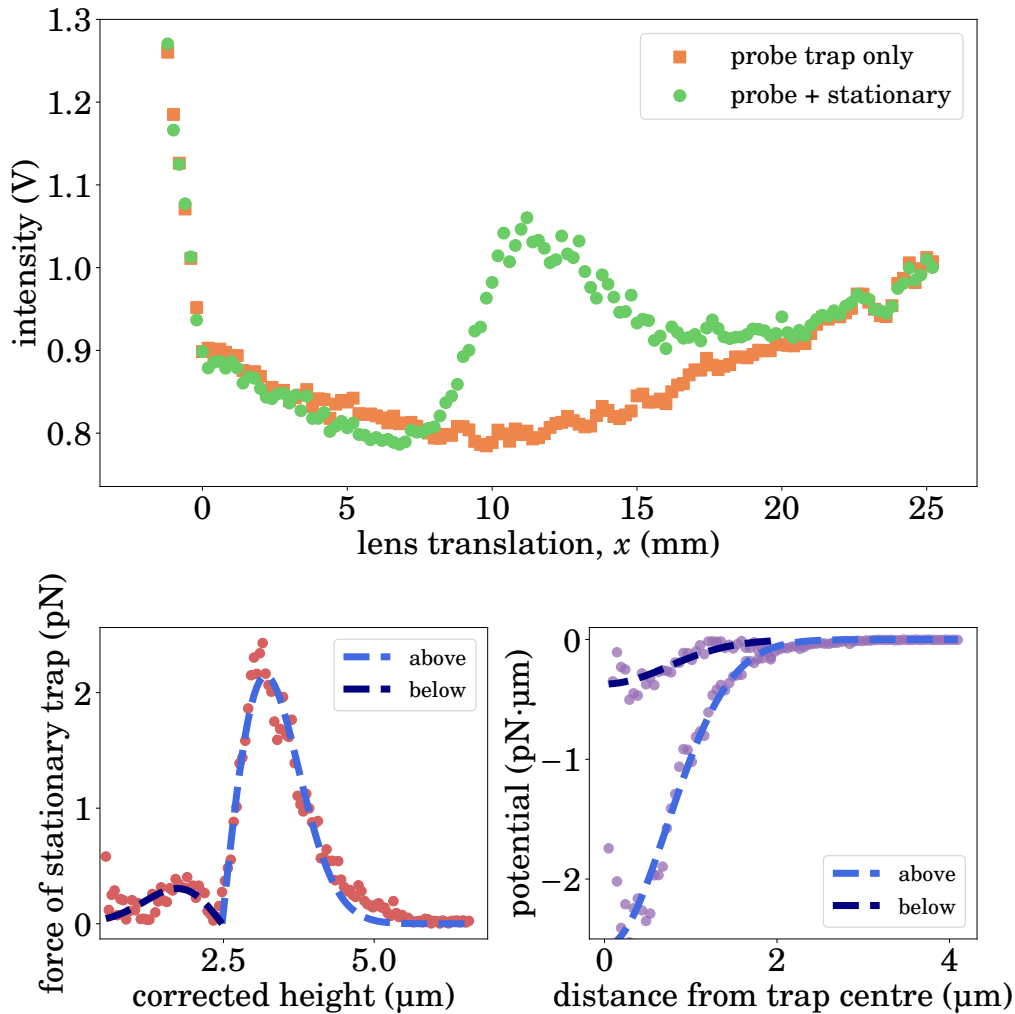
FIGURE 5.12. Measuring the axial optical potential. A bead is trapped and moved down to the surface and then a micron above. The translation stage is then moved in 0.5 mm steps downwards. At each step the trapping path is closed (orange squares) and then opened (green circles). This allows for the displacement of the bead from the probe trap to be measured and the surface to be fitted to the blue curve. This is then converted to a displacement-height relationship by using a calculated $\beta(z)$ and a calibrated fit of Δx (translation stage) to Δh (piezostage). This displacement is then converted to a force using $\kappa(z)$ and the height corrected (by subtracting the displacement) and fitted to the derivative of a Gaussian potential (bottom left). Finally, this is confirmed by integrating to get the potential (bottom right), and the linear region can be seen ~0.5 μm. Note that there is increased noise near the trap centre due to the experimental data being divided by very small numbers.

near the surface interfered with measurements below 1 µm, which would explain the behaviour below this height, i.e. a small error in the height above the surface. However, a linear region can clearly be seen ~ $1.5 - 2.5$ µm above the surface, in a similar manner to before.

Finally, the change in trap behaviour at different powers was investigated by looking at the force-height profiles of a single beam scanned at different laser powers (for the stationary trap). Doubling the power from 25 mW to 50 mW increased the trap strength in the linear region from ~10 pN to around ~12.5 pN (see the highlighted region in Figure 5.14). More importantly, the force-profile did not change except in height (note that the large rise near the surface for the 50 mW beam is due to hitting the surface earlier through drift as each measurement takes 30 minutes, although the two traps will drift together). The constant force region remains in the same region, demonstrating how the force in this region can be altered by changing the laser power.
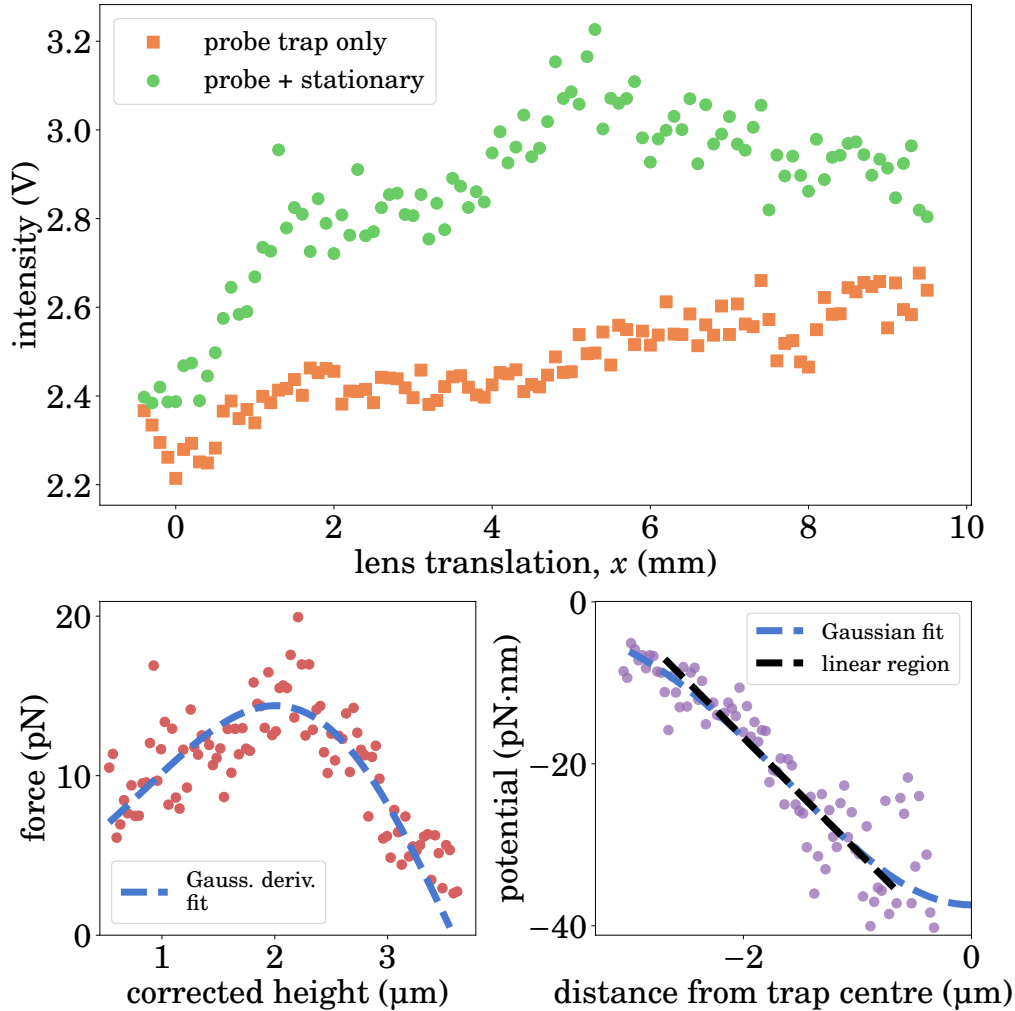
FIGURE 5.13. Measuring the axial optical potential below the trap centre. A bead is trapped and moved down to the surface and then a micron above. The translation stage is then moved in 0.5 mm steps downwards. At each step the trapping path is closed (orange squares) and then opened (green circles). This allows for the the force to be measured as described in Figure 5.12 and fitted to the derivative of a Gaussian potential (bottom left). Finally, this is confirmed by integrating to get the potential (bottom right), and the linear region can be seen ~0.5 µm away from the trap centre. Note that there is increased noise near the trap centre due to the experimental data being divided by very small numbers.
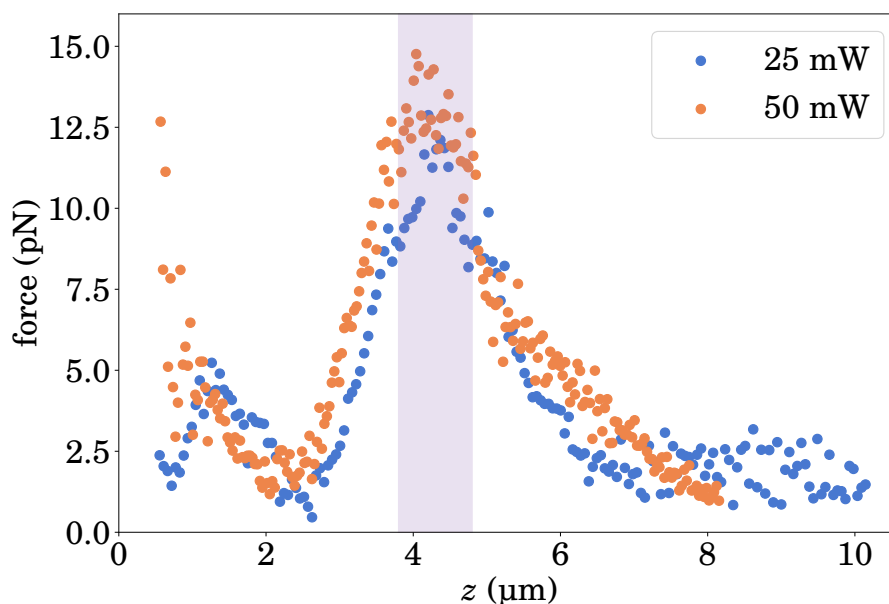
FIGURE 5.14. The axial optical force measured at different laser powers. The profiles are fundamentally the same, though the higher power maximal force is noisier, leading to a widening in the potential this is likely either an artefact of the measurement process, as the two beams were much closer in power (50/110 mW vs 25/125 mW) leading to a less tightly held beam and larger deflections. However, the highlighted region shows a stable linear region, where the force can then be altered how force in the linear region can be altered by changing the power as with the Hookean region.

5.7 Discussion

Axial optical trapping is a powerful technique, but one that comes with considerable challenges. If there is not a need for high spatio-temporal resolution then alternatives such as magnetic tweezers may be more applicable. However, if rapid feedback and base pair resolution is required, such as for weakly-interacting proteins such as NAPs then an axial optical trap would be able to provide it. Axial optical traps can also be used to perform experiments similar to those of an AFM, by moving a bead across a surface and measuring the trap displacements [225, 226] although this is only relevant when the lower forces of optical traps would be needed.

5.7.1 All-optical axial force clamping

The outstanding issue with building a more accurate all-optical axial force clamp is to utilise back-focal-plane detection whilst in the linear region of the trap. This can be achieved by utilising a weak detection laser, of a different wavelength or polarisation (the latter of which would require no modification to the trapping path, just a polarisation filter on the QPD). Another alternative is to use backscattered light to detect the bead position [227]. As long as the detection laser is small enough that it is within the margin of error of the force clamp, or is also a different enough wavelength that trapping is inefficient this work could be continued to realise an instrument capable of measuring protein-DNA interactions with DNA tethers on the order of 100s of base pairs with nanometre-resolution. While other tweezers are capable of base pair resolution, this is only for longer tethers, and so not useful for non-site-specific proteins.

5.7.2 Further improvements to optical trapping

The main downside of axial optical trapping is the inherently weaker trap stiffness compared to the lateral direction. However, there are ways of counteracting this by using non-TEM$_{00}$ modes. For example using a Laguerre-Gaussian mode with a higher l, i.e. for a cylindrical transverse mode TEM$_{0i}$ (a "doughnut" beam) removes the intensity at the centre of the beam profile (Fig. 5.15), reducing the radiation pressure, which acts to push an object out of the trap (and so also moves the trap height closer to the beam focus). Alternatively, the intensity at the centre of the beam could be removed by using a spatial light modulator (SLM), although they require more input power due to losses from the small amount of light that is reflected by the SLM. These methods would allow for stronger trapping without high levels of laser power going into the objective which can heat up the samples being measured.

Removing the centre of the trapping laser would also potentially allow for fluorescence measurements to be integrated into an axial optical trap. This is because the near-IR lasers used for optical trapping often photobleach fluorophores [199], which is a problem for short tethers when the beams overlap. Many current setups separate the laser paths in time [229, 12], but this causes the bead to move out of the trap momentarily - which becomes more significant as the tethers become shorter. The most likely method to combine axial optical trapping with fluorescence imaging would be total internal reflection fluorescence (TIRF) microscopy as it is capable of
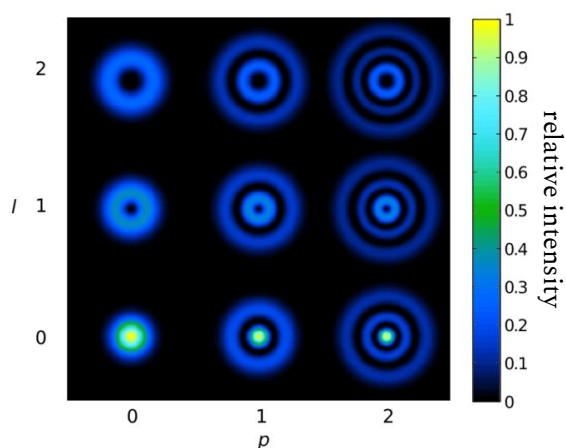
FIGURE 5.15. Intensity profiles of different laser modes. Increasing l creates increasing large holes, which acts to reduce the radiation pressure and increase the gradient force for the equivalent total laser power, which increases the trapping efficiency. Source: [228].

reaching penetration depths as low as 19 nm [230], and so can avoid fluorescent signals from the bead.

CHAPTER

6

CONCLUSIONS AND FUTURE WORK

The previous chapters examined several nucleoid-associated proteins (NAPs) and saw the dramatic changes they can induce in DNA, dependent upon the force on the DNA. Here I will review these findings and suggest future directions to continue this work as a whole.

6.1 The trouble with NAPs

The multifunctional nature of nucleoid-associated proteins makes it difficult for a single experiment to fully capture the entire behaviour of a NAP *in vitro*. H-NS, StpA and IHF are all capable of causing large deformations in the DNA structure that help to not only compact the genome but also regulate it. The increased flexibility of H-NS and StpA DNA filaments after force is applied and the multiple bending states and bridging behaviour of IHF show how the nucleoid is a highly dynamic system, where these proteins act in multiple roles. The isolated behaviours of a NAP can be used to build a model to further elucidate the function of NAPs in general. For example, now having a better understanding of the multi-modal bending behaviour of IHF the kinetics and behaviour under force is of interest, to compare to H-NS, and force spectroscopy would be able to provide this.It would also be instructive to perform AFM on H-NS/DNA complexes using the same constructs as with IHF to compare the behaviour and whether clustering is favourable.

Another complication of NAPs is that a single NAP (or unit such as dimer) will often cause a small change to DNA on the length scales that are usually accessible to many single-molecule techniques such as optical tweezers and longer length scales leads to too much non-specific binding. Atomic force microscopy is capable of imaging on DNA that is on the order of hundred of base pairs long but it cannot (easily) capture the dynamics, even in high-speed AFM due to its slower scanning speed (typically around 20 fps [231]). Although it is possible to use techniques such as TPM and magnetic tweezers, I wished to have greater precision and so set out to improve axial optical tweezers and build a passive force clamp in the axial direction, allowing for a stable force clamp even for DNA that is hundreds - and not thousands - of base pairs long.

In addition to the multiple binding behaviours of each individual NAP they also behave differently at different stages of the cell cycle and in response to environmental stress. Therefore, it is important to not only see how they act in *in vitro* experiments but to also compliment them with *in vivo* ones, such as super-resolution microscopy, to see if the isolated behaviours can help to explain the behaviour in the cell, or vice versa. For example, the difference between the H-NS-like and StpA-like mutants of StpA became more clear after the application of force, where the intermediate mutant StpA M4T behaved like H-NS before the application of force, and like StpA after. As its mutation is in the weaker of the two oligomerisation domains it shows the importance of oligomerisation to H-NS function, and how proteins that disrupt this (such as Hha) may play a role in altering H-NS function *in vivo*. In addition, many proteins also apply force to the DNA which may help to remove H-NS allowing transcription to take place.

The architecture of the bacterial nucleoid is comprised of many different nucleoid-associated proteins so their interactions with one another also need to be taken into account. I briefly did this with H-NS and StpA but there are many interactions known *in vivo* that could be explored as demonstrated in Figure 1.5. For example, HU - a homologue of IHF that prefers to form filaments - is known to antagonise H-NS [232] and the interactions of various NAPs with different genes or promoter regions could be investigated to see if there is a global pattern to silencing/anti-silencing by NAPs and related proteins.

To be able to investigate single promoter regions to isolate these behaviours short DNA sequences will need to be experimented upon due to propensity of many

NAPs to bind non-specifically. The aim of building optical axial tweezers was to reduce the length of the DNA being used to be comparable to the lengths measured with AFM, and to be able to do so accurately and precisely. While other techniques, such as magnetic tweezers, may be an option, the base pair resolution possible with optical tweezers would allow for greater determination of the small differences in, for example, a competition assay between H-NS and StpA which behave very similarly. The greatest advantage would be with the realisation of an axial passive force clamp which could allow for step-wise changes in the collapse of NAP/DNA filaments to be observed, as both H-NS [44] and IHF [116] have been shown to collapse linear DNA in assays similar to that of Chapter 3. This could help to determine how bridges form, whether the step-size is peaked around a certain value or broadly distributed and I provide some examples below.

Nucleoid-associated proteins are an incredibly important and ubiquitous family of proteins, vital to the function of bacteria in multiple ways. Although they provide a challenge due their complex nature, it is this that makes them an exciting avenue of study.

6.2 Future work

Further *in vitro* work on nucleoid-associated proteins (NAPs) will be greatly improved by moving towards experiments on shorter DNA sequences to take advantage of the specificity that experiments outside of the cell can provide. Here I give two examples of experiments that could be done.

6.2.1 Sequence dependence on short DNA tethers

The advantage of axial optical tweezers is that short DNA tethers (on the order of hundred of base pairs) can now be investigated with accurate force spectroscopy. This is particularly important for nucleoid-associated proteins. For example, with H-NS (or other filament-forming NAPs such as StpA or HU) DNA that is AT-rich or GC-rich, or more likely promoter regions, should show the differences in binding as in Figure 1.9, where GC-rich DNA was not bound. As shown in Figure 3.8, when DNA is on the length scale accessible to lateral optical tweezers (thousands of base pairs) these differences cannot be observed, due to the presence of enough AT-rich regions for H-NS to bind. To look at regions where the protein starts to oligomerise specific

promoters, such as *pagC*, could also be investigated without thousands of base pairs surrounding it. In the case of IHF, although it binds specifically, the changes it makes to DNA are small. Consequently, for longer linear DNA tethers a single kink will not noticeably alter the contour length and adding multiple binding sites would only give an average reading. Again, by going down to DNA tethers on the order of hundred of base pairs long a single binding site can be isolated and the effects a single IHF has on DNA could be determined. Finally, experimenting on this length scale would allow the same DNA constructs to be used for both optical tweezers and atomic force microscopy experiments, allowing for a visual interpretation of the force spectroscopy results, even without introducing markers needed for fluorescence microscopy.

6.2.2 Collapse and bending of NAP/DNA filaments

The observation of a permanent change in H-NS/DNA and StpA/DNA filaments under the application of force suggests the possibility of bridging, especially in the case where the negative charge of the DNA is shielded (reducing self-repulsion), where the filament collapsed over time [44]. The addition of positive charges, such as Mg^{2+}, should also be investigated, as it is also more likely to form bridges under these conditions (see Fig. 1.7).

Using a force clamp - in particular a passive all-optical force clamp - will allow for further experiments to be conducted. Shorter DNA constructs will allow for the collapse of NAP/DNA filaments to monitored over time. In particular, an H-NS dimer binds over ~20 bp (~7 nm), which is within the resolution to be able to observe possible bridging events as step changes in the contour length. The compaction of IHF (plateauing in a reduction of $\tilde{2}5\%$ of bead RMS motion) appears to occur for both DNA with and without a specific binding site [116]. In a similar manner to H-NS, monitoring the collapse of an IHF/DNA complex under a force clamp could allow step-wise changes to be observed.

In the case of IHF bending, holding the DNA extended at a low force and allowing IHF to bind would allow for the bending kinetics and transitions between the different bending modes (described in Chapter 4) to be investigated. If the DNA is short enough that these alter the contour length appreciably the kinetics between these modes of binding could be determined. This could be done with FRET but the unwrapped mode has the DNA too far apart to measure accurately (as it is

greater than 10 nm), although these two methods should ideally be combined to corroborate the trapping signal. Additionally, the force applied to the IHF to the DNA can be determined for the wrapped binding modes. In other words, the force could be increased until the fully-wrapped state can no longer form. Magnetic tweezers experiments on 445 bp DNA appeared to see only two states, with an 18 nm shift [233], which does, therefore, not include the different binding modes but complete unbending. This is because the distance between the states is small (as they can be measured by FRET). The magnetic tweezers were limited to 100 Hz measurements, whereas the bending rates are closer to 500 Hz [215] and so the higher temporal resolution with axial optical trapping could reveal the intermediate states.

DNA SEQUENCES

H ere I give more information on the DNA sequences used in the studies with
H-NS, StpA and IHF.

A.1   DNA sequences used with H-NS and StpA

H-NS was mainly investigated using a 5044bp region amplified around *pagC* that is
known to interact with H-NS *in vivo*. The DNA region has an AT content of 57.5%.
Additionally a 5000bp region around STM1033 (that has low affinity for H-NS *in
vivo*) was also used with an AT content of 53.36%. For StpA, pagC was used as well
as a 3970bp and 5073bp region from phage-λ with 58% AT.

A.2   DNA sequences used for AFM with IHF

The short (<500bp) DNA constructs are shown below. The **bold** sections are the
regions that match the IHF consensus sequence.

A.2.1 0λ361

41.6% AT Content in 361 bp

GCATCATCAAGTGCCGGTCGTGCAGCTTCCTCGGCAACGGCGGCAGAAAATT
CTGCCAGGGCGGCAAAAACGTCCGAGACGAATGCCAGGTCATCTGAAACAGC
AGCGGAACGGAGCGCCTCTGCCGCGGCAGACGCAAAAACAGCGGCGGCGGG
GAGTGCGTCAACGGCATCCACGAAGGCGACAGAGGCTGCGGGAAGTGCGGT
ATCAGCATCGCAGAGCAAAAGTGCGGCAGAAGCGGCGGCAATACGTGCAAAA
AATTCGGCAAAACGTGCAGAAGATATAGCTTCAGCTGTCGCGCTTGAGGATG
CGGACACAACGAGAAAGGGGATAGTGCAGCTCAGCAGTGCAACCAACAGCA

A.2.2 1λ302

58.9% AT content in 302 bp

CAAGACACCGGATCTGCACATTGATAACGCCCAATCTTTTTGCTCAGACTC**TA
ACTCATTGATA**TTATAAACTCCTTGCAATGTATGTCGTTTCAGCTAAACGGTA
TCAGCAATGTTTATGTAAAGAAACAGTAAGATAATACTCAACCCGATGTTTGA
GTACGGTCATCATCTGACACTACAGACTCTGGCATCGCTGTGAAGACGACGC
GAAATTCAGCATTTTCACAAGCGTTATCTTTTACAAAACCGATCTCACTCTCC
TTTGATGCGAATGCCAGCGTCAGACATCATATG

A.2.3 3λ343

70.3% AT Content in 343 bp

CTTTGTGCTTCTCTGGAGTGCGACAGGTTTGATGACAAAAAATTAGCGCAAG
AAGACAAAAATCACCTTGCGCTAATGCTCTGTTACAGGTCACTAATACCATC**T
AAGTAGTTGATT**CATAGTGACTGCATATGTTGTGTTTTACAGTATTATGTAG
TCTGTTTTTTATGCAAAATCTAATT**TAATATATTGATA**TTTATATCATTTTAC
GTTTCTCGTTCAGCTTTTTTATACTAAGTTGGCATTATAAAAAGCATTGCT**T
ATCAATTTGTTG**CAACGAACAGGTCACTATCAGTCAAAATAAAATCATTATT
TGATTTCAATTTTGTCCCACTCCCTGCC

A.2.4 3λ474

63.3% AT content in 474 bp

GATTGCGAGGCTTTGTGCTTCTGGAGTGCGACAGGTTTGATGACAAAAAATT
AGCGCAAGAAGACAAAAATCACCTTGCGCTAATGCTCTGTTACAGGTCACTAA
TACCATC**TAAGTAGTTGATT**CATAGTGACTGCATATGTTGTGTTTTACAGTA
TTATGTAGTCTGTTTTTTATGCAAAATCTAATT**TAATATATTGATA**TTTATAT
CATTTTACGTTTCTCGTTCAGCTTTTTTATACTAAGTTGGCATTATAAAAAGC
ATTGCT**TATCAATTTGTTG**CAACGAACAGGTCACTATCAGTCAAAATAAAAT
CATTATTTGATTTCAATTTTGTCCCACTCCCTGCCTCTGTCATCACGATACTGT
GATGCCATGGTGTCCGACTTATGCCCGAGAAGATGTTGAGCAAACTTATCGC
TTATCTGCTTCTCATAGAGTCTTGCAGACAAACTGCGCAACTCGTGAAAGGT

PROTEIN SYNTHESIS

The protocol to produce H-NS from *E. coli* is shown here and was carried out in conjunction with Jamieson Howard, each preparing a sample. The SDS-PAGE and activity assay shown were done by Jamieson Howard.

B.1   H-NS overexpression and purification

The pRD18 plasmid, containing H-NS [93] was transformed into BL21 (DE3) pL-yseE competent *E. coli*. These were then plated onto agar plates with LB and the antibiotics carbenicillin and chloramphenicol. Single colonies were then picked and grown overnight in 10 ml of LB, carbenicillin and chloramphenicol at 37°C.

Each overnight culture was centrifuged to obtain a pellet, which was then resuspended in 1 ml LB and used to inoculate 1 l of LB, carbenicillin and chloramphenicol. This was then grown to an OD_{600} of 0.8 by keeping at 37°C and shaking at 180 rpm. At this point overexpression of H-NS was induced by the addition of IPTG, with a final concentration of 1 mM and the cells were left to grow overnight at 37°C.

The induced cells were then harvested by centrifuging at 4°C at 4000 rpm for 20 minutes. Each obtained pellet was then resuspended in 10 ml of suspension buffer (20 mM Tris, 8 mM β-mercaptoethanol, 3 mM benzamidine, 10% glycerol, pH 7.2) and 100 mM NH_4Cl, then flash frozen in liquid nitrogen for storage. These were taken and another 10 ml of suspension buffer and 100 mM ammonium chloride was

added. The cells were then lysed in 10 ml aliquots by sonicating and the lysis was clarified (i.e. the supernatant separated) by centrifuging at 20,000 rpm at 4°C for 30 minutes. As H-NS is soluble the supernatant was collected and loaded onto a 5 ml P-cell column pre-equilibriated with suspension buffer and 100 mM NH_4Cl. The column was then run at 1 ml/min, with a 20 column-volume wash and 20 column-volume gradient where the concentration of ammonium chloride was increased from 100 mM to 1000 mM. H-NS was found to elute at around 300 mM NH_4Cl (Fig. B.1(a)).

The peak fractions (8-12) from the P-cell column were then pooled and dialysed against the suspension buffer with 130 mM NaCl. This was then loaded onto a 5 ml heparin column equilibriated with suspension buffer and 130 mM NaCl. H-NS eluted at approximately 350 mM NaCl (Fig. B.1(b)). The peak fractions 6-12) were then pooled, diluted 10× in suspension buffer and loaded onto a 5 ml heparin column equilibriated with suspension buffer and 130 mM NaCl. H-NS was found to flow through the column immediately (Fig. B.1(c)) and so the flow-through and the first 5 ml of the wash was pooled. This was then loaded directly onto a 1 ml HiTrap Heparin column equilibriated with suspension buffer and 130 mM NaCl. A 5 column-volume wash followed by a 20 column-volume gradient from 130 mM to 1000 mM NaCl was run and H-NS eluted again at ~350 mM NaCl (Fig. B.1(c)) and fractions 4-10 were pooled. Finally, this was taken and dialysed to be stored in suspension buffer with 130 mM NaCl and 20% glycerol, then flash-frozen in liquid nitrogen.

(a) Step 1: P-Cell column

(b) Step 2: Heparin column

(c) Step 3: HiTrap Q HP column

(d) Step 4: HiTrap Heparin column
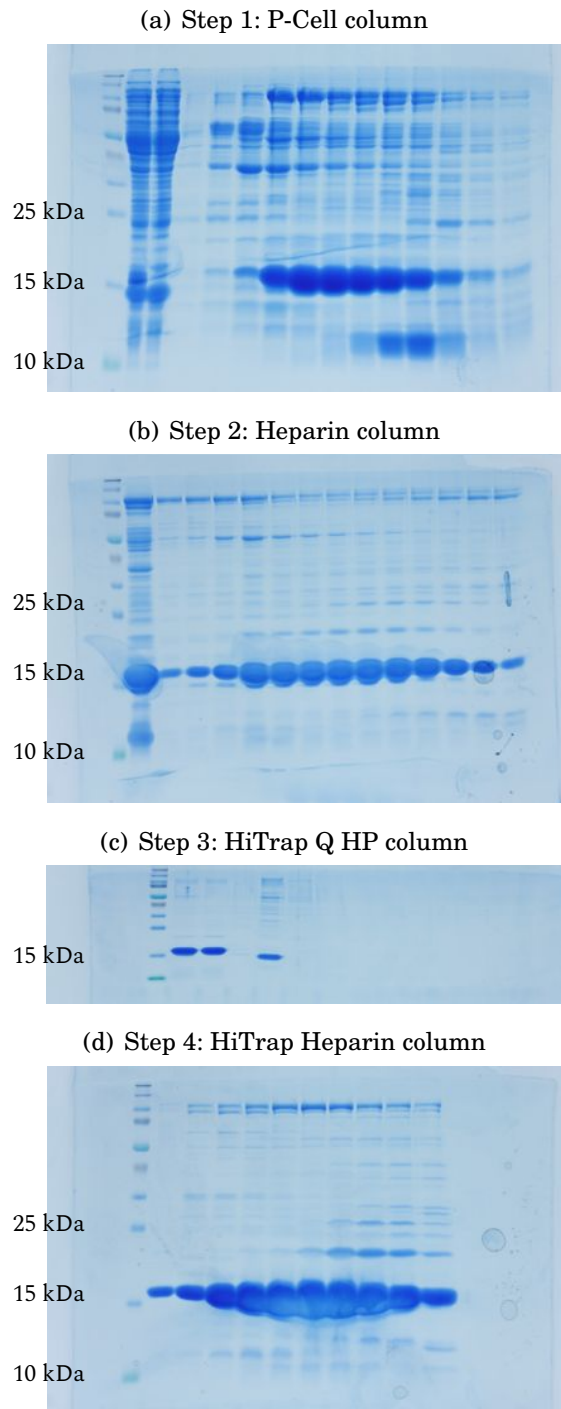
FIGURE B.1. SDS-PAGE gels of H-NS purification steps. Each purification step through a column further purifies overexpressed H-NS (the bright band at about 15 kDa) from a cell lysis until purified H-NS is obtained.
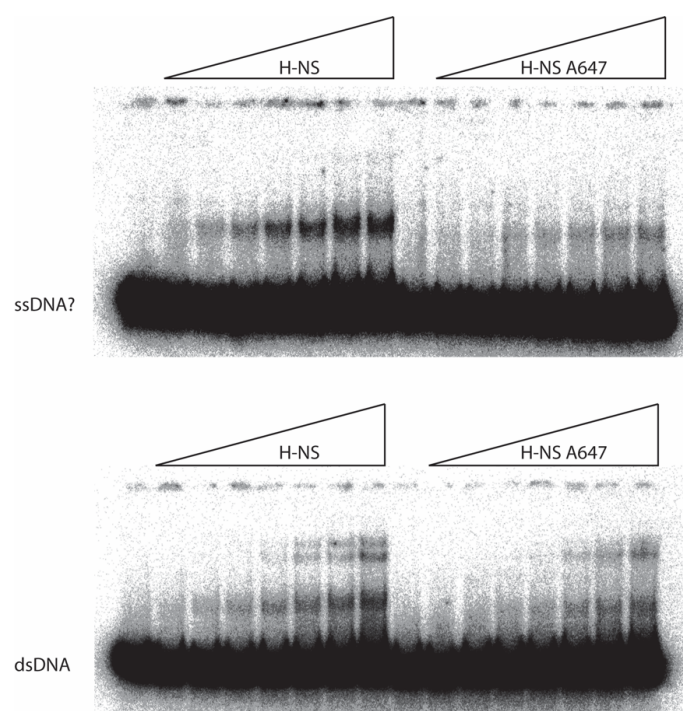
FIGURE B.2. Activity assay of H-NS and H-NS A647 (where Alexa647 was attached to H-NS via a disulphide bond (work by Jamieson Howard). As the concentration of H-NS is increased bands higher up in the gel can be seen corresponding to binding by H-NS. At even higher concentrations there are bands at a larger size, suggesting higher-order structures.

CODE EXAMPLES

Included here are parts of the code used to analyse or collect the data in this thesis using LabVIEW or Python 3 using (in addition to other specific packages) the SciPy stack and scikit-image [214].

C.1 LabVIEW interfaces for axial optical trapping
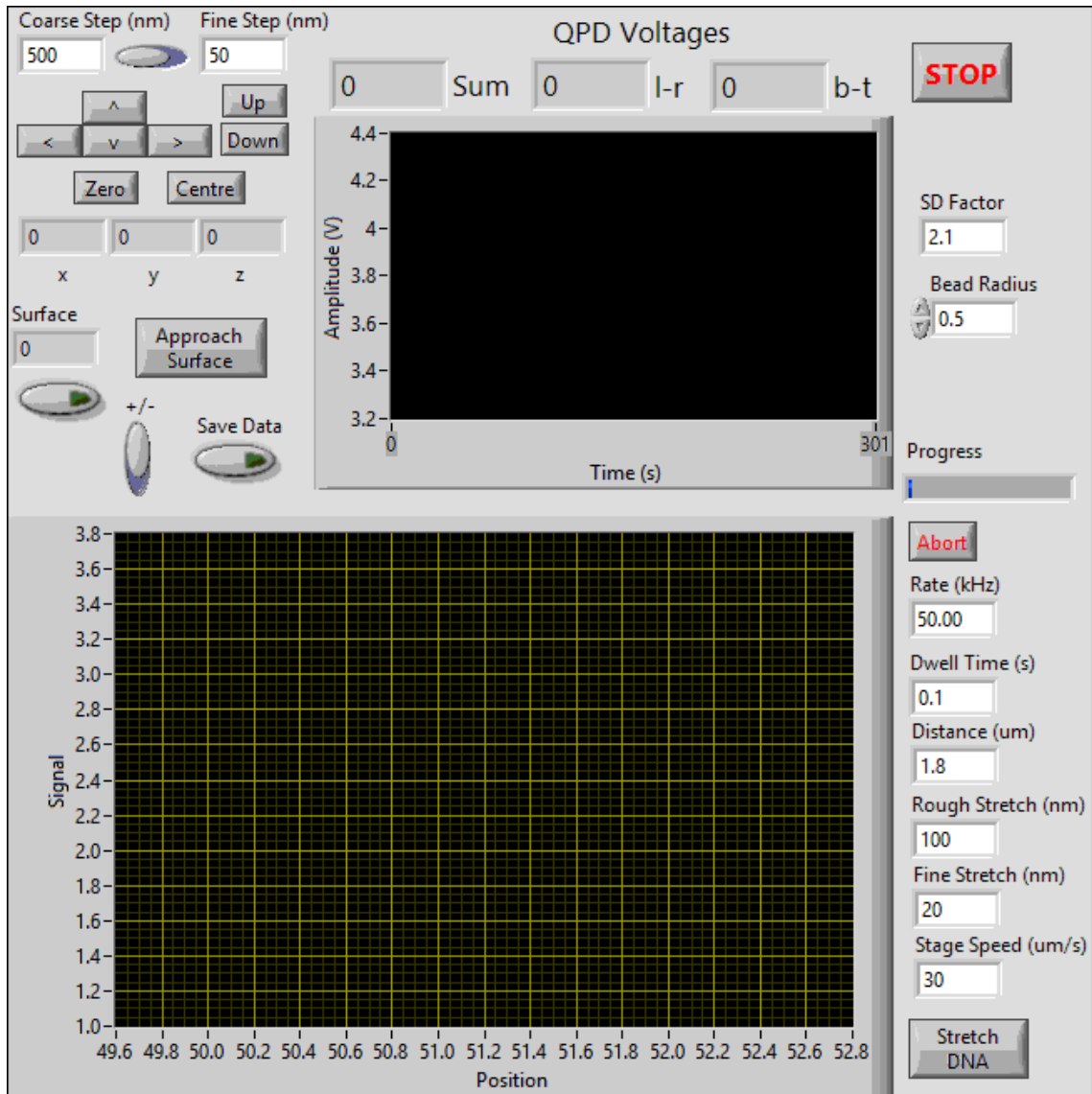
FIGURE C.1. LabVIEW interface for axial stretching with optical tweezers. A similar design was used for lateral tweezers. Coarse steps are used to quickly centre the bead over the anchor point laterally to have minimal lateral displacement when axially stretching.
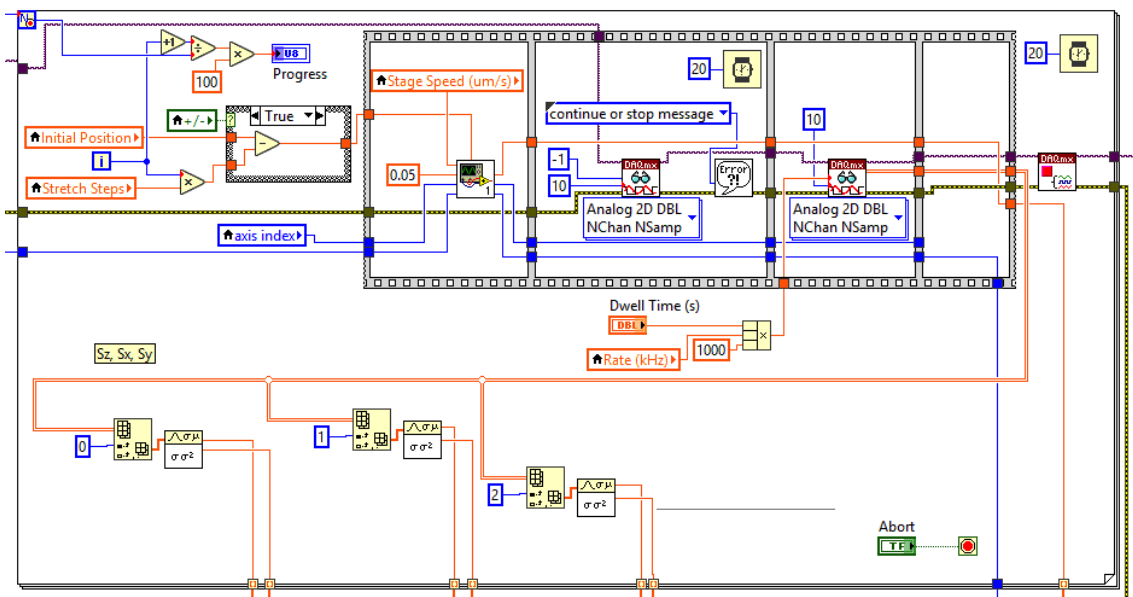
FIGURE C.2. Part of LabVIEW block diagram for axial stretching with optical tweezers. A similar design was used for lateral tweezers. The power spectrum is calculated as the LabVIEW program takes a measurement.
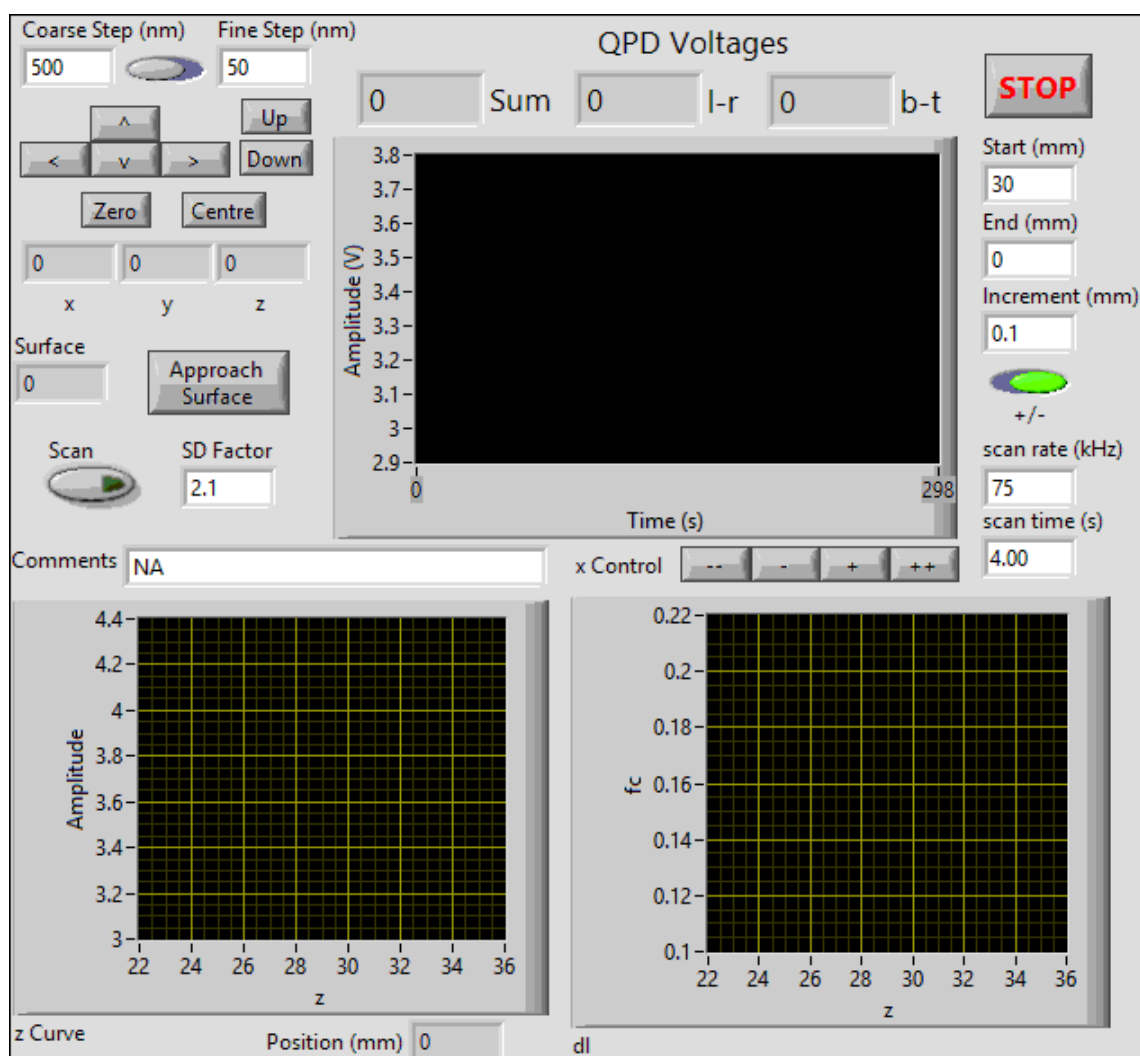
FIGURE C.3. LabVIEW interface for measuring the axial optical potential. "Approach Surface" would automatically find the surface by slowly moving down and looking for an increase in the intensity signal scaled by the "SD Factor" (i.e. how many standard deviations away). "Scan" would then move the translation stage of the lens for the probe trap, open and close the shutter for the stationary trap and take measurements of both, recording the corner frequencies, the diffusion constants (in V).
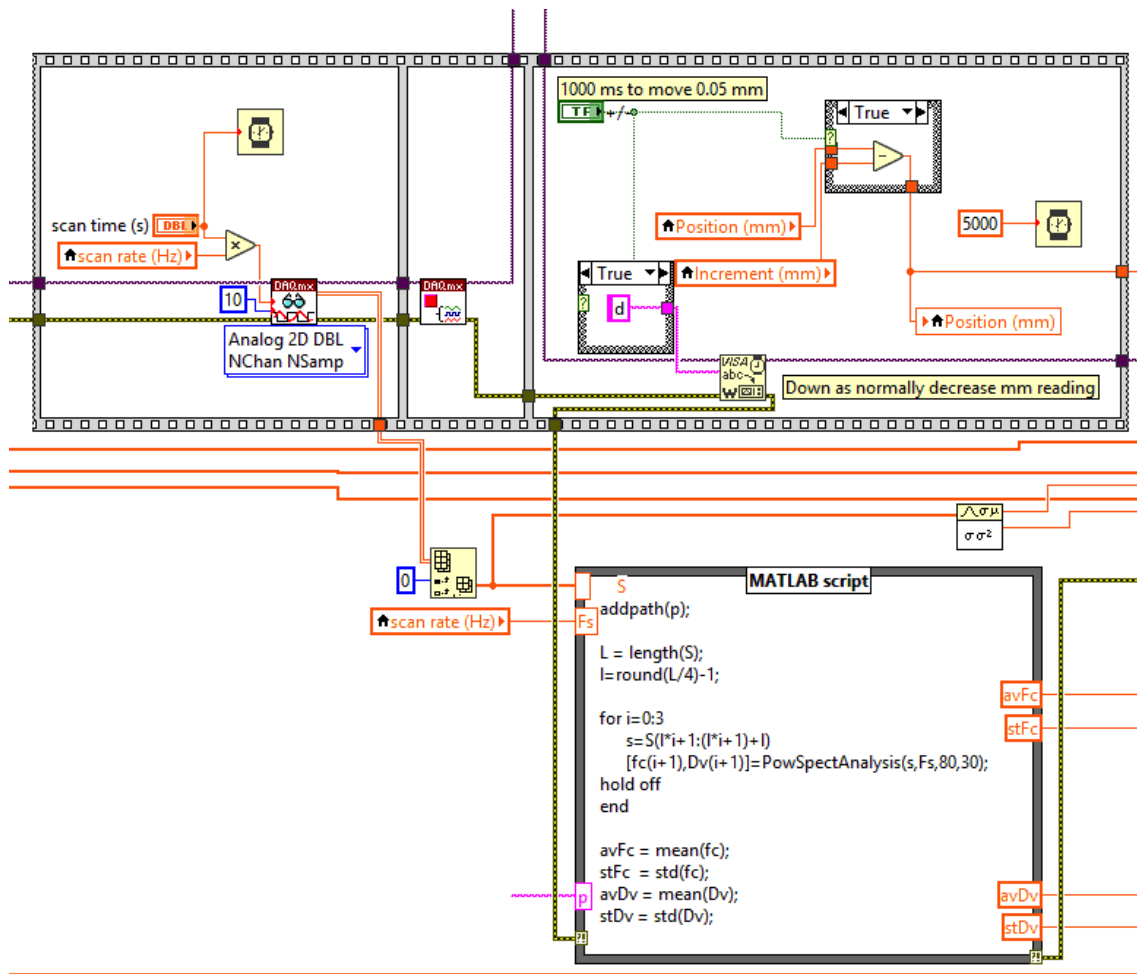
FIGURE C.4. Part of LabVIEW block diagram for measuring the axial optical potential

C.2 Code extracts to analyse a TPM trajectory

```python
import numpy as np


class RMS_to_pl:
    """
    Takes an RMS calculatd from TPM and returns a
    persistence length based on the method from
    Segall 'Bead Size Matters' paper.
    """

    def __init__(self, Lc, R=500, n_steps=4000, lp_max_fit=200):
        # contour length of DNA in nm
        self.Lc = [(Lc - 1000 + (i * 100)) * 0.34 for i in range(11)]
        self.R = R  # bead radius
        self.n_steps = n_steps  # granularity of pl
        self.lp_max_fit = lp_max_fit
        self.pl = np.linspace(0.1, self.lp_max_fit, self.n_steps)
        self.generate_conversion()

    def generate_conversion(self):
        """Run once to generate the persistence length for a range of RMSDs"""
        self.RMSD = []
        self.NR = [self.R / np.sqrt(L * self.pl / 3) for L in self.Lc]
        for (NR, L) in zip(self.NR, self.Lc):
            MSD = ((L * self.pl) / 3) * (2 + (4 * NR / (np.sqrt(np.pi) * erf(NR))))
            self.RMSD.append(np.sqrt(MSD))

    def __call__(self, value):
        """
        Will return a persistence length based from the conversion table.
        Returns NaN if out of range.
        """
        lps = []
        for RMS in self.RMSD:
            try:
                lp_max = self.pl[max(np.where(RMS < value))[-1]]
                lp_min = self.pl[min(np.where(RMS > value))[0]]
                lps.append((lp_max + lp_min) / 2)
            except IndexError:
                pass
        return np.average(lps), np.std(lps)


if __name__ == "__main__":
    convert_to_lp = RMS_to_pl()

    # obtain trajectory of x, y co-ordinated of bead motion...
    x = np.array([i[0] * pixel_scale for i in trajectory])
    y = np.array([i[1] * pixel_scale for i in trajectory])

    # find the centre drift
    x0 = moving_window(x, centering_window * fps)
    y0 = moving_window(y, centering_window * fps)

    xsq = np.power((x - x0), 2)
    ysq = np.power((y - y0), 2)
    rsq = xsq + ysq
    smoothed = moving_window(rsq, 40)

    # Parts of trajectory when the bead are stuck can be removed interactively
    # giving a selection index array
    RMSD = np.sqrt(np.mean(smoothed[selection]))
    lp, error = convert_to_lp(RMSD)
```

C.3 Calibrating an optical trap using the power spectrum

```python
import numpy as np
from lmfit import Minimizer, Parameters
from scipy.signal import periodogram, welch

kT = 1.381e-23 * 293.0


def anti_aliased_lorentzian(params, f, data=None, sides=1, N=20):
    N_values = [i - N for i in range(2 * N + 1)]
    model = 0
    for n in N_values:
        model += (params["Dv"] / (sides * np.pi ** 2)) / (
            (f + n * params["fNyq"]) ** 2 + params["fc"] ** 2
        )
    if data:
        return model - data
    return model


def lorentzian(params, f, data=None, sides=1):
    model = (params["Dv"] / (sides * np.pi ** 2)) / (
        f ** 2 + params["fc"] ** 2
    )
    if data:
        return model - data
    return model


def get_gamma(h=1, r=0.5, axial=False):
    # drag coefficient= 3*pi*eta*d in um
    gamma_0 = 3.0 * np.pi * 8.9e-4 * (2 * r * 1e-6)
    if axial:
        height_correction = (
            1.0
            - (9.0 / 8.0) * (r / h)
            + 0.5 * (r / h) ** 3
            - 0.57 * (r / h) ** 4
            + 0.2 * (r / h) ** 5
            + (7.0 / 200.0) * (r / h) ** 11
            - (1.0 / 25.0) * (r / h) ** 12
        )
    else:
        height_correction = (
            1.0
            - (9 / 16) * (r / h)
            + (1 / 8) * (r / h) ** 3
            - (45 / 256) * (r / h) ** 4
            + (1 / 16) * (r / h) ** 5
        )
    return gamma_0 / height_correction


def calculate_PSD(x, Fs, method="periodogram", window=None):
    if method == "periodogram":
        f, p = periodogram(
            x, fs=Fs, return_onesided=True, scaling="density"
        )
    elif method == "welch":
        # window="boxcar" or default "hanning"
        f, p = welch(
            x, fs=Fs, return_onesided=True, scaling="density", axis=-1
```

```
62            )
63        else:
64            raise ValueError("method needed to calc psd")
65
66        if window:
67            f = moving_average(f, window=window)
68            p = moving_average(p, window=window)
69        return f, p
70
71
72    def calibrate(f, p, axis, Fs, anti_aliasing=False, min_cutoff=None):
73        if min_cutoff:
74            p = p[f >= min_cutoff]
75            f = f[f >= min_cutoff]
76        fc = 1000 if axis != "z" else 100
77        A = 1e3
78        params = Parameters()
79        params.add("Dv", value=A)
80        params.add("fc", value=fc, min=-0, max=Fs / 2)
81        minner = Minimizer(lorentzian, params, fcn_args=(f, p))
82        result = minner.minimize()
83
84        if anti_aliasing:
85            params = Parameters()
86            params.add("Dv", value=result.params["Dv"].value)
87            params.add(
88                "fc", value=result.params["fc"].value, min=-0, max=Fs / 2
89            )
90            params.add("fNyq", value=Fs / 2, vary=False)
91            minner = Minimizer(
92                anti_aliased_lorentzian, params, fcn_args=(f, p)
93            )
94            result = minner.minimize()
95        return result
```

C.4   Code to fit the worm-like chain

The QPD correction here is based on code by Haowei Wang.

```
1    import numpy as np
2    from scipy.optimize import curve_fit
3    from scipy.stats import linregress
4
5
6    def odd_centre(x, x0, a, b, c, z0):
7        return a * (x - x0) ** 1 + b * (x - x0) ** 3 + c * (x - x0) ** 5 + z0
8
9
10   def even_centre(x, x0, a, b, c, z0):
11       return a * (x - x0) ** 2 + b * (x - x0) ** 4 + c * (x - x0) ** 6 + z0
12
13
14   def WLC_var(x, lp, L):
15       """If leaving L as free parameter"""
16       return (4.114 / lp) * (1 / (4 * (1 - x / L) ** 2) - 0.25 + x / L)
17
18
19   def WLC(x, lp):
20       return (4.114 / lp) * (1 / (4 * (1 - x) ** 2) - 0.25 + x)
21
22
23   def QPDCorr(x, a, c, d):
24       # fit = a*x + b + c*x[0] + d*x[-1]
```

```
25      fit1 = a * x
26      fit2 = c * x[0]
27      fit3 = d * x[-1]
28      fit4 = np.append(fit3, fit2)
29      fit4 = [fit2, 0, fit3]
30      fit = fit1 + fit4
31      return fit
32
33
34 def fit_wormlike_chain(
35      position,
36      signal,
37      sensitivity,
38      k,
39      other_signal,
40      other_sensitivity,
41      other_k,
42      z_offset,
43      z_sensitivity,
44      k_z,
45 ):
46      relax_right = position[0] > position[1]
47
48      # centering
49      position = position - np.median(position)
50
51      # fit z signal to even polynomial to find centre
52      for i in range(5):
53          popt, pcov = curve_fit(
54              even_centre,
55              position,
56              z_offset,
57              p0=[0, 1, 1, 1, np.mean(z_offset)],
58          )
59          position = position - popt[0]
60          z_offset = z_offset - popt[-1]
61          # force = force + force[(min(abs(position)))]
62      z_offset = z_offset * z_sensitivity
63
64      # fit off-axis signal to even polynomial to find centre
65      for i in range(2):
66          popt, pcov = curve_fit(odd_centre, position, signal)
67          position = position - popt[0]
68          signal = signal - popt[-1]
69
70      other_signal = other_signal - np.median(
71          other_signal[np.where(abs(position) < 0.5)]
72      )
73
74      z_threshold = 50  # in nm
75      x_thresholded = position[z_offset < z_threshold]
76      y_thresholded = signal[z_offset < z_threshold]
77      centre_point = (
78          min(position[z_offset < z_threshold])
79          + max(position[z_offset < z_threshold])
80      ) / 2
81
82      x_QPD = [
83          x_thresholded[0],
84          min(abs(x_thresholded)),
85          x_thresholded[-1],
86      ]
87      y_QPD = [
88          y_thresholded[0],
89          y_thresholded[abs(x_thresholded) == min(abs(x_thresholded))][0],
90          y_thresholded[-1],
```

```
 91      ]
 92      slope, intercept, r_value, p_value, std_err = linregress(
 93          x_QPD, y_QPD
 94      )
 95      slope1, intercept1, r_value, p_value, std_err = linregress(
 96          x_QPD[0:2], y_QPD[0:2]
 97      )
 98      slope2, intercept2, r_value, p_value, std_err = linregress(
 99          x_QPD[1:3], y_QPD[1:3]
100      )
101
102      left_correction = slope1 - slope
103      right_correction = slope2 - slope
104      signal[position < 0] = (
105          signal[position < 0] - (left_correction) * position[position < 0]
106      )
107      signal[position > 0] = (
108          signal[position > 0]
109          - (right_correction) * position[position > 0]
110      )
111
112      displacement = signal * sensitivity
113
114      force = np.sqrt(
115          (k * displacement) ** 2
116          + (k_z * z_offset) ** 2
117          + (other_k * other_signal * other_sensitivity) ** 2
118      )
119
120      # split into stretch and relax curves
121      masks = [(position < 0), (position > 0)]
122      code = (
123          ["Stretch: ", "Relax: "]
124          if relax_right
125          else ["Relax: ", "Stretch: "]
126      )
127
128      for i in range(2):
129          mask = masks[i]
130          distance = np.sqrt(
131              (position[mask] - displacement[mask]) ** 2
132              + (z_offset[mask] + r + h) ** 2
133              + (other_signal * other_scale) ** 2
134          )
135          L_fit = np.abs(distance - r) / Lc
136          F_fit = abs(force[mask])
137
138          fit_mask = (L_fit < max_fit_range) & (L_fit > min_fit_range)
139          popt, pcov = curve_fit(
140              WLC, L_fit[fit_mask], F_fit[fit_mask], p0=[50.0]
141          )
142          lp = popt[0]
```

C.5 Code snippets for axial calibrations and optical potential

The measured intensity is fit to the axial_oscillationsfunction to extract L_1 and L_2, which correct the stage position z, to height, h. The other parameters can then

be fit with the same function, modifying what parameters are allowed and varied to get the correct functional forms.

```python
import numpy as np
import lmfit

# oscillation parameter based on wavelength
K_SIN = 4 * 1.33 * np.pi / 1.064  # in um


def find_surface(z, I, guess=0):
    """Guess surface to be able to fit a linear line
       and oscillations so can find intersection"""
    perr = 100000
    z0, m, c = 0, 0, 0
    for i in np.linspace(guess - 1.0, guess + 1.0, num=5000):
        if np.size(z[np.where(z <= i)]) > 5:
            x = z[np.where(z <= i)]
            y = I[np.where(z <= i)]
            popt, pcov = curve_fit(linear_fit, x, y)
            if np.sum(np.sqrt(np.diag(pcov))) < perr:
                perr = np.sum(np.sqrt(np.diag(pcov)))
                m = popt[0]
                c = popt[1]
                z0 = i
    return z0, m, c


def axial_oscillations(params, x, data=None):
    """Use lmfit as can turn params on and off to be able to use
       this for all the different oscillation functions"""
    p = params
    L = p["L1"] * x + p["L2"] * x ** 2
    Pbg = p["p0"] + p["p1"] * x + p["p2"] * x ** 2 + p["p3"] * x ** 3
    model = Pbg + p["b"] * np.exp(-p["wl"] * L) * np.sin(
        p["alpha"] * K_SIN * L + p["phi"]
    )
    if data is not None:
        return model - data
    return model
```

For the potential experiments, after calibrating the corrected heights, h and force at each height is known by taking the difference of the two intensities and multiplying by the trap stiffness at that height. The trap centre is then determined as the minimum force within the linear region, allowing for the force to be fitted.

```python
import numpy as np
from scipy.optimize import curve_fit


def dGauss(x, a, b):
    return -1.0 * a * x * np.exp(-b * x ** 2)


def Gaussian(x, a, b):
    return a * np.exp(-b * (x) ** 2)


x_fit = h[h >= trap_centre]
f_fit = force[h >= trap_centre]  # move into fN

x_min = x_fit[0]
```

```
17 x_fit = x_fit - x_fit[0]
18
19 popt, pcov = curve_fit(dGauss, x_fit, f_fit, maxfev=100000)
20
21 # Convert the fit to the right values for the Gaussian
22 a = popt[0] / (-2.0 * popt[1])
23 b = popt[1]
24 xV = np.linspace(-2.0, 2.0, num=50)
25 V = -1.0 * Gaussian(xV, a, b)
```

C.6 Code to analyse AFM images

Included here is an object to take an SPM image and extract DNA skeletons from it.

```
 1 import numpy as np
 2 import numpy.ma as ma
 3 from scipy import ndimage as ndi
 4 from skimage import filters, graph, img_as_bool, morphology
 5 from image_processing.afm_loader import afmLoader
 6 from image_processing.array_helpers import (
 7     get_coord_pairs,
 8     pad_to_square,
 9     skeleton_endpoints,
10     trim_zeros,
11 )
12
13
14 class dnaFinder(afmLoader):
15     def __init__(
16         self,
17         filename,
18         channel="Height Sensor",
19         filetype="bruker",
20         contour_length=302,
21     ):
22         super().__init__(filename, channel=channel, filetype=filetype)
23         self.scale = self._px2real(1, 1)[0] * 1e3  # x, y in um --> nm
24         self.contour_length = contour_length * 0.34  # bp --> nm
25
26     def get_mask(self, sigma=2, plot=False):
27         try:
28             filtered = filters.gaussian(self.image, sigma=sigma)
29         except ValueError as e:
30             # if np.unique(self.image) == None:
31             if None in self.image:
32                 raise EmptyImageError  # faster only checking here
33             else:
34                 raise e
35
36         threshold = filters.threshold_local(filtered, 11, param=3)
37         mask = filtered >= threshold
38         return mask, threshold
39
40     def get_segments(self, crop=False, spacing=5):
41         labelled, n_segments = ndi.label(self.mask)
42         segments = [
43             img_as_bool(labelled == i) for i in range(1, n_segments - 1)
44         ]
45
46         if crop:
47             cropped = []
48             for segment in segments:
```

```
49              x_range, y_range = segment.shape
50              xs, ys = np.where(segment != 0)
51              min_x = min(xs) - spacing if min(xs) > spacing else 0
52              max_x = (
53                  max(xs) + spacing
54                  if max(xs) + spacing < x_range
55                  else x_range
56              )
57              min_y = min(ys) - spacing if min(ys) > spacing else 0
58              max_y = (
59                  max(ys) + spacing
60                  if max(ys) + spacing < y_range
61                  else y_range
62              )
63              cropped.append(segment[min_x:max_x, min_y:max_y])
64          return cropped
65      return segments
66
67  def skeletonize(self, use_masks=True):
68      if use_masks:
69          skeletons = [
70              morphology.skeletonize(morphology.binary_erosion(mask))
71              for mask in self.segmented_masks
72          ]
73          # skeletons = [morphology.thin(morphology.erosion(mask)) for mask in
    self.segmented_masks]
74          # skeletons = [morphology.medial_axis(morphology.erosion(mask)) for
    mask in self.segmented_masks]
75          # skeletons = [morphology.skeletonize_3d(morphology.binary_erosion(mask
    )) for mask in self.segmented_masks]
76      else:
77          skeletons = [
78              morphology.skeletonize(segment > 0)
79              for segment in self.segments
80          ]
81      return skeletons
82
83  def process_segments(self, trim=True, remove_small=True):
84      # masks are inverse so == False
85      seg_images = [
86          ma.array(self.image, mask=np.logical_not(segment), copy=True)
87          for segment in self.segments
88      ]
89      seg_masks = [
90          ma.array(
91              self.mask,
92              mask=np.logical_not(segment),
93              fill_value=1,
94              copy=True,
95          )
96          for segment in self.segments
97      ]
98
99      if trim:
100         seg_images = [
101             pad_to_square(trim_zeros(ma.filled(x, 0)))
102             for x in seg_images
103         ]
104         seg_masks = [img > 0 for img in seg_images]
105         if remove_small:
106             new_seg_images = []
107             new_seg_masks = []
108
109             for image, mask in zip(seg_images, seg_masks):
110                 if image.size > 50:
111                     new_seg_images.append(image)
```

```
112                             new_seg_masks.append(mask)
113
114                 seg_images = new_seg_images
115                 seg_masks = new_seg_masks
116
117         return seg_images, seg_masks
118
119     def get_contour_length(self, trace):
120         contour_length = 0
121         x0, y0 = trace[0]
122         for x, y in trace[1:]:
123             rsq = (x - x0) ** 2 + (y - y0) ** 2
124             contour_length += np.sqrt(rsq)
125             x0, y0 = x, y
126         contour_length = self.scale * contour_length
127         return contour_length
128
129     def get_euclidean_distance(self, endpoints):
130         e2e = np.sqrt(
131             (endpoints[0][0] + endpoints[1][0]) ** 2
132             + (endpoints[0][1] + endpoints[1][1]) ** 2
133         )
134         return e2e * self.scale
135
136     def skeleton_stats(self, skeletons=None, verbose=0):
137         distances = []
138         euclidean = []
139         coords = []
140         ids = []
141         weights = []
142         skeletons = skeletons if skeletons else self.skeletons
143
144         for i, skeleton in enumerate(skeletons):
145             if np.any(np.asarray(skeleton.shape) > 50):
146                 continue
147
148             intarr = ~skeleton.astype(int) + 2
149             endpoints = np.array(
150                 skeleton_endpoints(np.array(skeleton).astype(int))
151             ).T
152             if (len(endpoints) == 1) or not len(endpoints):
153                 continue
154             coord_pairs = get_coord_pairs(endpoints)
155
156             max_length = -1  # avoid 0 lengths before filtering
157             best_indices = None
158             idx = None
159             for j, epp in enumerate(coord_pairs):
160                 try:
161                     indices, weight = graph.route_through_array(
162                         intarr,
163                         (epp[0][1], epp[0][0]),
164                         (epp[1][1], epp[1][0]),
165                         geometric=False,
166                     )
167                 except ValueError:
168                     continue
169                 indices = np.array(indices).T
170                 path = np.zeros_like(intarr)
171                 path[indices[0], indices[1]] = 1
172                 if np.sum(path) > max_length:
173                     max_length = np.sum(path)
174                     idx = j
175                     best_indices = indices.T
176                     best_endpoints = epp
177                     best_weight = weight
```

```
178
179            if max_length > np.ceil(
180                0.75 * self.contour_length / self.scale
181            ) and max_length < np.ceil(
182                1.25 * self.contour_length / self.scale
183            ):
184                    distances.append(self.get_contour_length(best_indices))
185                    euclidean.append(
186                        self.get_euclidean_distance(best_endpoints)
187                    )
188                    coords.append(best_indices)
189                    ids.append(i)
190                    weights.append(best_weight)
191
192        total_branches = len(distances)
193        filtered_distances = []
194        filtered_euclidean = []
195        filtered_coords = []
196        filtered_ids = []
197        for idn, bd, ed, cd, wt in zip(
198            ids, distances, euclidean, coords, weights
199        ):
200            if (
201                (
202                    bd > min_Lc_scale * self.contour_length
203                    and bd < max_Lc_scale * self.contour_length
204                )
205                and (ed < 1.6 * self.contour_length)
206                and (wt < 13.0)
207            ):
208                filtered_ids.append(idn)
209                filtered_distances.append(bd)
210                filtered_euclidean.append(ed)
211                filtered_coords.append(cd)
212
213        if verbose >= 1:
214            print(
215                len(filtered_distances),
216                "out of",
217                total_branches,
218                "branches remaining",
219            )
220        return (
221            filtered_ids,
222            filtered_distances,
223            filtered_euclidean,
224            filtered_coords,
225        )
226
227    def get_line_profiles(self):
228        zs = []
229
230        for idx, coords in zip(self.filtered_ids, self.skel_coords):
231            add = True
232            x0, y0 = coords[0]
233            z = [(0, self.segmented_images[idx][int(x0), int(y0)])]
234            r = 0
235            for x, y in coords[1:]:
236                r += ((x - x0) ** 2 + (y - y0) ** 2) ** 0.5 * self.scale
237                h = self.segmented_images[idx][int(x), int(y)]
238                z.append((r, h))
239                x0, y0 = x, y
240            zs.append(z)
241        return zs
```

138

SIMULATIONS OF IHF WITH DNA

H ere I include examples of IHF simulations carried out by George D. Watson, to illustrate the different binding modes proposed based upon my experimental results in Chapter 4.

D.1 Regions of IHF binding
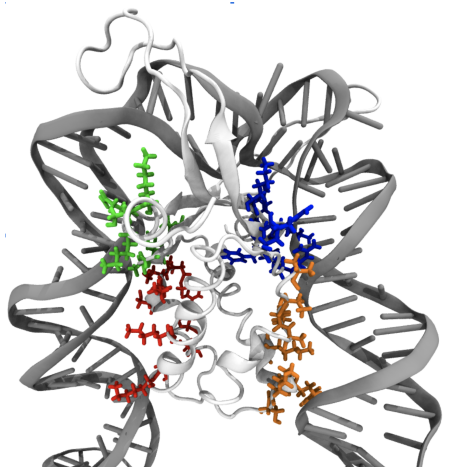
FIGURE D.1. Colour-codes regions of IHF that can bind to DNA (the canonical state is shown). Provided by George D. Watson.

D.2 Simulations of DNA/IHF binding modes
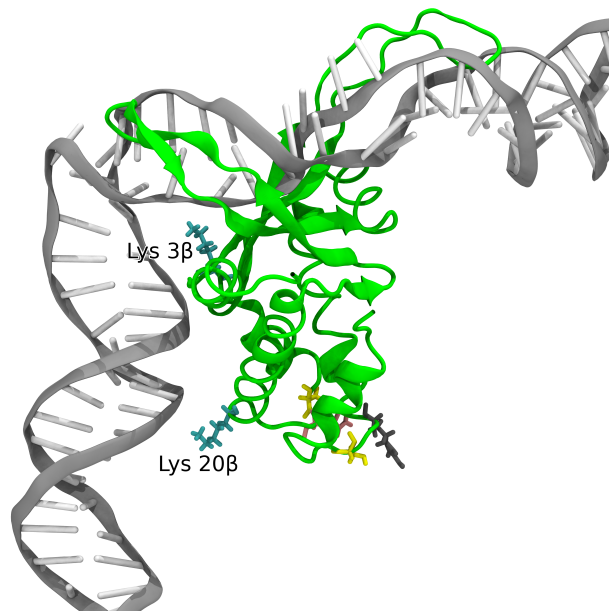
FIGURE D.2. A simulation of IHF/DNA in the associated state. Provided by
George D. Watson.
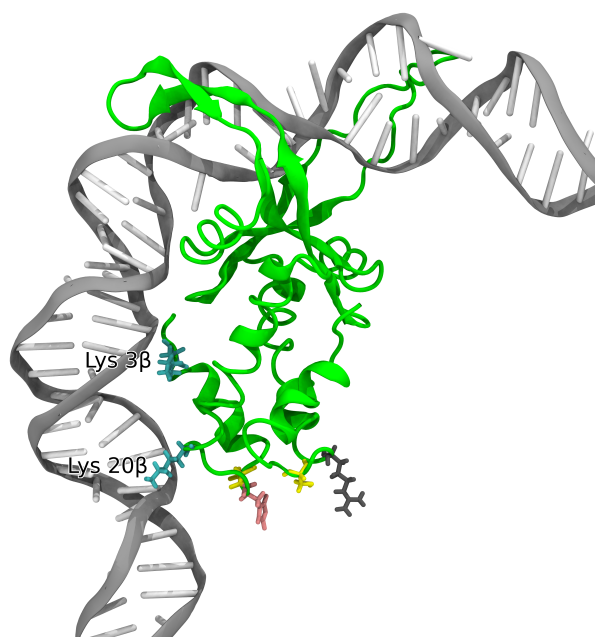
FIGURE D.3. A simulation of IHF/DNA in the half-wrapped state. Provided by George D. Watson.
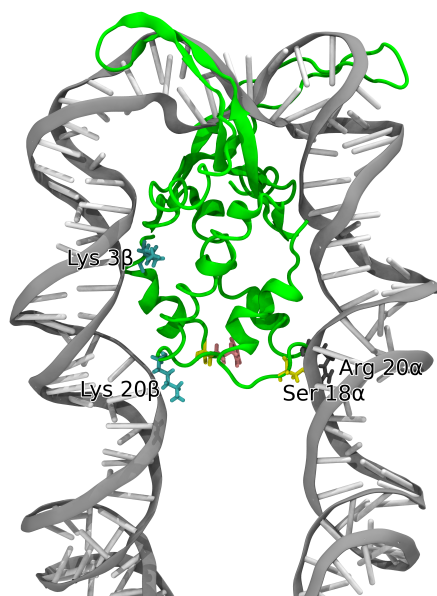
FIGURE D.4. A simulation of IHF/DNA in the fully wrapped state. Provided by George D. Watson.
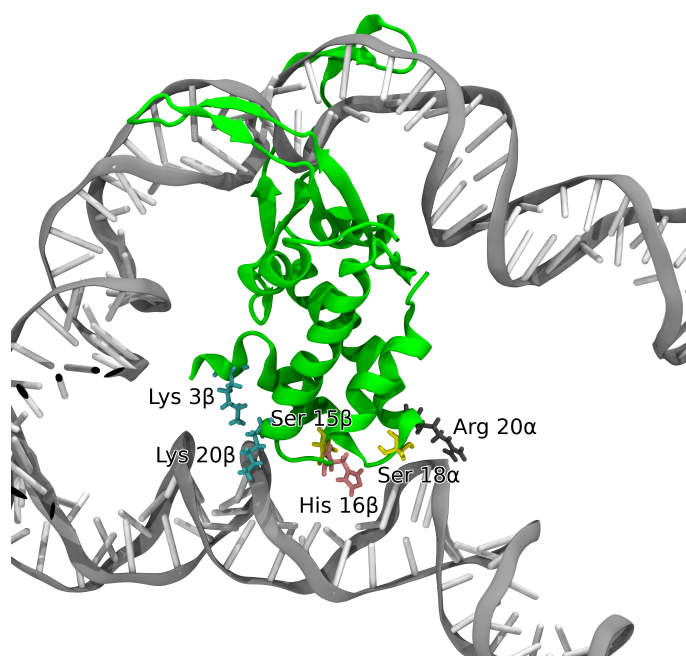
FIGURE D.5. A simulation example of IHF bridging two pieces of DNA. Provided by George D. Watson.

D.3 Free Energy Landscape

A free-energy landscape was determined that shows the difference between the left and right arms. Not shown is that the free energy of bridging is an even deeper well, supporting the AFM images where clusters seem preferable.
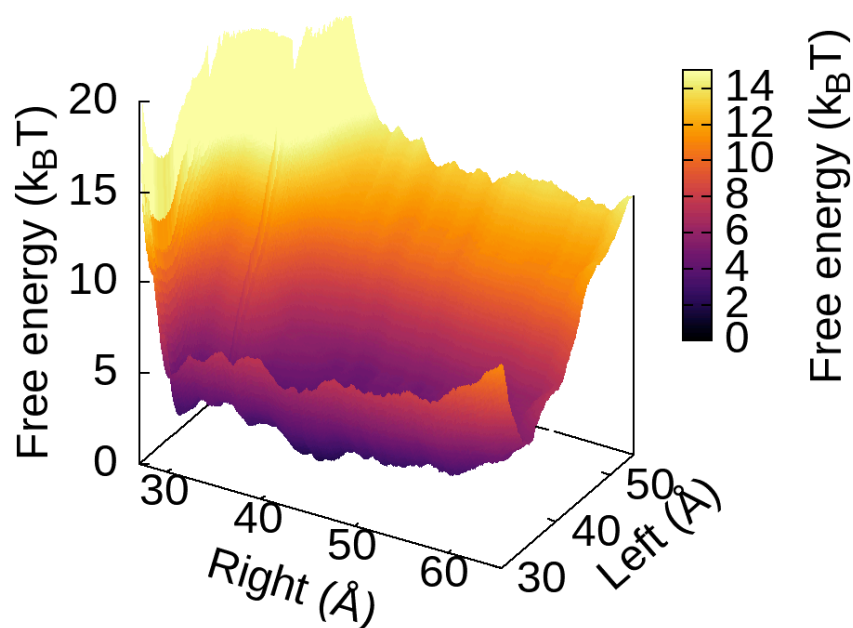
FIGURE D.6. Free energy landscape of IHF binding to 1λ302 from molecular dynamics simulations by George D. Watson. The left side has a steep well, whilst the right side is a shallow well with two local minima, corresponding to the partially and fully wrapped states.

LIST OF ABBREVIATIONS

AFM atomic force microscopy.
AM-AFM amplitude modulation AFM.
APTES (3-Aminopropyl)triethoxysilane.

BFP back-focal plane.

DMSO dimethyl sulphoxide.
DNA deoxyribonucleic acid.
DNAp DNA polymerase.
DTT dithiothreitol.

E. coli *Escherichia coli*.
EDTA ethylenediaminetetraacetic acid.

FJC freely-jointed chain.
FLIM fluorescence lifetime imaging.
FRAP fluorescence recovery after photobleaching.
FRET fluorescence resonance energy transfer.

H-NS DNA-binding protein H-NS.
HEPES 4-(2-hydroxyethyl)-1-piperazineethanesulfonic acid.
HGT horizontal gene transfer.
Hha hemolysin expression-modulating protein.
HU DNA-binding protein HU.

IHF integration host factor.
IPTG Isopropyl beta-D-1-thiogalactopyranoside.
IR infrared.

LB lysogeny broth.

NA numerical aperture.
NAP nucleoid-associated protein.

OD optical density.
OT optical tweezers.

144

PBS phosphate-buffered saline.
PCR polymerase chain reaction.

QPD quadrant photodiode.

RMS root mean square.
RMSD root mean square deviation (of bead motion).
RNA ribonucleic acid.
RNAP RNA polymerase.

S. typhimurium *Salmonella typhimurium*.
SDS-PAGE sodium dodecyl sulfateâĂŞpolyacrylamide gel electrophoresis.
SLM spatial light modulator.
smFRET single-molecule fluorescence resonance energy transfer.
SPM scanning probe microscopy.
StpA DNA-binding protein StpA.

TFM tethered-fluorophore motion.
TIRF total internal reflection fluorescence.
TPM tethered-particle motion.

WLC worm-like chain.

[1] J. D. WATSON AND F. H. CRICK, *Molecular structure of nucleic acids; a structure for deoxyribose nucleic acid*, Nature, 171 (1953), pp. 737–738.

[2] F. OOSAWA, *Biophysics: fifty years after schrödinger*, Adv. Biophys., 32 (1996), pp. 1–15.

[3] R. M. DICKSON, A. B. CUBITT, R. Y. TSIEN, AND W. E. MOERNER, *On/off blinking and switching behaviour of single molecules of green fluorescent protein*, Nature, 388 (1997), pp. 355–358.

[4] E. BETZIG, G. H. PATTERSON, R. SOUGRAT, O. W. LINDWASSER, S. OLENYCH, J. S. BONIFACINO, M. W. DAVIDSON, J. LIPPINCOTT-SCHWARTZ, AND H. F. HESS, *Imaging intracellular fluorescent proteins at nanometer resolution*, Science, 313 (2006), pp. 1642–1645.

[5] T. A. KLAR, E. ENGEL, AND S. W. HELL, *Breaking abbe's diffraction resolution limit in fluorescence microscopy with stimulated emission depletion beams of various shapes*, Phys. Rev. E Stat. Nonlin. Soft Matter Phys., 64 (2001), p. 066613.

[6] V. J. MORRIS, A. R. KIRBY, AND A. P. GUNNING, *Atomic force microscopy for biologists*, World Scientific, 1999.

[7] G. E. FOERSTER, P. Q. BEHRENS, AND R. L. AIRTH, *BIOLUMINESCENCE AND OTHER CHARACTERISTICS OF COLLYBIA VELUTIPES*, Am. J. Bot., 52 (1965), pp. 487–495.

[8] R. B. SEKAR AND A. PERIASAMY, *Fluorescence resonance energy transfer (FRET) microscopy imaging of live cell protein localizations*, J. Cell Biol., 160 (2003), pp. 629–633.

[9] K. C. NEUMAN AND A. NAGY, *Single-molecule force spectroscopy: optical tweezers, magnetic tweezers and atomic force microscopy*, Nat. Methods, 5 (2008), pp. 491–505.

[10] A. CANDELLI, G. J. L. WUITE, AND E. J. G. PETERMAN, *Combining optical trapping, fluorescence microscopy and micro-fluidics for single molecule*

studies of DNA–protein interactions, Phys. Chem. Chem. Phys., 13 (2011), pp. 7263–7272.

[11] T. T. M. NGO, R. ZHOU, J. YODH, AND T. HA, *Asymmetric unwrapping of nucleosome revealed by single molecule Fluorescence-Force spectroscopy*, Biophys. J., 104 (2013), p. 210a.

[12] K. D. WHITLEY, M. J. COMSTOCK, AND Y. R. CHEMLA, *High-Resolution "fleezers": Dual-Trap optical tweezers combined with Single-Molecule fluorescence detection*, Methods Mol. Biol., 1486 (2017), pp. 183–256.

[13] Y. E. GOLDMAN, *Kinetics of the actomyosin ATPase in muscle fibers*, Annu. Rev. Physiol., 49 (1987), pp. 637–654.

[14] A. MEHTA, *Myosin learns to walk*, J. Cell Sci., 114 (2001), pp. 1981–1998.

[15] A. YILDIZ, J. N. FORKEY, S. A. MCKINNEY, T. HA, Y. E. GOLDMAN, AND P. R. SELVIN, *Myosin V walks hand-over-hand: single fluorophore imaging with 1.5-nm localization*, Science, 300 (2003), pp. 2061–2065.

[16] M. T. WOODSIDE, W. M. BEHNKE-PARKS, K. LARIZADEH, K. TRAVERS, D. HERSCHLAG, AND S. M. BLOCK, *Nanomechanical measurements of the sequence-dependent folding landscapes of single nucleic acid hairpins*, Proc. Natl. Acad. Sci. U. S. A., 103 (2006), pp. 6190–6195.

[17] A. WERON, K. BURNECKI, E. J. AKIN, L. SOLÉ, M. BALCEREK, M. M. TAMKUN, AND D. KRAPF, *Ergodicity breaking on the neuronal surface emerges from random switching between diffusive states*, Sci. Rep., 7 (2017), p. 5404.

[18] W. COLOMB AND S. K. SARKAR, *Dynamic fluctuations in single-molecule biophysics experiments comment on "extracting physics of life at the molecular level: A review of single-molecule data analyses"*, Phys. Life Rev., 13 (2015), pp. 148–149.

[19] A. V. WEIGEL, B. SIMON, M. M. TAMKUN, AND D. KRAPF, *Ergodic and nonergodic processes coexist in the plasma membrane as observed by single-molecule tracking*, Proc. Natl. Acad. Sci. U. S. A., 108 (2011), pp. 6438–6443.

[20] I. J. FINKELSTEIN AND E. C. GREENE, *Molecular traffic jams on DNA*, Annu. Rev. Biophys., 42 (2013), pp. 241–263.

[21] D. S. GOODSELL, *Putting proteins in context: scientific illustrations bring together information from diverse sources to provide an integrative view of the molecular biology of cells*, Bioessays, 34 (2012), pp. 718–720.

[22] R. T. DAME, C. WYMAN, AND N. GOOSEN, *Structural basis for preferential binding of H-NS to curved DNA*, Biochimie, 83 (2001), pp. 231–234.

[23] M. DOI, S. F. EDWARDS, AND S. F. EDWARDS, *The Theory of Polymer Dynamics*, Clarendon Press, 1988.

[24] J. F. MARKO AND E. D. SIGGIA, *Statistical mechanics of supercoiled DNA*, Phys. Rev. E Stat. Phys. Plasmas Fluids Relat. Interdiscip. Topics, 52 (1995), pp. 2912–2938.

[25] J. BASCHNAGEL, H. MEYER, J. WITTMER, I. KULIĆ, H. MOHRBACH, F. ZIEBERT, G.-M. NAM, N.-K. LEE, AND A. JOHNER, *Semiflexible chains at surfaces: Worm-Like chains and beyond*, Polymers, 8 (2016).

[26] D. R. TREE, A. MURALIDHAR, P. S. DOYLE, AND K. D. DORFMAN, *Is DNA a good model polymer?*, Macromolecules, 46 (2013).

[27] E. N. TRIFONOV, R. K. Z. TAN, AND S. C. HARVEY, *Static persistence length of DNA*, Structure and expression : proceedings of the Fifth Conversation in the Discipline Biomolecular Stereodynamics held at the State University of New York at Albany, June 2-6, 1987 / edited by M.H. Sarma & R.H. Sarma, (1988).

[28] Y. SEOL, J. LI, P. C. NELSON, T. T. PERKINS, AND M. D. BETTERTON, *Elasticity of short DNA molecules: theory and experiment for contour lengths of 0.6-7 microm*, Biophys. J., 93 (2007), pp. 4360–4373.

[29] M. D. WANG, H. YIN, R. LANDICK, J. GELLES, AND S. M. BLOCK, *Stretching DNA with optical tweezers*, Biophys. J., 72 (1997), pp. 1335–1346.

[30] A. K. MAZUR AND M. MAALOUM, *Atomic force microscopy study of DNA flexibility on short length scales: smooth bending versus kinking*, Nucleic Acids Res., 42 (2014), pp. 14006–14012.

[31] A. NOY AND R. GOLESTANIAN, *Length scale dependence of DNA mechanical properties*, Phys. Rev. Lett., 109 (2012), p. 228101.

[32] T. SHAFEE AND R. LOWE, *Eukaryotic and prokaryotic gene structure*. 2016.

[33] S. C. VERMA, Z. QIAN, AND S. L. ADHYA, *Architecture of the escherichia coli nucleoid*, PLoS Genet., 15 (2019), p. e1008456.

[34] J. LI, S. S. WIJERATNE, X. QIU, AND C.-H. KIANG, *DNA under force: Mechanics, electrostatics, and hydration*, Nanomaterials (Basel), 5 (2015), pp. 246–267.

[35] V. DAHIREL, F. PAILLUSSON, M. JARDAT, M. BARBI, AND J.-M. VICTOR, *Nonspecific DNA-protein interaction: why proteins can diffuse along DNA*, Phys. Rev. Lett., 102 (2009), p. 228101.

[36] J. J. FUNKE, P. KETTERER, C. LIELEG, S. SCHUNTER, P. KORBER, AND H. DIETZ, *Uncovering the forces between nucleosomes using DNA origami*, Sci Adv, 2 (2016), p. e1600974.

[37] J. KINDT, S. TZLIL, A. BEN-SHAUL, AND W. M. GELBART, *DNA packaging and ejection forces in bacteriophage*, Proc. Natl. Acad. Sci. U. S. A., 98 (2001), pp. 13671–13674.

[38] H. Y. WANG, T. ELSTON, A. MOGILNER, AND G. OSTER, *Force generation in RNA polymerase*, Biophys. J., 74 (1998), pp. 1186–1202.

[39] J. T. FINER, R. M. SIMMONS, AND J. A. SPUDICH, *Single myosin molecule mechanics: piconewton forces and nanometre steps*, Nature, 368 (1994), pp. 113–119.

[40] D. KELLER AND C. BUSTAMANTE, *The mechanochemistry of molecular motors*, Biophys. J., 78 (2000), pp. 541–556.

[41] L. D. MURPHY AND S. B. ZIMMERMAN, *Stabilization of compact spermidine nucleoids from escherichia coli under crowded conditions: implications for in vivo nucleoid structure*, J. Struct. Biol., 119 (1997), pp. 336–346.

[42] S. S. ALI, J. SOO, C. RAO, A. S. LEUNG, D. H.-M. NGAI, A. W. ENSMINGER, AND W. W. NAVARRE, *Silencing by H-NS potentiated the evolution of salmonella*, PLoS Pathog., 10 (2014), p. e1004500.

[43] S. B. ZIMMERMAN, *Shape and compaction of escherichia coli nucleoids*, J. Struct. Biol., 156 (2006), pp. 255–261.

[44] H. WANG, S. YEHOSHUA, S. S. ALI, W. W. NAVARRE, AND J. N. MILSTEIN, *A biomechanical mechanism for initiating DNA packaging*, Nucleic Acids Res., 42 (2014), pp. 11921–11927.

[45] I. N. OLEKHNOVICH AND R. J. KADNER, *Role of nucleoid-associated proteins hha and H-NS in expression of salmonella enterica activators HilD, HilC, and RtsA required for cell invasion*, J. Bacteriol., 189 (2007), pp. 6882–6890.

[46] J. GARCÍA, T. N. CORDEIRO, J. M. NIETO, I. PONS, A. JUÁREZ, AND M. PONS, *Interaction between the bacterial nucleoid associated proteins hha and H-NS involves a conformational change of hha*, Biochem. J, 388 (2005), pp. 755–762.

[47] C. MADRID, C. BALSALOBRE, J. GARCÍA, AND OTHERS, *The novel Hha/YmoA family of nucleoid-associated proteins: use of structural mimicry to modulate the activity of the H-NS family of proteins*, Molecular, (2007).

[48] S. PAYTUBI, C. MADRID, N. FORNS, J. M. NIETO, AND OTHERS, *YdgT, the hha paralogue in escherichia coli, forms heteromeric complexes with H-NS and StpA*, Molecular, (2004).

[49] S. S. ALI, J. C. WHITNEY, J. STEVENSON, H. ROBINSON, P. L. HOWELL, AND W. W. NAVARRE, *Structural insights into the regulation of foreign genes in salmonella by the Hha/H-NS complex*, J. Biol. Chem., 288 (2013), pp. 13356–13369.

[50] J. M. NIETO, C. MADRID, A. PRENAFETA, E. MIQUELAY, C. BALSALOBRE, M. CARRASCAL, AND A. JUÁREZ, *Expression of the hemolysin operon in escherichia coli is modulated by a nucleoid-protein complex that includes the proteins hha and H-NS*, Mol. Gen. Genet., 263 (2000), pp. 349–358.

[51] B. LANG, N. BLOT, E. BOUFFARTIGUES, M. BUCKLE, M. GEERTZ, C. O. GUALERZI, R. MAVATHUR, G. MUSKHELISHVILI, C. L. PON, S. RIMSKY, S. STELLA, M. M. BABU, AND A. TRAVERS, *High-affinity DNA binding sites for H-NS provide a molecular basis for selective silencing within proteobacterial genomes*, Nucleic Acids Res., 35 (2007), pp. 6330–6337.

[52] A. E. TUPPER, T. A. OWEN-HUGHES, D. W. USSERY, D. S. SANTOS, D. J. FERGUSON, J. M. SIDEBOTHAM, J. C. HINTON, AND C. F. HIGGINS, *The chromatin-associated protein H-NS alters DNA topology in vitro*, EMBO J., 13 (1994), pp. 258–268.

[53] C. J. DORMAN, *H-NS: a universal regulator for a dynamic genome*, Nat. Rev. Microbiol., 2 (2004), p. 391.

[54] J. R. C. VAN DER MAAREL, D. GUTTULA, V. ARLUISON, S. U. EGELHAAF, I. GRILLO, AND V. T. FORSYTH, *Structure of the H-NS-DNA nucleoprotein complex*, Soft Matter, 12 (2016), pp. 3636–3642.

[55] C. J. DORMAN, J. C. HINTON, AND A. FREE, *Domain organization and oligomerization among H-NS-like nucleoid-associated proteins in bacteria*, Trends Microbiol., 7 (1999), pp. 124–128.

[56] M. C. NOOM, W. W. NAVARRE, T. OSHIMA, G. J. L. WUITE, AND R. T. DAME, *H-NS promotes looped domain formation in the bacterial chromosome*, Curr. Biol., 17 (2007), pp. R913–4.

[57] W. W. NAVARRE, S. PORWOLLIK, Y. WANG, M. MCCLELLAND, H. ROSEN, S. J. LIBBY, AND F. C. FANG, *Selective silencing of foreign DNA with low GC content by the H-NS protein in salmonella*, Science, 313 (2006), pp. 236–238.

[58] T. OSHIMA, S. ISHIKAWA, K. KUROKAWA, H. AIBA, AND N. OGASAWARA, *Escherichia coli histone-like protein H-NS preferentially binds to horizontally acquired DNA in association with RNA polymerase*, DNA Res., 13 (2006), pp. 141–153.

[59] C. UEGUCHI AND T. MIZUNO, *The escherichia coli nucleoid protein H-NS functions directly as a transcriptional repressor*, EMBO J., 12 (1993), pp. 1039–1046.

[60] S. S. SINGH, N. SINGH, R. P. BONOCORA, D. M. FITZGERALD, J. T. WADE, AND D. C. GRAINGER, *Widespread suppression of intragenic transcription initiation by H-NS*, Genes Dev., 28 (2014), pp. 214–219.

[61] B. J. A. M. JORDI, A. E. FIELDER, C. M. BURNS, J. C. D. HINTON, N. DOVER, D. W. USSERY, AND C. F. HIGGINS, *DNA binding is not sufficient for H-NS-mediated repression ofprou expression*, J. Biol. Chem., 272 (1997), pp. 12083–12090.

[62] K. HIGASHI, T. TOBE, A. KANAI, E. UYAR, S. ISHIKAWA, Y. SUZUKI, N. OGASAWARA, K. KUROKAWA, AND T. OSHIMA, *H-NS facilitates sequence diversification of horizontally transferred DNAs during their integration in host chromosomes*, PLoS Genet., 12 (2016), p. e1005796.

[63] R. AMIT, A. B. OPPENHEIM, AND J. STAVANS, *Increased bending rigidity of single DNA molecules by H-NS, a temperature and osmolarity sensor*, Biophys. J., 84 (2003), pp. 2467–2473.

[64] S. LUCCHINI, G. ROWLEY, M. D. GOLDBERG, D. HURD, M. HARRISON, AND J. C. D. HINTON, *H-NS mediates the silencing of laterally acquired genes in bacteria*, PLoS Pathog., 2 (2006), p. e81.

[65] B. R. G. GORDON, Y. LI, A. COTE, M. T. WEIRAUCH, P. DING, T. R. HUGHES, W. W. NAVARRE, B. XIA, AND J. LIU, *Structural basis for recognition of AT-rich DNA by unrelated xenogeneic silencing proteins*, Proc. Natl. Acad. Sci. U. S. A., 108 (2011), pp. 10690–10695.

[66] M. DOETSCH, T. GSTREIN, R. SCHROEDER, AND B. FÜRTIG, *Mechanisms of StpA-mediated RNA remodeling*, RNA Biol., 7 (2010), pp. 735–743.

[67] S. T. AROLD, P. G. LEONARD, G. N. PARKINSON, AND J. E. LADBURY, *H-NS forms a superhelical protein scaffold for DNA condensation*, Proc. Natl. Acad. Sci. U. S. A., 107 (2010), pp. 15728–15732.

[68] W. W. NAVARRE, *H-NS as a defence system*, in Bacterial chromatin, Springer, 2010, pp. 251–322.

[69] C. J. DORMAN, *H-NS, the genome sentinel*, Nat. Rev. Microbiol., (2007).

[70] W. W. NAVARRE, M. MCCLELLAND, S. J. LIBBY, AND F. C. FANG, *Silencing of xenogeneic DNA by H-NS—facilitation of lateral gene transfer in bacteria by a defense system that recognizes foreign DNA*, Genes Dev., 21 (2007), pp. 1456–1471.

[71] M. A. PICKER AND H. J. WING, *H-NS, its family members and their regulation of virulence genes in shigella species*, Genes, 7 (2016).

[72] L. E. LAMBERTE, G. BANIULYTE, S. S. SINGH, A. M. STRINGER, R. P. BONOCORA, M. STRACY, A. N. KAPANIDIS, J. T. WADE, AND D. C. GRAINGER, *Horizontally acquired AT-rich genes in escherichia coli cause toxicity by sequestering RNA polymerase*, Nat Microbiol, 2 (2017), p. 16249.

[73] J. C. PEREZ, T. LATIFI, AND E. A. GROISMAN, *Overcoming H-NS-mediated transcriptional silencing of horizontally acquired genes by the PhoP and SlyA proteins in salmonella enterica*, J. Biol. Chem., 283 (2008), pp. 10773–10783.

[74] D. SLEDJESKI AND S. GOTTESMAN, *A small RNA acts as an antisilencer of the H-NS-silenced rcsa gene of escherichia coli*, Proc. Natl. Acad. Sci. U. S. A., 92 (1995), pp. 2003–2007.

[75] M. V. KOTLAJICH, D. R. HRON, B. A. BOUDREAU, Z. SUN, Y. L. LYUBCHENKO, AND R. LANDICK, *Bridged filaments of histone-like nucleoid structuring protein pause RNA polymerase and aid termination in bacteria*, Elife, 4 (2015).

[76] S. ONO, M. D. GOLDBERG, T. OLSSON, D. ESPOSITO, J. C. D. HINTON, AND J. E. LADBURY, *H-NS is a part of a thermally controlled mechanism for bacterial gene regulation*, Biochem. J, 391 (2005), pp. 203–213.

[77] J. M. NIETO, M. CARMONA, S. BOLLAND, Y. JUBETE, F. DE LA CRUZ, AND A. JUÁREZ, *The hha gene modulates haemolysin expression in escherichia coli*, Mol. Microbiol., 5 (1991), pp. 1285–1293.

[78] C. MADRID, J. M. NIETO, AND A. JUÁREZ, *Role of the Hha/YmoA family of proteins in the thermoregulation of the expression of virulence factors*, Int. J. Med. Microbiol., 291 (2002), pp. 425–432.

[79] G. R. CORNELIS, C. SLUITERS, I. DELOR, D. GEIB, AND K. KANIGA, *YmoA, a yersinia enterocolitica chromosomal gene modulating the expression of virulence functions*, Mol. Microbiol., 5 (1991), pp. 1023–1034.

[80] C. F. DE ALBA, C. SOLÓRZANO, S. PAYTUBI, C. MADRID, A. JUAREZ, J. GARCÍA, AND M. PONS, *Essential residues in the H-NS binding site of hha, a co-regulator of horizontally acquired genes in enterobacteria*, FEBS Lett., 585 (2011), pp. 1765–1770.

[81] D. M. STOEBEL, A. FREE, AND C. J. DORMAN, *Anti-silencing: overcoming H-NS-mediated repression of transcription in gram-negative enteric bacteria*, Microbiology, 154 (2008), pp. 2533–2545.

[82] R. C. Baños, A. Vivero, S. Aznar, J. García, M. Pons, C. Madrid, and A. Juárez, *Differential regulation of horizontally acquired and core genome genes by the bacterial modulator H-NS*, PLoS Genet., 5 (2009), p. e1000513.

[83] F. Hommais, E. Krin, C. Laurent-Winter, O. Soutourina, A. Malpertuy, J. P. Le Caer, A. Danchin, and P. Bertin, *Large-scale monitoring of pleiotropic regulation of gene expression by the prokaryotic nucleoid-associated protein, H-NS*, Mol. Microbiol., 40 (2001), pp. 20–36.

[84] R. Gulvady, Y. Gao, L. J. Kenney, and J. Yan, *A single molecule analysis of H-NS uncouples DNA binding affinity from DNA specificity*, Nucleic Acids Res., 46 (2018), pp. 10216–10224.

[85] E. Riccardi, E. C. van Mastbergen, W. W. Navarre, and J. Vreede, *Predicting the mechanism and rate of H-NS binding to AT-rich DNA*, PLoS Comput. Biol., 15 (2019), p. e1006845.

[86] M. Sette, R. Spurio, E. Trotta, C. Brandizi, A. Brandi, C. L. Pon, G. Barbato, R. Boelens, and C. O. Gualerzi, *Sequence-specific recognition of DNA by the c-terminal domain of nucleoid-associated protein H-NS*, J. Biol. Chem., 284 (2009), pp. 30453–30462.

[87] C. Badaut, R. Williams, V. Arluison, E. Bouffartigues, B. Robert, H. Buc, and S. Rimsky, *The degree of oligomerization of the H-NS nucleoid structuring protein is related to specific binding to DNA*, J. Biol. Chem., 277 (2002), pp. 41657–41666.

[88] R. Spurio, M. Falconi, A. Brandi, C. L. Pon, and C. O. Gualerzi, *The oligomeric structure of nucleoid protein H-NS is necessary for recognition of intrinsically curved DNA and for DNA bending*, EMBO J., 16 (1997), pp. 1795–1805.

[89] D. S. Goodsell and R. E. Dickerson, *Bending and curvature calculations in B-DNA*, Nucleic Acids Res., 22 (1994), pp. 5497–5503.

[90] J. L. Leroy, E. Charretier, M. Kochoyan, and M. Guéron, *Evidence from base-pair kinetics for two types of adenine tract structures in solution: their relation to DNA curvature*, Biochemistry, 27 (1988), pp. 8894–8898.

[91] C. Ueguchi, T. Suzuki, T. Yoshida, K. Tanaka, and T. Mizuno, *Systematic mutational analysis revealing the functional domain organization of escherichia coli nucleoid protein H-NS*, J. Mol. Biol., 263 (1996), pp. 149–162.

[92] Y. Liu, H. Chen, L. J. Kenney, and J. Yan, *A divalent switch drives H-NS/DNA-binding conformations between stiffening and bridging modes*, Genes Dev., 24 (2010), pp. 339–344.

[93] R. A. VAN DER VALK, J. VREEDE, L. QIN, G. F. MOOLENAAR, A. HOFMANN, N. GOOSEN, AND R. T. DAME, *Mechanism of environmentally driven conformational changes that modulate H-NS DNA-bridging activity*, Elife, 6 (2017).

[94] R. CUKIER-KAHN, M. JACQUET, AND F. GROS, *Two heat-resistant, low molecular weight proteins from escherichia coli that stimulate DNA-directed RNA synthesis*, Proc. Natl. Acad. Sci. U. S. A., 69 (1972), pp. 3643–3647.

[95] C. J. LIM, Y. R. WHANG, L. J. KENNEY, AND J. YAN, *Gene silencing H-NS paralogue StpA forms a rigid protein filament along DNA that blocks DNA accessibility*, Nucleic Acids Res., 40 (2012), pp. 3316–3328.

[96] A. ZHANG AND M. BELFORT, *Nucleotide sequence of a newly-identified escherichia coli gene, stpa, encoding an H-NS-like protein*, Nucleic Acids Res., 20 (1992), p. 6735.

[97] A. ZHANG, S. RIMSKY, M. E. REABAN, H. BUC, AND M. BELFORT, *Escherichia coli protein analogs StpA and H-NS: regulatory loops, similar and disparate effects on nucleic acid dynamics*, EMBO J., 15 (1996), pp. 1340–1349.

[98] M. Á. DE LA CRUZ, M. FERNÁNDEZ-MORA, C. GUADARRAMA, M. A. FLORES-VALDEZ, V. H. BUSTAMANTE, A. VÁZQUEZ, AND E. CALVA, *LeuO antagonizes H-NS and StpA-dependent repression in salmonella enterica omps1*, Mol. Microbiol., 66 (2007), pp. 727–743.

[99] C. M. MÜLLER, U. DOBRINDT, G. NAGY, L. EMÖDY, B. E. UHLIN, AND J. HACKER, *Role of histone-like proteins H-NS and StpA in expression of virulence determinants of uropathogenic escherichia coli*, J. Bacteriol., 188 (2006), pp. 5428–5438.

[100] P. G. LEONARD, S. ONO, J. GOR, S. J. PERKINS, AND J. E. LADBURY, *Investigation of the self-association and hetero-association interactions of H-NS and StpA from enterobacteria*, Mol. Microbiol., 73 (2009), pp. 165–179.

[101] S. LUCCHINI, P. MCDERMOTT, A. THOMPSON, AND J. C. D. HINTON, *The H-NS-like protein StpA represses the RpoS (sigma 38) regulon during exponential growth of salmonella typhimurium*, Mol. Microbiol., 74 (2009), pp. 1169–1186.

[102] B. A. BOUDREAU, D. R. HRON, L. QIN, R. A. VAN DER VALK, M. V. KOTLAJICH, R. T. DAME, AND R. LANDICK, *StpA and hha stimulate pausing by RNA polymerase by promoting DNA-DNA bridging of H-NS filaments*, Nucleic Acids Res., 46 (2018), pp. 5525–5546.

[103] C. WALDSICH, R. GROSSBERGER, AND R. SCHROEDER, *RNA chaperone StpA loosens interactions of the tertiary structure in the td group I intron in vivo*, Genes Dev., 16 (2002), pp. 2300–2312.

[104] P. DEIGHAN, A. FREE, AND C. J. DORMAN, *A role for the escherichia coli H-NS-like protein StpA in OmpF porin expression through modulation of micf RNA stability*, Mol. Microbiol., 38 (2000), pp. 126–139.

[105] A. ZHANG, V. DERBYSHIRE, J. L. SALVO, AND M. BELFORT, *Escherichia coli protein StpA stimulates self-splicing by promoting RNA assembly in vitro*, RNA, 1 (1995), pp. 783–793.

[106] O. MAYER, L. RAJKOWITSCH, C. LORENZ, R. KONRAT, AND R. SCHROEDER, *RNA chaperone activity and RNA-binding properties of the e. coli protein StpA*, Nucleic Acids Res., 35 (2007), pp. 1257–1269.

[107] J. M. SONNENFIELD, C. M. BURNS, C. F. HIGGINS, AND J. C. HINTON, *The nucleoid-associated protein StpA binds curved DNA, has a greater DNA-binding affinity than H-NS and is present in significant levels in hns mutants*, Biochimie, 83 (2001), pp. 243–249.

[108] A. FREE, R. M. WILLIAMS, AND C. J. DORMAN, *The StpA protein functions as a molecular adapter to mediate repression of the bgl operon by truncated H-NS in escherichia coli*, J. Bacteriol., 180 (1998), pp. 994–997.

[109] B. SONDEN AND B. E. UHLIN, *Coordinated and differential expression of histone-like proteins in escherichia coli: regulation and function of the H-NS analog StpA*, EMBO J., 15 (1996), pp. 4970–4980.

[110] A. TRAVERS, *DNA-protein interactions: IHF–the master bender*, Curr. Biol., 7 (1997), pp. R252–4.

[111] S. W. YANG AND H. A. NASH, *Comparison of protein binding to DNA in vivo and in vitro: defining an effective intracellular target*, EMBO J., 14 (1995), pp. 6292–6300.

[112] L. M. HALES, R. I. GUMPORT, AND J. F. GARDNER, *Determining the DNA sequence elements required for binding integration host factor to two different target sites*, J. Bacteriol., 176 (1994), pp. 2999–3006.

[113] P. A. RICE, S. YANG, K. MIZUUCHI, AND H. A. NASH, *Crystal structure of an IHF-DNA complex: a protein-induced DNA u-turn*, Cell, 87 (1996), pp. 1295–1306.

[114] D. FRENKIEL-KRISPIN, S. LEVIN-ZAIDMAN, E. SHIMONI, S. G. WOLF, E. J. WACHTEL, T. ARAD, S. E. FINKEL, R. KOLTER, AND A. MINSKY, *Regulated phase transitions of bacterial chromatin: a non-enzymatic pathway for generic DNA protection*, EMBO J., 20 (2001), pp. 1184–1191.

[115] T. Sarkar, A. S. Petrov, J. R. Vitko, C. T. Santai, S. C. Harvey, I. Mukerji, and N. V. Hud, *Integration host factor (IHF) dictates the structure of polyamine-DNA condensates: implications for the role of IHF in the compaction of bacterial chromatin*, Biochemistry, 48 (2009), pp. 667–675.

[116] B. M. Ali, R. Amit, I. Braslavsky, A. B. Oppenheim, O. Gileadi, and J. Stavans, *Compaction of single DNA molecules induced by binding of integration host factor (IHF)*, Proc. Natl. Acad. Sci. U. S. A., 98 (2001), pp. 10658–10663.

[117] J. E. Grimwade, V. T. Ryan, and A. C. Leonard, *IHF redistributes bound initiator protein, DnaA, on supercoiled oric of escherichia coli*, Mol. Microbiol., 35 (2000), pp. 835–844.

[118] V. T. Ryan, J. E. Grimwade, C. J. Nievera, and A. C. Leonard, *IHF and HU stimulate assembly of pre-replication complexes at escherichia coli oric by two different mechanisms*, Mol. Microbiol., 46 (2002), pp. 113–124.

[119] A. V. Wright, J.-J. Liu, G. J. Knott, K. W. Doxzen, E. Nogales, and J. A. Doudna, *Structures of the CRISPR genome integration complex*, Science, 357 (2017), pp. 1113–1118.

[120] J. Lin, H. Chen, P. Dröge, and J. Yan, *Physical organization of DNA by multiple non-specific DNA-binding modes of integration host factor (IHF)*, PLoS One, 7 (2012), p. e49885.

[121] W. Wang, G.-W. Li, C. Chen, X. S. Xie, and X. Zhuang, *Chromosome organization by a nucleoid-associated protein in live bacteria*, Science, 333 (2011), pp. 1445–1449.

[122] L. A. Novotny, A. O. Amer, M. E. Brockson, S. D. Goodman, and L. O. Bakaletz, *Structural stability of burkholderia cenocepacia biofilms is reliant on eDNA structure and presence of a bacterial nucleic acid binding protein*, PLoS One, 8 (2013), p. e67629.

[123] T. Das, S. Sehar, and M. Manefield, *The roles of extracellular DNA in the structural integrity of extracellular polymeric substance and bacterial biofilm development*, Environ. Microbiol. Rep., 5 (2013), pp. 778–786.

[124] A. L. Spoering and M. S. Gilmore, *Quorum sensing and DNA release in bacterial biofilms*, Curr. Opin. Microbiol., 9 (2006), pp. 133–137.

[125] N. S. Jakubovics, R. C. Shields, N. Rajarajan, and J. G. Burgess, *Life after death: the critical role of extracellular DNA in microbial biofilms*, Lett. Appl. Microbiol., 57 (2013), pp. 467–475.

[126] C. B. WHITCHURCH, T. TOLKER-NIELSEN, P. C. RAGAS, AND J. S. MATTICK, *Extracellular DNA required for bacterial biofilm formation*, Science, 295 (2002), p. 1487.

[127] L. MONTANARO, A. POGGI, L. VISAI, S. RAVAIOLI, D. CAMPOCCIA, P. SPEZIALE, AND C. R. ARCIOLA, *Extracellular DNA in biofilms*, Int. J. Artif. Organs, 34 (2011), pp. 824–831.

[128] M. CONNOLLY, A. ARRA, V. ZVODA, P. J. STEINBACH, P. A. RICE, AND A. ANSARI, *Static kinks or flexible hinges: Multiple conformations of bent DNA bound to integration host factor revealed by fluorescence lifetime measurements*, J. Phys. Chem. B, 122 (2018), pp. 11519–11534.

[129] A. R. CARTER, Y. SEOL, AND T. T. PERKINS, *Precision surface-coupled optical-trapping assay with one-basepair resolution*, Biophys. J., 96 (2009), pp. 2926–2934.

[130] M. FOQUET, J. KORLACH, W. ZIPFEL, W. W. WEBB, AND H. G. CRAIGHEAD, *DNA fragment sizing by single molecule detection in submicrometer-sized closed fluidic channels*, Anal. Chem., 74 (2002), pp. 1415–1422.

[131] J. DAI, T. ITO, L. SUN, AND R. M. CROOKS, *Electrokinetic trapping and concentration enrichment of DNA in a microfluidic channel*, J. Am. Chem. Soc., 125 (2003), pp. 13026–13027.

[132] ENZOKLOP, *Polymerase chain reaction.*
https://commons.wikimedia.org/wiki/File:Polymerase_chain_reaction.svg, Apr. 2014.
Accessed: 2019-12-1.

[133] U. PIRAN AND W. J. RIORDAN, *Dissociation rate constant of the biotin-streptavidin complex*, J. Immunol. Methods, 133 (1990), pp. 141–143.

[134] O. H. LAITINEN, V. P. HYTÖNEN, H. R. NORDLUND, AND M. S. KULOMAA, *Genetically engineered avidins and streptavidins*, Cell. Mol. Life Sci., 63 (2006), pp. 2992–3017.

[135] D. A. SCHAFER, J. GELLES, M. P. SHEETZ, AND R. LANDICK, *Transcription by single molecules of RNA polymerase observed by light microscopy*, Nature, 352 (1991), pp. 444–448.

[136] H. YIN, R. LANDICK, AND J. GELLES, *Tethered particle motion method for studying transcript elongation by a single RNA polymerase molecule*, Biophys. J., 67 (1994), pp. 2468–2478.

[137] J. GELLES, B. J. SCHNAPP, AND M. P. SHEETZ, *Tracking kinesin-driven movements with nanometre-scale precision*, Nature, 331 (1988), pp. 450–453.

[138] D. E. SEGALL, P. C. NELSON, AND R. PHILLIPS, *Volume-exclusion effects in tethered-particle experiments: bead size matters*, Phys. Rev. Lett., 96 (2006), p. 088306.

[139] S. BRINKERS, H. R. C. DIETRICH, F. H. DE GROOTE, I. T. YOUNG, AND B. RIEGER, *The persistence length of double stranded DNA determined using dark field tethered particle motion*, J. Chem. Phys., 130 (2009), p. 215105.

[140] J. N. M. PINKNEY, P. ZAWADZKI, J. MAZURYK, L. K. ARCISZEWSKA, D. J. SHERRATT, AND A. N. KAPANIDIS, *Capturing reaction paths and intermediates in Cre-loxP recombination using single-molecule fluorescence*, Proc. Natl. Acad. Sci. U. S. A., 109 (2012), pp. 20871–20876.

[141] P. F. J. MAY, J. N. M. PINKNEY, P. ZAWADZKI, G. W. EVANS, D. J. SHERRATT, AND A. N. KAPANIDIS, *Tethered fluorophore motion: studying large DNA conformational changes by single-fluorophore imaging*, Biophys. J., 107 (2014), pp. 1205–1216.

[142] N. POUGET, C. DENNIS, C. TURLAN, M. GRIGORIEV, M. CHANDLER, AND L. SALOMÉ, *Single-particle tracking for DNA tether length monitoring*, Nucleic Acids Res., 32 (2004), p. e73.

[143] P. C. NELSON, C. ZURLA, D. BROGIOLI, J. F. BEAUSANG, L. FINZI, AND D. DUNLAP, *Tethered particle motion as a diagnostic of DNA tether length*, J. Phys. Chem. B, 110 (2006), pp. 17260–17267.

[144] K. HALVORSEN AND W. P. WONG, *Massively parallel single-molecule manipulation using centrifugal force*, Biophys. J., 98 (2010), pp. L53–5.

[145] D. YANG, A. WARD, K. HALVORSEN, AND W. P. WONG, *Multiplexed single-molecule force spectroscopy using a centrifuge*, Nat. Commun., 7 (2016), p. 11026.

[146] A. ASHKIN, *Acceleration and trapping of particles by radiation pressure*, Phys. Rev. Lett., (1970).

[147] A. ASHKIN, J. M. DZIEDZIC, J. E. BJORKHOLM, AND S. CHU, *Observation of a single-beam gradient force optical trap for dielectric particles*, Opt. Lett., 11 (1986), p. 288.

[148] A. B. STILGOE, T. A. NIEMINEN, G. KNÖENER, N. R. HECKENBERG, AND H. RUBINSZTEIN-DUNLOP, *The effect of mie resonances on trapping in optical tweezers*, Opt. Express, 16 (2008), pp. 15039–15051.

[149] K. DHOLAKIA, P. REECE, AND M. GU, *Optical micromanipulation*, Chem. Soc. Rev., 37 (2008), pp. 42–55.

[150] W. J. GREENLEAF, M. T. WOODSIDE, E. A. ABBONDANZIERI, AND S. M. BLOCK, *Passive all-optical force clamp for high-resolution laser trapping*, Phys. Rev. Lett., 95 (2005), p. 208102.

[151] F. GITTES AND C. F. SCHMIDT, *Interference model for back-focal-plane displacement detection in optical tweezers*, Opt. Lett., 23 (1998), pp. 7–9.

[152] K. BERG-SØRENSEN, E. J. G. PETERMAN, T. WEBER, C. F. SCHMIDT, AND H. FLYVBJERG, *Power spectrum analysis for optical tweezers. II: Laser wavelength dependence of parasitic filtering, and how to achieve high bandwidth*, Rev. Sci. Instrum., 77 (2006), p. 063106.

[153] K. BERG-SØRENSEN AND H. FLYVBJERG, *Power spectrum analysis for optical tweezers*, Rev. Sci. Instrum., 75 (2004), pp. 594–612.

[154] G. M. GIBSON, J. LEACH, S. KEEN, A. J. WRIGHT, AND M. J. PADGETT, *Measuring the accuracy of particle position and force in optical tweezers using high-speed video microscopy*, Opt. Express, 16 (2008), pp. 14561–14570.

[155] G. BINNIG, C. F. QUATE, AND C. GERBER, *Atomic force microscope*, Phys. Rev. Lett., 56 (1986), pp. 930–933.

[156] Y. F. DUFRÊNE, *Atomic force microscopy in microbiology: new structural and functional insights into the microbial cell surface*, MBio, 5 (2014), pp. e01363–14.

[157] H. ASAKAWA, K. IKEGAMI, M. SETOU, N. WATANABE, M. TSUKADA, AND T. FUKUMA, *Submolecular-scale imaging of α-helices and c-terminal domains of tubulins by frequency modulation atomic force microscopy in liquid*, Biophys. J., 101 (2011), pp. 1270–1276.

[158] A. PYNE, R. THOMPSON, C. LEUNG, D. ROY, AND B. W. HOOGENBOOM, *Single-molecule reconstruction of oligonucleotide secondary structure by atomic force microscopy*, Small, 10 (2014), pp. 3257–3261.

[159] Y. LYUBCHENKO, L. SHLYAKHTENKO, R. HARRINGTON, P. ODEN, AND S. LINDSAY, *Atomic force microscopy of long DNA: imaging in air and under water*, Proc. Natl. Acad. Sci. U. S. A., 90 (1993), pp. 2137–2140.

[160] M. GRANDBOIS, M. BEYER, M. RIEF, H. CLAUSEN-SCHAUMANN, AND H. E. GAUB, *How strong is a covalent bond?*, Science, 283 (1999), pp. 1727–1730.

[161] F. OESTERHELT, D. OESTERHELT, M. PFEIFFER, A. ENGEL, H. E. GAUB, AND D. J. MÜLLER, *Unfolding pathways of individual bacteriorhodopsins*, Science, 288 (2000), pp. 143–146.

[162] J. M. Kim, T. Ohtani, J. Y. Park, S. M. Chang, and H. Muramatsu, *DC electric-field-induced DNA stretching for AFM and SNOM studies*, Ultramicroscopy, 91 (2002), pp. 139–149.

[163] M. Chen, M. Li, C. L. Brosseau, and J. Lipkowski, *AFM studies of the effect of temperature and electric field on the structure of a DMPC-cholesterol bilayer supported on a au (111) electrode surface*, Langmuir, 25 (2008), pp. 1028–1037.

[164] L. J. C. Jeuken, *AFM study on the electric-field effects on supported bilayer lipid membranes*, Biophys. J., 94 (2008), pp. 4711–4717.

[165] E. M. Puchner and H. E. Gaub, *Force and function: probing proteins with AFM-based force spectroscopy*, Curr. Opin. Struct. Biol., 19 (2009), pp. 605–614.

[166] T. Hugel and M. Seitz, *The study of molecular interactions by AFM force spectroscopy*, Macromol. Rapid Commun., 22 (2001), pp. 989–1016.

[167] S. Tasharrofi, S. S. Hassani, and Z. Sobat, *Encyclopedia of Nanotechnology*, May 2015.

[168] F. G. A. Faas, B. Rieger, L. J. van Vliet, and D. I. Cherny, *DNA deformations near charged surfaces: electron and atomic force microscopy views*, Biophys. J., 97 (2009), pp. 1148–1157.

[169] M. Bussiek, N. Mücke, and J. Langowski, *Polylysine-coated mica can be used to observe systematic changes in the supercoiled DNA conformation by scanning force microscopy in solution*, Nucleic Acids Res., 31 (2003), p. e137.

[170] L. S. Shlyakhtenko, A. A. Gall, and Y. L. Lyubchenko, *Mica functionalization for imaging of DNA and protein-DNA complexes with atomic force microscopy*, Methods Mol. Biol., 931 (2013), pp. 295–312.

[171] L. S. Shlyakhtenko, A. A. Gall, J. J. Weimer, D. D. Hawn, and Y. L. Lyubchenko, *Atomic force microscopy imaging of DNA covalently immobilized on a functionalized mica substrate*, Biophys. J., 77 (1999), pp. 568–576.

[172] M. Tanigawa and T. Okada, *Atomic force microscopy of supercoiled DNA structure on mica*, Anal. Chim. Acta, 365 (1998), pp. 19–25.

[173] L. T. Costa, J. R. Pinto, M. B. Moraes, G. G. B. de Souza, M. M. Sorenson, P. M. Bisch, and G. Weissmüller, *Chemical treatment of mica for atomic force microscopy can affect biological sample conformation*, Biophys. Chem., 109 (2004), pp. 63–71.

[174] Y. L. Lyubchenko, A. A. Gall, and L. S. Shlyakhtenko, *Atomic force microscopy of DNA and protein-DNA complexes using functionalized mica substrates*, Methods Mol. Biol., 148 (2001), pp. 569–578.

[175] A. A. Bukharaev, N. V. Berdunov, D. V. Ovchinnikov, and K. M. Salikhov, *Three-dimensional probe and surface reconstruction for atomic force microscopy using a deconvolution algorithm*, In Pract., 5 (1998), p. 21.

[176] P. Markiewicz and M. C. Goh, *Atomic force microscopy probe tip visualization and improvement of images using a simple deconvolution procedure*, Langmuir, 10 (1994), pp. 5–7.

[177] ———, *Atomic force microscope tip deconvolution using calibration arrays*, Rev. Sci. Instrum., 66 (1995), pp. 3186–3190.

[178] C. K. P. Loong, H.-X. Zhou, and P. B. Chase, *Persistence length of human cardiac α-tropomyosin measured by single molecule direct probe microscopy*, PLoS One, 7 (2012), p. e39676.

[179] E. J. Miller, W. Trewby, A. Farokh Payam, L. Piantanida, C. Cafolla, and K. Voïtchovsky, *Sub-nanometer resolution imaging with amplitude-modulation atomic force microscopy in liquid*, J. Vis. Exp., (2016).

[180] H. G. Hansma, M. Bezanilla, F. Zenhausern, M. Adrian, and R. L. Sinsheimer, *Atomic force microscopy of DNA in aqueous solutions*, Nucleic Acids Res., 21 (1993), pp. 505–512.

[181] F. Moreno-Herrero, J. Colchero, and A. M. Baró, *DNA height in scanning force microscopy*, Ultramicroscopy, 96 (2003), pp. 167–174.

[182] S. Santos, V. Barcons, H. K. Christenson, J. Font, and N. H. Thomson, *The intrinsic resolution limit in the atomic force microscope: implications for heights of nano-scale features*, PLoS One, 6 (2011), p. e23821.

[183] D. Kiracofe and A. Raman, *On eigenmodes, stiffness, and sensitivity of atomic force microscope cantilevers in air versus liquids*, J. Appl. Phys., 107 (2010), p. 033506.

[184] K. Voïtchovsky, *Anharmonicity, solvation forces, and resolution in atomic force microscopy at the solid-liquid interface*, Phys. Rev. E Stat. Nonlin. Soft Matter Phys., 88 (2013), p. 022407.

[185] K. Voïtchovsky, J. J. Kuna, S. A. Contera, E. Tosatti, and F. Stellacci, *Direct mapping of the solid–liquid adhesion energy with subnanometre resolution*, Nat. Nanotechnol., 5 (2010), pp. 401–405.

[186] A. San Paulo and R. García, *High-resolution imaging of antibodies by tapping-mode atomic force microscopy: attractive and repulsive tip-sample interaction regimes*, Biophys. J., 78 (2000), pp. 1599–1605.

[187] F. S. RUGGERI, J. HABCHI, A. CERRETA, AND G. DIETLER, *AFM-Based single molecule techniques: Unraveling the amyloid pathogenic species*, Curr. Pharm. Des., 22 (2016), pp. 3950–3970.

[188] H. J BUTT AND M. JASCHKE, *Calculation of thermal noise in atomic force microscopy*, Nanotechnology, 6 (1999), p. 1.

[189] T. E. SCHÄFFER, *Calculation of thermal noise in an atomic force microscope with a finite optical spot size*, Nanotechnology, 16 (2005), p. 664.

[190] Y. GAN, *Atomic and subnanometer resolution in ambient conditions by atomic force microscopy*, Surf. Sci. Rep., 64 (2009), pp. 99–121.

[191] G. SHANG, X. QIU, C. WANG, AND C. BAI, *Analysis of lateral force contribution to the topography in contact mode AFM*, Appl. Phys. A: Mater. Sci. Process., 66 (1998).

[192] F. J. GIESSIBL, *Advances in atomic force microscopy*, Rev. Mod. Phys., 75 (2003), pp. 949–983.

[193] A. M. SWEETMAN, S. P. JARVIS, H. SANG, I. LEKKAS, P. RAHE, Y. WANG, J. WANG, N. R. CHAMPNESS, L. KANTOROVICH, AND P. MORIARTY, *Mapping the force field of a hydrogen-bonded assembly*, Nat. Commun., 5 (2014), p. 3931.

[194] Q. ZHONG, D. INNISS, K. KJOLLER, AND V. B. ELINGS, *Fractured polymer/silica fiber surface studied by tapping mode atomic force microscopy*, Surface Science Letters, 290 (1993), p. L688.

[195] P. K. HANSMA, J. P. CLEVELAND, M. RADMACHER, D. A. WALTERS, P. E. HILLNER, M. BEZANILLA, M. FRITZ, D. VIE, H. G. HANSMA, C. B. PRATER, J. MASSIE, L. FUKUNAGA, J. GURLEY, AND V. ELINGS, *Tapping mode atomic force microscopy in liquids*, Appl. Phys. Lett., 64 (1994), pp. 1738–1740.

[196] L. LIU, N. XI, G. LI, AND H. CHEN, *Chapter 4 - atomic force Microscope-Based nanorobotic system for nanoassembly*, in Nano Optoelectronic Sensors and Devices, N. Xi and K. W. C. Lai, eds., William Andrew Publishing, Oxford, Jan. 2012, pp. 51–79.

[197] O. HANSEN AND A. BOISEN, *Noise in piezoresistive atomic force microscopy*, Nanotechnology, 10 (1999), pp. 51–60.

[198] M. HROUZEK, *Feedback control in an atomic force microscope used as a Nano-Manipulator*, Czech Technical University in Prague Acta Polytechnica, 45 (2005).

[199] M. A. VAN DIJK, L. C. KAPITEIN, J. VAN MAMEREN, C. F. SCHMIDT, AND E. J. G. PETERMAN, *Combining optical trapping and single-molecule fluorescence spectroscopy: enhanced photobleaching of fluorophores*, J. Phys. Chem. B, 108 (2004), pp. 6479–6484.

[200] B. XIAO, H. ZHANG, R. C. JOHNSON, AND J. F. MARKO, *Force-driven unbinding of proteins HU and fis from DNA quantified using a thermodynamic maxwell relation*, Nucleic Acids Res., 39 (2011), pp. 5568–5577.

[201] H. R. C. DIETRICH, B. RIEGER, F. G. M. WIERTZ, F. H. DE GROOTE, H. A. HEERING, I. T. YOUNG, AND Y. GARINI, *Tethered particle motion mediated by scattering from gold nanoparticles and darkfield microscopy*, J. Nurse Pract., 3 (2009), p. 031795.

[202] M. LINDNER, G. NIR, S. MEDALION, H. R. C. DIETRICH, Y. RABIN, AND Y. GARINI, *Force-free measurements of the conformations of DNA molecules tethered to a wall*, Phys. Rev. E Stat. Nonlin. Soft Matter Phys., 83 (2011), p. 011916.

[203] S. BLUMBERG, A. GAJRAJ, M. W. PENNINGTON, AND J.-C. MEINERS, *Three-dimensional characterization of tethered microspheres by total internal reflection fluorescence microscopy*, Biophys. J., 89 (2005), pp. 1272–1281.

[204] F. HAJIZADEH AND S. N. S. REIHANI, *Optimized optical trapping of gold nanoparticles*, Opt. Express, 18 (2010), pp. 551–559.

[205] O. SCHOLDER, *scholi/pySPM v0.2.20*, Apr. 2019.

[206] N. OTSU, *A threshold selection method from gray-level histograms*, IEEE Trans. Syst. Man Cybern., 9 (1979), pp. 62–66.

[207] T. Y. ZHANG AND Y. SUENC, *A fast parallel algorithm for thinning digital patterns*, Commun. ACM, (1984).

[208] C. RIVETTI, M. GUTHOLD, AND C. BUSTAMANTE, *Scanning force microscopy of DNA deposited onto mica: equilibration versus kinetic trapping studied by statistical polymer chain analysis*, J. Mol. Biol., 264 (1996), pp. 919–932.

[209] D. W. SCOTT, *On optimal and data-based histograms*, Biometrika, 66 (1979), pp. 605–610.

[210] R. T. DAME, J. VAN MAMEREN, M. S. LUIJSTERBURG, M. E. MYSIAK, A. JANIĆIJEVIĆ, G. PAZDZIOR, P. C. VAN DER VLIET, C. WYMAN, AND G. J. L. WUITE, *Analysis of scanning force microscopy images of protein-induced DNA bending using simulations*, Nucleic Acids Res., 33 (2005), p. e68.

[211] S. M. RAPPAPORT, S. MEDALION, AND Y. RABIN, *Curvature distribution of worm-like chains in two and three dimensions*, (2008).

[212] G. H. SEONG, E. KOBATAKE, K. MIURA, A. NAKAZAWA, AND M. AIZAWA, *Direct atomic force microscopy visualization of integration host factor-induced DNA bending structure of the promoter regulatory region on the pseudomonas TOL plasmid*, Biochem. Biophys. Res. Commun., 291 (2002), pp. 361–366.

[213] A. L. B. PYNE, A. NOY, K. MAIN, V. VELASCO-BERRELLEZA, M. M. PIPER-AKIS, L. A. MITCHENALL, F. M. CUGLIANDOLO, J. G. BETON, C. E. M. STEVENSON, B. W. HOOGENBOOM, A. D. BATES, A. MAXWELL, AND S. A. HARRIS, *Combining high-resolution AFM with MD simulations shows that DNA supercoiling induces kinks and defects that enhance flexibility and recognition*.
Dec. 2019.

[214] S. VAN DER WALT, J. L. SCHÖNBERGER, J. NUNEZ-IGLESIAS, F. BOULOGNE, J. D. WARNER, N. YAGER, E. GOUILLART, T. YU, AND SCIKIT-IMAGE CONTRIBUTORS, *scikit-image: image processing in python*, PeerJ, 2 (2014), p. e453.

[215] S. V. KUZNETSOV, S. SUGIMURA, P. VIVAS, D. M. CROTHERS, AND A. ANSARI, *Direct observation of DNA bending/unbending kinetics in complex with DNA-bending protein IHF*, Proc. Natl. Acad. Sci. U. S. A., 103 (2006), pp. 18515–18520.

[216] A. L. IBÁÑEZ DE ALDECOA, O. ZAFRA, AND J. E. GONZÁLEZ-PASTOR, *Mechanisms and regulation of extracellular DNA release and its biological roles in microbial communities*, Front. Microbiol., 8 (2017), p. 1390.

[217] O. ZAFRA, M. LAMPRECHT-GRANDÍO, C. G. DE FIGUERAS, AND J. E. GONZÁLEZ-PASTOR, *Extracellular DNA release by undomesticated bacillus subtilis is regulated by early competence*, PLoS One, 7 (2012), p. e48716.

[218] F. LANKAS, R. LAVERY, AND J. H. MADDOCKS, *Kinking occurs during molecular dynamics simulations of small DNA minicircles*, Structure, 14 (2006), pp. 1527–1534.

[219] S. YEHOSHUA, R. POLLARI, AND J. N. MILSTEIN, *Axial optical traps: A new direction for optical tweezers*, Biophys. J., 108 (2015), pp. 2759–2766.

[220] E. SCHÄFFER, S. F. NØRRELYKKE, AND J. HOWARD, *Surface forces and drag coefficients of microspheres near a plane surface measured with optical tweezers*, Langmuir, 23 (2007), pp. 3654–3665.

[221] T. Fazio, M.-L. Visnapuu, S. Wind, and E. C. Greene, *DNA curtains and nanoscale curtain rods: high-throughput tools for single molecule imaging*, Langmuir, 24 (2008), pp. 10524–10531.

[222] K. C. Neuman, E. A. Abbondanzieri, and S. M. Block, *Measurement of the effective focal shift in an optical trap*, Opt. Lett., 30 (2005), pp. 1318–1320.

[223] A. H. Mack, D. J. Schlingman, L. Regan, and S. G. J. Mochrie, *Practical axial optical trapping*, Rev. Sci. Instrum., 83 (2012), p. 103106.

[224] Y.-F. Chen, G. A. Blab, and J.-C. Meiners, *Stretching submicron biomolecules with constant-force axial optical tweezers*, Biophys. J., 96 (2009), pp. 4701–4708.

[225] S. Nawaz, P. Sánchez, K. Bodensiek, S. Li, M. Simons, and I. A. T. Schaap, *Cell visco-elasticity measured with AFM and optical trapping at sub-micrometer deformations*, PLoS One, 7 (2012), p. e45297.

[226] F. Pierini, K. Zembrzycki, P. Nakielski, S. Pawłowska, and T. A. Kowalewski, *Atomic force microscopy combined with optical tweezers (AFM/OT)*, Meas. Sci. Technol., 27 (2016), p. 025904.

[227] J. Huisstede, K. van der Werf, M. Bennink, and V. Subramaniam, *Force detection in optical tweezers using backscattered light*, Opt. Express, 13 (2005), pp. 1113–1123.

[228] A. Freise and K. Strain, *Interferometer techniques for Gravitational-Wave detection*, Living Rev. Relativ., 13 (2010), p. 1.

[229] R. R. Brau, P. B. Tarsa, J. M. Ferrer, P. Lee, and M. J. Lang, *Interlaced optical force-fluorescence measurements for single molecule biophysics*, Biophys. J., 91 (2006), pp. 1069–1077.

[230] H. Shen, E. Huang, T. Das, H. Xu, M. Ellisman, and Z. Liu, *TIRF microscopy with ultra-short penetration depth*, Opt. Express, 22 (2014), pp. 10728–10734.

[231] T. Ando, *High-speed atomic force microscopy and its future prospects*, Biophys. Rev., 10 (2018), pp. 285–292.

[232] R. T. Dame and N. Goosen, *HU: promoting or counteracting DNA compaction?*, FEBS Lett., 529 (2002), pp. 151–156.

[233] S. Le, H. Chen, P. Cong, J. Lin, P. Dröge, and J. Yan, *Mechanosensing of DNA bending in a single specific protein-DNA complex*, Sci. Rep., 3 (2013), p. 3508.

165